Development of a Real-time Spinal Motion Inertial Measurement System for Vestibular Disorder Application

by

Christina Isabelle Goodvin
B.Eng., University of Victoria, 2003

A Thesis Submitted in Partial Fulfillment of the
Requirements for the Degree of

MASTER OF APPLIED SCIENCE

in the Department of Mechanical Engineering

Development of a real-time spinal motion inertial measurement system for vestibular disorder application

By

Christina I. Goodvin
B.Eng., University of Victoria, 2003

Supervisory Committee

Dr. Edward Park, Supervisor

(Department of Mechanical Engineering)

Dr. Brad Buckham, Departmental Member

(Department of Mechanical Engineering)

Dr. Nikolai Dechev, Departmental Member

(Department of Mechanical Engineering)

Dr. Naznin Virji-Babul, Outside Member

(Down Syndrome Research Foundation)

Supervisory Committee

Dr. Edward Park, Supervisor

(Department of Mechanical Engineering)

Dr. Brad Buckham, Departmental Member

(Department of Mechanical Engineering)

Dr. Nikolai Dechev, Departmental Member

(Department of Mechanical Engineering)

Dr. Naznin Virji-Babul, Outside Member

(Down Syndrome Research Foundation)

Abstract

The work presented in this thesis has two distinct parts: *(i)* development of a spinal motion measurement technique and *(ii)* incorporation of the spinal motion measurement with galvanic vestibular stimulation (GVS) technology, acting as a balance assist device hereafter referred to as a galvanic vestibular stimulation device (GVSD). The developed spinal motion measurement technique fulfills seven desired attributes: accuracy, portability, real-time data capture of dynamic data, non-invasive, small device footprint, clinically useful and of non-prohibitive cost. Applications of the proposed system range from diagnosis of spine injury to postural and balance monitoring, on-field as well as in the lab setting. The system is comprised of three inertial measurement sensors, respectively attached and calibrated to the head, torso and hips, based on the subject's anatomical planes. Sensor output is transformed into meaningful clinical parameters of rotation, flexion-extension and lateral bending of each body segment with respect to a global reference space, then collected and visualized via an interactive graphical user interface (GUI). The accuracy of the proposed sensing system has been successfully verified with subject trials using a VICON optical motion measurement system. Next, the proposed motion measurement system and technique has been used to record a standing

subject's motion response to GVS. The data obtained allows the development of a new GVSD with the attributes of: eligibility for commercial licensing, portability, and capable of safely providing controlled stimulating current to the mastoid bones at varying levels and frequencies. The successful combination of the spinal motion measurement technique and GVSD represents the preliminary stage of a balance prosthesis.

Table of Contents

List of Tables

List of Figures

Nomenclature

atan2	arctangent MATLAB function
A	Acceleration [m/s^2]
F_{SEG}	Flexion of segment (head, torso or hips)
Hz	Hertz
$\hat{\boldsymbol{i}}$	x-axis unit vector designation
$\hat{\boldsymbol{j}}$	y-axis unit vector designation
$\hat{\boldsymbol{k}}$	z-axis unit vector designation
l_{SEG}	length of segment (head, torso or hips)
L_{SEG}	Lateral bending of segment (head, torso or hips)
mA	milliamps
${}^{H}_{T}\boldsymbol{r}$	relative position vector from torso to head
${}^{T}_{Hp}\boldsymbol{r}$	relative position vector from hips to torso
${}^{H}_{Hp}\boldsymbol{r}$	relative position vector from hips to head
V	Voltage
$\boldsymbol{V}$	Vector
X, x	x-axis
$X_{G\text{-}SEG}$	fixed global x-axis of the segment
x_{VICONs}	VICON marker x-axis
$x_{VICON\text{-}axis}$	VICON marker x-axis in illustration
$x_{G\text{-}VICON}$	VICON global fixed x-axis
Y, y	y-axis
$Y_{G\text{-}SEG}$	fixed global y-axis of the segment
y_{VICONs}	VICON marker y-axis
$y_{VICON\text{-}axis}$	VICON marker y-axis in illustration
$y_{G\text{-}VICON}$	VICON global fixed y-axis
Z, z	z-axis
Z'_{SEG}	z-axis of the sensor on the segment
$Z_{G\text{-}SEG}$	fixed global z-axis of the segment
$\hat{z}_{SEG}$	z-axis fixed global unit vector of segment
$\hat{z}'_{SEG}$	z-axis final orientation unit vector of segment
$\hat{z}'_{SEG\ X}$	x-axis component of $\hat{z}'_{SEG}$ vector
$\hat{z}'_{SEG\ Y}$	y-axis component of $\hat{z}'_{SEG}$ vector
$\hat{z}'_{SEG\ Z}$	z-axis component of $\hat{z}'_{SEG}$ vector

z_{VICONs} VICON marker *z*-axis

$z_{VICON\text{-axis}}$ VICON marker *z*-axis in illustration

$z_{G\text{-}VICON}$ VICON global fixed *z*-axis

Rotation matrices

$\boldsymbol{r}_{SEG}$ rotation matrix [1x10] output of sensor for segment

$\boldsymbol{R}_{SEG}$ rotation matrix [3x3] output of sensor for segment

${}^{H}_{G}\boldsymbol{R}$ rotation matrix describing head orientation in global coordinate frame

${}^{T}_{G}\boldsymbol{R}$ rotation matrix describing torso orientation in global coordinate frame

${}^{Hp}_{G}\boldsymbol{R}$ rotation matrix describing hips orientation in global coordinate frame

${}^{H}_{T}\boldsymbol{R}$ relative rotation matrix orientation from torso to head

${}^{T}_{Hp}\boldsymbol{R}$ relative rotation matrix orientation from hips to torso

${}^{H}_{Hp}\boldsymbol{R}$ relative rotation matrix orientation from hips to head

Parameters specific to the head segment

l_{HEAD} length of head segment

$\boldsymbol{R}_{HEAD}$ head rotation matrix

X_H *x*-axis of the head segment

X'_H *x*-axis of the sensor on the head segment

$X_{G\text{-}H}$ fixed global *x*-axis of the head segment

Y_H *y*-axis of the head segment

Y'_H *y*-axis of the sensor on the head segment

$Y_{G\text{-}H}$ fixed global *y*-axis of the head segment

Z_H *z*-axis of the head segment

Z'_H *z*-axis of the sensor on the head segment

$Z_{G\text{-}H}$ fixed global *z*-axis of the head segment

$\hat{z}'_{HEAD\text{-}SCALED}$ scaled final position *z*-axis unit vector of head segment

Parameters specific to the torso segment

l_{TOR} length of torso segment

$\boldsymbol{R}_{TOR}$ torso rotation matrix

$X_{G\text{-}T}$ fixed global *x*-axis of the torso segment

$Y_{G\text{-}T}$ fixed global *y*-axis of the torso segment

$Z_{G\text{-}T}$ fixed global *z*-axis of the torso segment

$\hat{z}'_{TOR\text{-}SCALED}$ scaled final position *z*-axis unit vector of torso segment

Parameters specific to the hips segment

l_{HIPS} length of hips segment

$\boldsymbol{R}_{HIPS}$	hips rotation matrix
$X_{G\text{-}Hp}$	fixed global *x*-axis of the hips segment
$Y_{G\text{-}Hp}$	fixed global *y*-axis of the hips segment
$Z_{G\text{-}Hp}$	fixed global *z*-axis of the hips segment
$\hat{z}'_{HIPS\text{-}SCALED}$	scaled final position *z*-axis unit vector of hips segment

Greek Symbols

$\boldsymbol{\sigma}$	standard deviation
$\boldsymbol{\beta}$	pitch
$\boldsymbol{\alpha}$	yaw
ψ	*Cauchy-Schwartz* angle
θ_{SEG}	tilt azimuth angle of segment
φ_{SEG}	tilt angle of segment
τ_{SEG}	rotation or twist angle of segment

Acronyms

AC	Alternating Current
AL	Anode Left
AR	Anode Right
AVR	Animated Vector Representation
CFP	Compound Flexible Pole
COP	Center Of Pressure
DC	Direct Current
DOF	Degrees Of Freedom
ENG	Electronystagmography
G	Global
GUI	Graphical user interface
GVS	Galvanic Vestibular Stimulation
GVSD	Galvanic Vestibular Stimulation Device
HNL	Human Neurophysiology Laboratory
IMU	Inertial Measurement Unit
LACOBS	Laboratory of Applied Control and Biorobotic Systems
MARG	Magnetic Angular Rate Gravity
MEMS	micro-electro-mechanical-systems
MRI	Magnetic Resonance Imaging
MT9	Xsens 6-DOF inertial sensor
PDA	personal digital assistant
P1,P2,P3	VICON reflective marker designations
SDK	Software Development Kit
VICON	Optical motion analysis system
VIHA	Vancouver Island Heath Authority
VNG	Videonystagmography
VOR	Vestibule-ocular reflex

Acknowledgements

Thanks to my supervisor, Dr. Ed Park. Thanks also to the LACOBS team for their programming assistance and GUI. Thanks to Ian Soutar and Ed Haslam for their exemplary work with the GVSD. Thanks also to my friends and family who have provided ongoing support. This thesis is dedicated in part to all those without whom it would not have been a practical reality.

Chapter 1

Introduction

This thesis presents the research and development of (*i*) a three-dimensional spinal motion inertial measurement technique to capture natural full spinal motion, particularly as it relates to posture, and (*ii*) incorporation of the spinal motion measurement system with galvanic vestibular stimulation (GVS) technology as a balance assist device. This chapter presents the motivation behind this work, followed by a summary of thesis objectives and contributions.

1.1 Motivation: Balance and Vestibular Disorders

Balance is the ability to maintain an upright (or stable) position and make purposeful movements within our environment. The overall balance system is a complex system that is comprised of three main systems: vestibular, vision and proprioception. Each system provides a different reference for postural control providing redundancy in the information provided. Failure of one system does not necessarily mean balance is disrupted, an example being that of a blind subject still capable of walking etc. A person may not show mild vestibular dysfunction until they close their eyes. The complex coordination of these systems is managed by the brain. For example, if a person turns the head left, the eyes send visual information about the head turn while the two vestibular systems simultaneously send information about the inertial acceleration of the head turn. At the same time, the proprioceptive system, through the muscles and skin sensors of the neck, also sends information to the brain about the head position. It is the coordination

between these three systems that allows the brain to recognize and interpret the head turn, which in turn signals the body to make postural adjustments to maintain balance. Whenever there is a failure in any part of the balance system, the result is a disruption of balance.

In its most severe form, balance disorders physically interfere with a person's everyday functional abilities, and psychologically, due to an increase in risk of falling. A majority of balance disorders involve the vestibular system, hence are often called vestibular disorders. Some common symptoms of a vestibular disorder are: dizziness, vertigo, imbalance, jumpy vision, and motion sickness. Some common causes of vestibular disorders are: viral infections, tumors, trauma to the vestibular organs, toxic exposure to medication/treatment and aging.

Anatomically, the vestibular system consists of the vestibule and semicircular canals. The location of these structures within the inner ear is illustrated in Fig. 1.1. Within the vestibule are two membranous sacs called the utricle (utriculus) and saccule (sacculus), which are organs that are sensitive to gravity and the body's translational changes. Together, the utricle and saccule detect linear accelerations. The semicircular canals, named the superior, lateral and posterior semicircular canals or ducts, detect rotational changes (i.e. angular accelerations). The sensing receptors of the semicircular canals are hair cells, small protruding hairs that are activated by inertial changes in the enclosed fluid (endolymph). These activation signals are relayed by the vestibular nerves to the brain, which in turn signals the body to make postural adjustments to maintain balance.

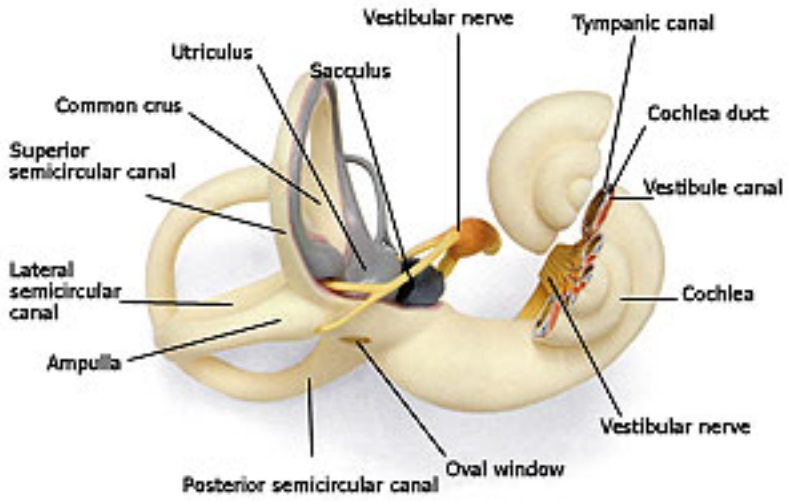

Figure 1.1 Inner ear.

According to studies from the National Institute of Health [1], over 90 million Americans will seek medical attention for balance disorders at least once in their lifetime. At least 2 million Americans suffer chronic impairment due to balance disorders, resulting in annual costs exceeding $1 billion US. For the elderly, falling due to balance disorders is a leading cause of injury and death [2]. In many cases, the cause lies directly due to aging of the vestibular organs, where sensory hair cell death occurs and vestibular sensation is irreversibly lost [3].

1.2 The Need for a Vestibular Prosthesis

We may someday possess the knowledge to promote hair cell regeneration and self-repair, but this remains a distant goal at the moment [4]. At present, the most promising hope of restoring vestibular functions following hair cell death is a vestibular prosthesis, which can be used to re-supply the lost motion information to the vestibular nerves. A vestibular prosthesis should ultimately be an implantable device – a vestibular equivalent of a cochlear implant. However, while our previous work [5] reviewed the feasibility of a totally implantable vestibular prosthesis, the focus of this thesis work lies solely in the development and proof-of-concept demonstration of component technologies of an externally-mounted vestibular prosthesis.

1.2.1 Vestibular prosthesis

A literature survey shows that there are a number of on-going research projects that suggest potential solutions to vestibular/balance disorders. Many of these projects involve the amplification of the human proprioception system. For example, there are inserts that go into footware that sends out vibration to the sole when balance is threatened, and also vests that utilize vibrotactile pads that respond to body-tilt measurements (e.g. [6]). These devices provide short-term rehabilitation of the vestibular system, but not a long-term replacement of the lost vestibular functions intended by a prosthetic device. As illustrated in Fig. 1.2, a true vestibular prosthetic device is dependant first on an accurate postural balance measurement system, and second on the ability to stimulate the vestibular system using a safe stimulation device.

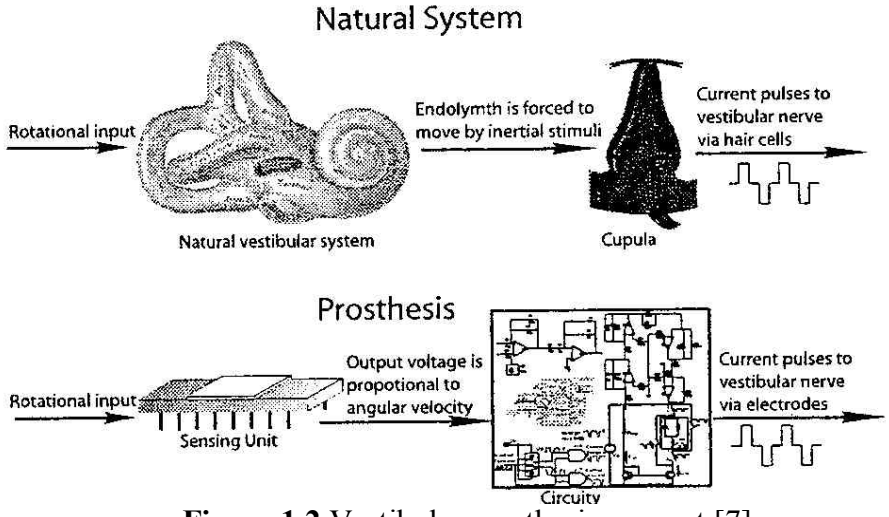

Figure 1.2 Vestibular prosthesis concept [7].

There are currently no commercially available prosthetic devices assisting postural balance control of vestibular disorder patients. Furthermore, even the science and technology behind vestibular testing and treatment is still in a research stage. At this time, no gold standard test has been established to provide a conclusive diagnosis in many vestibular disorder patients [7]. Vestibular specialty clinics have been restricted to major teaching hospitals associated with large university medical schools [8]. This is largely due to the vestibular evaluation equipment being cost prohibitive for small institutions

and clinics. Typical vestibular evaluation equipment includes computerized electronystagmography (ENG) or videonystagmography (VNG), rotary chair testing, and computerized dynamic platform posturography, which could exceed $200,000 US.

The current treatment for vestibular disorders falls into one of four categories: *(i)* medication, *(ii)* surgery, *(iii)* counseling to "learn to live with it", and *(iv)* vestibular rehabilitation. Vestibular rehabilitation through exercise and repositioning techniques has gained popularity only within the last decade, and recent studies demonstrate its efficacy [8]. The ultimate aim of the proposed vestibular device is to offer an alternative treatment strategy to patients with severe vestibular dysfunction, likely those suffering from the lack of hair cells. While the scope of this thesis is limited to the prosthetic application of the device, it is equally valuable as a potential diagnostic tool, which will be addressed in Chap. 5 (as part of discussion on future works).

1.2.2 Galvanic vestibular stimulation (GVS)

GVS is a transcutaneous (through the skin) electrical stimulation technique used to deliver electrical currents to the natural vestibular system. GVS affects the output of the vestibular system to the brain by modulating the continuous firing level of the vestibular afferents. Cathodal (negative) currents increase the firing rate of the vestibular afferents, while anodal (positive) currents decrease the firing rate of vestibular afferents. Depending on the polarity of the current, literature suggests the subject will tend to lean toward the anodal stimulus, and away from the cathodal stimulus.

There are three types of GVS that are of interest in our application. The first and most common is bilateral bipolar (denoted as *bb*) GVS where the anodal electrode is behind one ear, and the cathodal electrode behind the other. The second type is bilateral monopolar (denoted as *b*) GVS: where electrodes of same polarity are at both ears with a distant reference electrode. The third and last type is unilateral monopolar (denoted as *u*) GVS, where the stimulating electrode is at one ear only. The combination of these three types of GVS creates eight possible GVS scenarios (or modes) in total, as illustrated in

Fig. 1.3. Recently, Fizpatrick and Day [9] came up with a model that explains the observed human balance responses for every mode of GVS, in relation to the electrophysiological and anatomy of the vestibular organs (see Fig. 1.4). Note that our natural balance system interprets the GVS as a real head movement in space, one that was unplanned and interpreted as one from movement of the body. This induces a sway response of the body, which can potentially be manipulated as active balance correction measures.

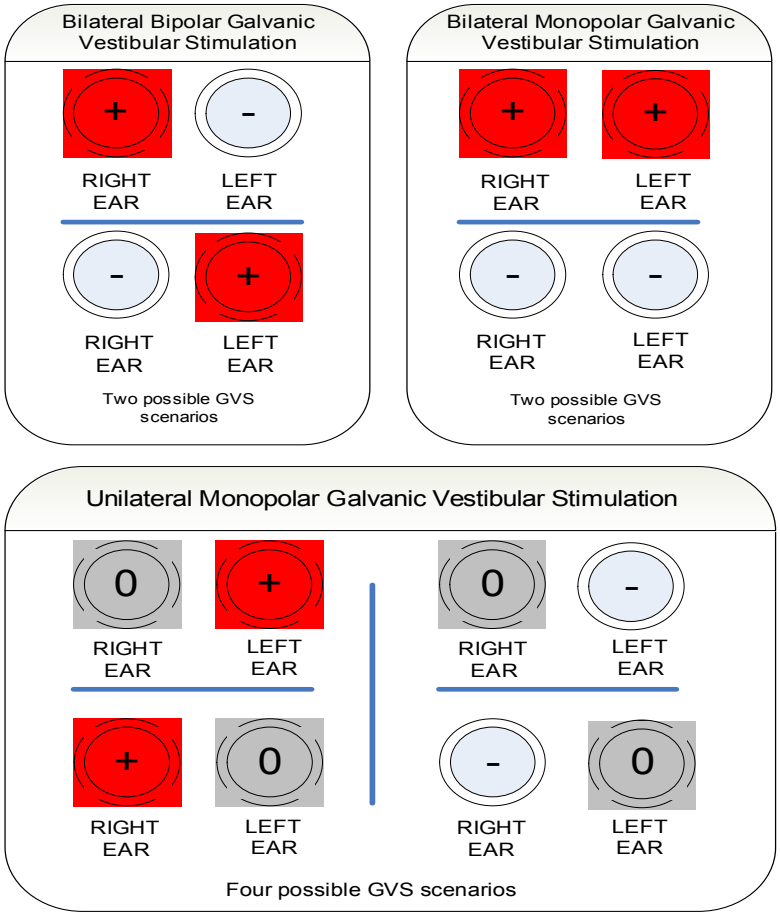

Figure 1.3 Eight possible GVS modes.

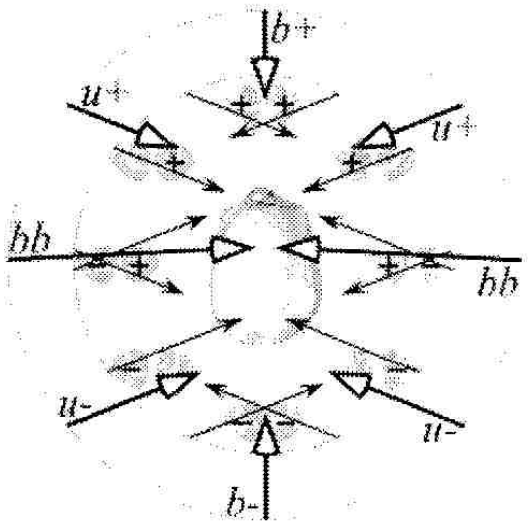

Figure 1.4 Net directional head response to different GVS modes [9].

In the context of a vestibular prosthesis, the main hypothesis of this thesis work is that we can assist vestibular disorder patients by using a postural balance measurement system to monitor their motions, and correct any postural balance instability by triggering one of the eight GVS modes using a GVSD. Currently, there are no commercially available GVSD for postural balance control. Typical stimulators used by vestibular researchers are DC-based analog stimulus isolators, which are designed for a wide variety of transcutaneous nerve and muscle stimulation applications, non-specific to the GVS application. In a GVS setting, such a stimulator delivers high DC voltages (100 volts or more) to the electrodes behind the ears. Hence, there is a need to develop a safer (e.g. lower voltage) and portable (e.g. battery operated) GVSD, suitable as a prosthetic (and research) tool for vestibular disorder patients.

Note that the electrophysiological effect of GVS onto the vestibular nerves is quite different from that of the vestibular stimuli produced by the natural vestibular organs. GVS stimulates the vestibular system as a whole, creating a net effect (e.g. as shown in Fig. 1.4), whereas the natural vestibular stimuli are discrete effects produced by the individual vestibular organs (i.e. the three semicircular canals and two otolith organs, utricle and saccule) in direct relation to the head motions.

Ideally, future implantation of a balance prosthesis allows the vestibular organs to be selectively stimulated, assuming fabrication of surgically implantable, micro-electrode vestibular stimulation circuitry becomes technologically feasible. The motion sensing unit illustrated in Fig. 1.2, which supplies motion information to the micro-electrode circuitry, would be an inertial measurement unit (IMU) mounted or implanted behind the ear. The head, torso and hip sensors detecting 6 DOF (degree-of-freedom) motion would supply combined balance information. Together with the micro-electrode circuitry technology, it would then allow creation of more life-like vestibular stimuli that, when accurately combined with visual and proprioception stimuli by the brain, might result in coherent balance signals. However, with an externally applied stimulation technology such as GVS that sends unnatural vestibular stimuli to the brain, incoherent balance signals will result producing a predictable sway response, which can potentially be used for active balance corrections. If GVS is to be used for correcting balance, a corresponding sensing system is needed to detect the postural balance instabilities of the body in real time. The detection of the head motion alone is not sufficient for active balance corrections using a GVSD. In order to use such a device in active balance corrections, what we require instead is a real-time, portable postural balance measurement system that can detect the balance of the entire body.

1.3 Thesis Objectives and Scope

The primary goal of the work presented in this thesis is to develop an appropriate postural measurement system for the prescribed application. The emphasis is to make such a system ambulatory – able to wear by a vestibular patient outside the laboratory setting – so that it becomes a useful part of a vestibular prosthesis. Ideally, such a sensing system is inertial based like the natural vestibular system. In addition, as this work is a preliminary study, we have simplified the postural balance problem by ignoring the movements of the upper limbs and lower limbs (i.e. no gait motion). This implies that the sensing system only needs to capture the movements of the head, torso and hips, which exactly corresponds to the movements of the spine.

Consequently, the goal of this work can be redefined as the development of a human spinal motion measurement technique. The ideal attributes of this system include measurement accuracy, beyond laboratory portability, real-time measurements of dynamic motion, non-invasive application, minimal device footprint, non-prohibitive cost and a high clinical usefulness. No technique reported in literature to date is able to satisfy these criteria. Hence, the first objective is to develop a spinal motion measurement system that fulfills the listed criteria.

The second objective is to incorporate the sensing technique with a novel galvanic vestibular stimulation device (GVSD). The GVSD has been custom-developed by our research group, the Laboratory of Applied Control and Biorobotic Systems (LACOBS), at the University of Victoria (UVic), to act as a balance prosthetic device or research tool. To date there are no commercially available GVS devices approved for clinical use.

1.4 Thesis Contributions

The thesis work has led to the development of a novel spinal motion measurement technique using three IMUs. The author has combined the sensors together with unique algorithms to model the spine and output the data in clinically significant parameters. Attached to the head, torso and hips, respectively, the sensing system provides the real-time measurements of the upper body postural motion in the clinically useful parameters of flexion/extension, lateral bending and rotation. While the proposed system was developed for postural monitoring, it has shown more immediate application in the economical standardized diagnosis of spine injuries, replacing non-standardized conventional clinical techniques. With additional sensors (up to ten in the current system configuration), additional spinal motion measurements can be made. Furthermore, by attaching additional sensors to upper and lower limbs as well, continuous monitoring of entire body becomes possible in a portable and unobtrusive manner. The potential impact of such a “wearable” human movement analysis is enormous [10], opening the possibilities of continuous monitoring of patients on-field, including vestibular disorder patients. The research has also been used to direct development of an AC-based GVSD.

1.5 Overview of Thesis

Chapter 2 provides detailed background information on the current state of the spine measurement, inertial sensing, and GVS technologies, defining the basic framework (e.g. design criteria and research questions) in which our research is carried out. Chapter 3 picks up from Chapter 2, explaining our proposed solution. Chapter 4 describes the experimental set-up for verification and testing. Chapter 5 presents the experimental results, including an evaluation according to the design criteria we have chosen. Chapter 6 concludes by summarizing the achievements and their impact on the research questions we raised in Chapter 2. The Appendices provide additional technical materials that support the results presented in Chapter 5.

Chapter 2

Scientific Background

As pointed out in Sec. 1.3, the research carried out in this thesis has two distinct parts: *(i)* development of a spinal motion measurement technique and *(ii)* incorporation of the spinal motion measurement system with GVS technology, to create a balance assist device, referred to as a GVSD. The purpose of this chapter is to define the framework of the thesis with respect to the above two parts, and to provide pertinent background information.

2.1 Spine Motion Measurement Techniques

With 24 flexible vertebrae influenced by an intricate supporting physiological framework of muscles, tendons, and ligaments, capturing motion of the human spine is a complex endeavor. The accurate three-dimensional (3D) motion capture of the human spine is a complex process, particularly when real-time data is required. Existing techniques used in practice to measure spine motion include: optical tracking [11], radiology [12], electromagnetic techniques [13], and goniometers and inclinometers. In medical clinics, goniometers and inclinometers are the most prevalently used techniques to assess and diagnose the spine. Goniometers measure the angle between two device arms, aligned with body segments and bony landmarks, capable of motion in one plane. Inclinometers measure tilt with respect to gravity. Goniometers (and inclinometers) are useful in generalized static situations, measuring the angle between an initial and final position of a

single joint or the spine, but are restrictive due to positioning errors and often act as a mechanical constraint. Radiology, involving hazardous x-ray photography of the bones, is a 'snapshot' technique of tracking the initial and final images in a motion. This is also a static technique, and the dynamic information of spinal motion cannot be measured. In research, optical tracking is prevalently used to capture dynamic spine motion. While it is a highly sophisticated technique, the cost and volume of equipment used in optical tracking restricts it to the laboratory environment. The technique is also beset with occlusion problems, where the cameras cannot accurately define a marker throughout the motion, resulting in lost position data. Electromagnetic tracking devices are very useful for relative joint measurements but are limited by the speed of joint motion that can be measured and are highly susceptible to electromagnetic interference.

Literature review suggests that clinicians need a portable and continuous way of recording 'everyday' real-time spinal motion of their patients, particularly outside the restricting volume of the laboratory environment. Such a method has the potential to redirect clinical assessment from the specialized lab setting to the more relevant real-life setting (such as the home), where the patient's normal daily activities are actually carried out [10]. While such a method would provide clinicians and therapists with more natural data complementary to the controlled lab data, it would also allow the monitoring of a patient's postural balance, which is an objective of this work. The ideal spinal motion capture system should have the following seven major attributes:

i. accuracy,
ii. portability,
iii. real-time measurement of dynamic data,
iv. non-invasive application,
v. minimal device footprint,
vi. high clinical usefulness, and
vii. non-prohibitive cost

which are graphically summarized in Fig. 2.1.

Currently, the most promising sensing technology that can satisfy all these attributes seems to be inertial sensors. The use of inertial sensing systems is becoming more and more widespread as their components are becoming smaller and more reliable to use. The current state of the inertial sensing technology is summarized below, in Sec. 2.1.2. To provide additional information on how typical assessment and diagnosis of the spine are performed, the existing clinical spinal measurement techniques are explained in more detail in Sec. 2.1.1.

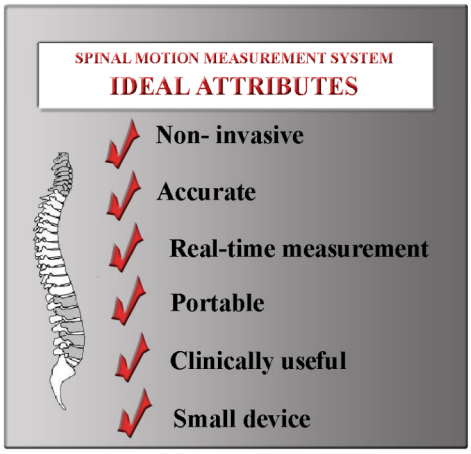

Figure 2.1 Spinal motion measurement system ideal attributes.

2.1.1 Clinical spinal motion measurement techniques

The equipment used in clinical evaluation varies in degree of sophistication, often based on the information desired by the clinician. In addition, clinical techniques are often restricted by the cost and functionality of the equipment. The level of sophistication of the information provided by measurements can range from a simple number to quantify a parameter like flexion or extension, up to detailed kinematic descriptions of how the spine moves segmentally from full extension to full flexion [14]. Preliminary examination of a patient will also determine the choice of measurement technique and information required to provide full diagnosis.

Since each patient has a unique range of motion, clinical specialists often use relative comparisons of the subject's range of motion to assess healing, damage, and/or disability. Spine mobility is quantified primarily using surface level techniques, which involve measurement of a patient performing a set of motions while measured with goniometers, inclinometers, tape measure, or skin markers placed on surface landmarks. As already mentioned above, two of the most representative measurement techniques used in clinical evaluation involve goniometers and inclinometers.

2.1.1.1 Clinical 'surface level' tests used to assess range of motion

There are four common representative clinical tests used to assess a patient's range of motion [15, 16]. The instrumentation in all four is based on expert application by the clinician of goniometers, inclinometers, and measuring tape. The first test (Test 1) is a standing flexion test, measured with either the inclinometer or goniometer method, beginning with the patient standing in a neutral spine position (standing upright, relaxed). The inclinometer method for Test 1 places one of two inclinometers over the T12 spinal vertebrae (shoulder level) and the other at the level of the sacrum (hip level), both in the mid-sagittal plane (see Fig.2.2). Both inclinometers are zeroed with the subject standing in the neutral position. The patient is then instructed to flex his trunk forward (bend forward) as the inclinometers are held in position by the clinician. The goniometer method requires the subject to go through the same motion while the clinician holds the goniometer to the lateral aspect (side) of the patient, placing the second arm of the goniometer by eye once the subject has flexed.

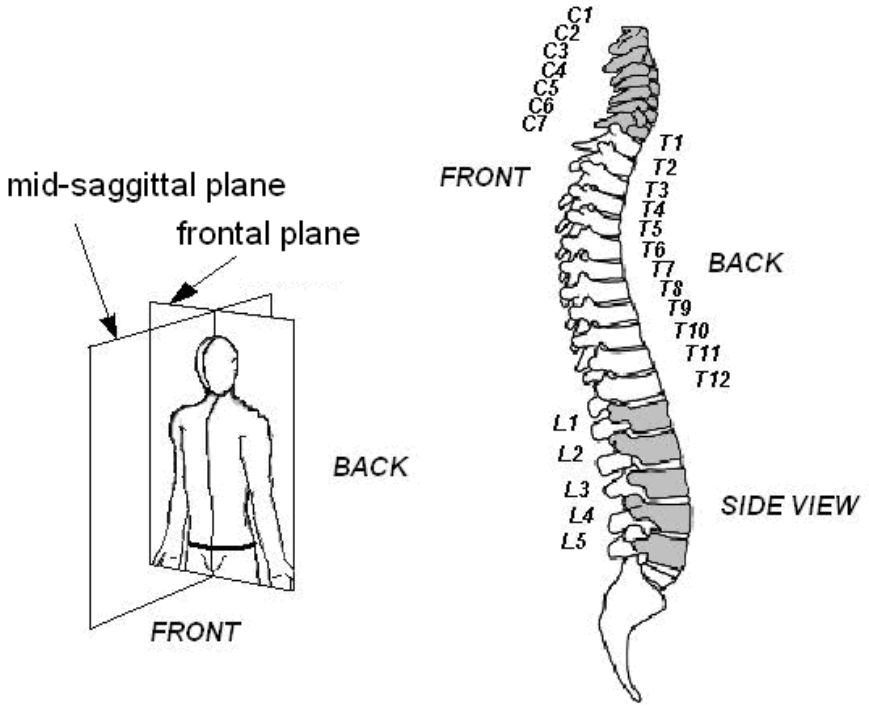

Figure 2.2 Spinal vertebrae and anatomic planes.

The second test (Test 2) is the standing extension test, similar to Test 1 with the motion of the patient in the reverse direction (bending backwards). This test can also be measured with either the inclinometer or the goniometer. The third test (Test 3) is the standing lateral flexion tests for both sides. For the goniometer method the devices are placed as in Test 1, but within the coronal (frontal) plane. The fourth test (Test 4) is a sitting rotation goniometer test with the subject sitting on a chair with arms crossed over trunk. The subject alternately rotates right and left, with the resulting angle from neutral measured and recorded for each side.

All four tests are typical of clinical motion evaluation of the spine to determine range of motion of a subject. The inclinometers and goniometers are cost effective portable instruments used by clinical specialists who place and read the devices 'by eye'. They are non-invasive, and minimally hinder the motion of the subject. However, they lack accuracy, have limited application to specific single or multi-axis joints [17], and are incapable of capturing the dynamic motion of the spine. As well, goniometers and

inclinometers lack the ability to provide detailed measurements on segmental spinal analysis. These surface techniques, and other non-invasive methods [14, 15], provide limited, but still valuable quantitative information on the mobility of the patient.

2.1.1.2 Clinical 'in-vivo' tests used to assess range of motion

Ultrasound and Magnetic Resonance Imaging (MRI) are not sufficiently well developed to allow motion analysis of an erect patient, and as a consequence X-ray techniques currently offer the most practical route to segmental level analysis [18, 19]. Radiology provides an opportunity for clinicians to gain static segmental visualization of the spine using 'snapshot' pictures of bony landmarks at various stages of a motion. The snapshots can be superimposed to allow geometric analysis. The higher the radiation dose used the better quality the images that result. Subjects are typically restrained in such a way as to control the two-dimensional (2D) motion that will be captured. For example, for lumbar spine flexion-extension analysis the subject will have their hips immobilized in a holding structure such that the resulting motion is constrained to lumbar motion only. Though widely used by hospitals and clinics, segmental analysis by radiology is a tool that is used conservatively due to invasive radiation exposure of the patient. The technique is employed for acute spinal injuries and diseases of the spine [20]. Differences in set-up of the patient in the restraint apparatus between treatments can also affect accuracy. The technique lacks portability, real-time dynamic data measurement, is invasive, costly, and has a large equipment footprint.

2.1.2 Inertial sensing in human motion measurement

Accelerometry has a long history in the field of human motion analysis [21]. For low relative accelerations a 2D or 3D accelerometer unit can be used as an inclinometer, indicating altitude or tilt of an object with respect to gravity. Gyroscopes [22] can be used to provide angular velocity measurements, and when combined with accelerometers, can provide a more descriptive measurement of motion [23]. Rapid continued development of micro-components, particularly using micro-electromechanical systems (MEMS)

technology, has resulted in commercially available miniature inertial motion sensors suitable for human orientation and position measurements. Traditionally, inertial sensors have found applications in aviation and robotics [24], using a combination of accelerometers and gyroscopes to monitor dimensional parameters such as roll, pitch, yaw, linear accelerations, rotational velocities, and assorted derived parameters such as altitude and heading.

More recently, inertial sensors composed of MEMS accelerometers and gyroscopes have been proposed to analyze ambulatory human movement, including the monitoring of daily living activities [25, 26]. Inertial sensors have been successfully evaluated and used to track human segment motion with reasonable accuracy [22-23, 27-29]. The knee joint has also been of particular interest in applications of inertial sensors [30]. Measurements of the lumbar spine using inertial sensors have been successfully evaluated [31]. However, accuracy of orientation measurements has often been a problem with inertial sensors using gyroscopes, which are actually rate gyros, as any error in the gyro's measurement will result in larger inaccuracies after integration of angular velocity to obtain orientation angles. This integration drift error has restricted the use of inertial systems, rendering the measurements inaccurate in less than a minute [22]. To maintain accuracy over time a number of solutions have been developed and the most relevant solution to our research is the integration of magnetometers into the inertial measurement system to provide an absolute reference of magnetic north to reduce drift.

Gravitational acceleration is dominant for most human motions, and as mentioned previously, accelerometers can be used as a tilt (gravitational) sensor in low relative accelerations. This ability allows for inclination drift compensation of gyro measurements about the two horizontal axes (pitch and roll axes), but leaves the vertical axis (yaw axes) drift error uncorrected since accelerometers cannot measure rotation about the vertical axis (no gravitational change). Sensing systems fusing accelerometers and gyros have been enhanced through the development of a Kalman filter, resulting in drift-free attitude orientations [22]. To correct yaw/heading drift magnetometers can be used. This additional yaw rate compensation, combined with a sophisticated proprietary

Kalman filtering technique to compensate for the effects of magnetic disturbances, has been developed and implemented by Rotenburg et al. [32], and is present in the technology of the sensors (from XSens) employed in this thesis work.

The feasibility of using a 3D real-time inertial measurement system for full spinal motion has not been explored by other researchers. The proposed inertial spinal motion measurement system promises accuracy, portability, affordability, real-time measurement of dynamic data, non-invasive application, minimal device footprint, and a high clinical usefulness.

2.2 Vestibular-related Motion Measurement Techniques

The second objective of this thesis is the development of a balance assist device, the GVSD, which incorporates the spinal motion measurements system as bio-feedback for postural stability. The proposed GVSD operates using GVS that, as described in Chap. 1, is a process of transcutaneously exciting the vestibular system using mild electric currents to induce a sway response of varying magnitude. By characterizing the GVS sway response of each subject using a motion measurement system, it becomes theoretically possible to correct the sway resulting from postural instability. When such a sway is detected by the motion measurement system, a corrective sway can be induced using GVS in order to correct the patient's balance. The ideal GVSD has three major attributes:

i. capable of safely providing controlled stimulation current to the mastoid bones at varying current levels and frequencies,
ii. portability,
iii. eligibility for commercial licensing (evaluated as safe for human experimentation).

Sec. 2.2.1 below provides background information on how typical assessment and diagnosis of the vestibular/balance disorders are performed followed by a description of the basic framework for the GVSD in Sec. 2.2.2.

2.2.1 Clinical assessment of postural balance function and motor control

An excellent summary of clinical tests and their reliability has been done in [33, 34], and is used as the basis for the following description of clinical postural measurement techniques. The description is to give the reader a basic and general idea of some of the methods used in the clinical setting. Clinical tests are based on functional performance of the subject while asked to perform various tasks. Tests such as the Romberg, Sharpened Romberg, Timed One-Leg Stance, and Clinical Test of Sensory Integration and Balance, require the subject to stand with their feet in specific positions, with performance evaluated by examining clinician. The Sternal shove, and Postural Stress Test, evaluate the subject's response to controlled perturbations from the clinician or from weights secured to the waist. There are also several performance based tests including the Functional Reach Test, Get-up-and-go Test, and Berg Balance Scale that evaluate the subject's ability to perform basic tasks involving gait and balance. It is important is to note that all of these basic tests are based on the clinical examiner's skill at evaluating the motion of the subject, and allow the examiner a method by which to direct further diagnosis of balance dysfunction, if required. The tests are non-standardized, due to individual interpretation of results, though are easily performed in any clinical setting and measure natural response of the subject.

2.2.1.1 Vestibule-ocular reflex and nystagmus

The vestibular system responds to motions of the head by acting to stabilize visual focus on the environment through the vestibule-ocular reflex (VOR). The visual and vestibular information is integrated with the proprioceptive data received by the brain. One method of clinically evaluating balance dysfunction is through electronystagmography (ENG), a common clinical method that measures involuntary eye motion (nystagmus). During ENG electrodes placed on the skin around the eye record eye motion relative to a ground electrode attached to the forehead. Another method gaining popularity is videonystagmography (VNG), which measures eye motion by camera tracking the pupil of the eye. This technique can be used in the dark, which removes any possible visual

fixation points that would affect readings. A test usually included with ENG and VNG testing is the caloric test, which records nystagmus resulting from circulation hot and cold water or air alternately in the ear canal, stimulating the lateral semicircular canal by causing a thermal movement of fluid inside of the canal. The comparison indicates the relative strength or weakness of one ear relative to the other, determining whether there is a defect in either ear. However, abnormal readings from VNG and ENG do not imply vestibular dysfunction explicitly, and caloric testing only provides data on one of the three semicircular canals in each ear [20].

2.2.1.2 Force plates

The force plate, a computerized stability assessment method, is the most widely reported method of quantitative balance measurement in literature [33]. The force plate, a flat platform balanced on three or more force measurement devices, records the displacement of the center of pressure (COP) of the standing subject. Most force plates evaluate four aspects of balance: *(i)* postural sway or steadiness of the subject as they try to remain motionless, *(ii)* symmetry of the weight distribution between the feet of the subject, *(iii)* dynamic stability of the ability to move COP to remain in a stationary position, and *(iv)* the subject's automatic motor responses to disturbances of the platform surface. Force plates are commonly combined with visual stimulus, such as virtual reality goggles or projections screens, to evaluate vestibular disorder via the VOR.

The costs of these systems are very high, as well as non-portable, restricted to a small performance volume and limit the technology to specific clinics and institutions. The natural motion of the subject may or may not be hindered by retraining devices used to stop the subject from serious falls.

2.2.2 Research assessment of balance function and motor control

As computational methods and sensing systems become more sophisticated, the various methods employed to measure the body's response to the environment are integrated to provide greater levels of information. Those of particular interest involve a combination

of force platforms, GVS, and inertial measurement systems. The combination of force plate and GVS has been studied by many researchers, e.g. [35], to better understand the effects of GVS on vestibular system. The resulting postural sway of the subject undergoing GVS is determined from measurements of their COP as they stand on the force platform. However, the GVS system is not suitable for non-research applications due to potentially unsafe driving voltages (100~200 V). The possibility of using accelerometers (a triaxial accelerometer, 3 DOF) to monitor standing balance has been proposed in [36]. To date there has been no known work combining 6 DOF inertial measurement systems and GVS.

2.3 GVSD Development

With a suitable motion capture system to provide real-time accurate biofeedback on postural balance, the second stage of the research is to develop a GVSD. In this work, the GVSD will act to correct postural sway based on the biofeedback response of the subject's position and orientation of the spine. A GVSD is needed to drive the desired current to stimulate the vestibular system via electrodes placed behind the ears on the mastoid process. The effects of GVS have been studied extensively, linked to beginnings with Alessandro Volta himself [37-39]. To date there is no commercially viable GVSD available for use outside the research lab environment. One device available for research is a PC-based GVS system developed at the University of British Columbia (UBC), which is capable of transcutaneously delivering electrical currents to the vestibular system to invoke GVS response [35]. Using the established standard stimulation parameters, subject response can be characterized and used to guide development of our own GVSD system suitable for clinical use.

2.3.1 GVSD design parameters

As shown in Fig. 1.4, an expert model has recently been presented in literature that explains the observed postural sway responses resulting from the effects of GVS on human balance control, including electrophysiology and anatomy of the vestibular

organs, and it is this model that we reference in our own research [37]. Mathematical equations of the semi-circular canals have also been developed to predict the optimal head position of the subject for rotational stimulation [37, 39]. From this research we know that small-amplitude galvanic current stimulation, ranging between 0 and ±5 mA, is well known to evoke predictable sway response in the standing or sitting subject [6, 9, 35, 37-39]. The effect of GVS on a walking subject has also been studied [40].

In order to achieve a desired stimulation current at the mastoid process we must take into account the skin resistance as well as electrode properties. A high skin resistance and/or poor electrode construction, and/or contact will reduce the effective current and require a higher driving voltage. The higher the driving voltage, the more unsafe the device becomes for human research. Research based GVSDs are direct current (DC) which characteristically require higher driving voltages to overcome the skin resistance effects that develop with DC stimulators. These high driving voltages render the device unsafe for clinical and commercial use. To develop a GVSD that is commercially and clinically viable, the driving voltage must remain low (e.g. under 24 V) while still providing adequate controllable stimulation current (up to 5 mA). In addition, to use the GVSD with the spinal motion measurement device, the GVSD itself must also be portable.

The combination of an inertial motion measurement system fulfilling the seven ideal attributes (accuracy, portability, affordability, real-time measurement of dynamic data, minimal device footprint, and high clinical usefulness), combined with a portable GVSD system safe for human clinical use, has yet to be proposed outside of this thesis.

Chapter 3

Development of Proposed Spinal Measurement System

Picking up from the previous chapter which defined the basic framework of the thesis work, this chapter defines and outlines the steps taken towards the development of a spinal motion measurement system. Results from these developments are presented in Chap. 5.

3.1 Inertial Sensor Selection

As defined in the previous chapter, the ideal spinal motion measurement system should have the following attributes (Fig. 2.1): accuracy, portability, affordability, real-time measurement of dynamic data, non-invasive application, minimal device footprint, and a high clinical usefulness. With a spinal motion measurement device capable of fulfilling the ideal attributes, we can also integrate the device with a commercially viable galvanic vestibular stimulation device (GVSD) to provide biofeedback on postural balance and stability.

The first step in fulfilling the stated ideal attributes of a motion measurement system is selecting the sensors to use. For the design objective of having a PC based device we selected three small state-of-the-art inertial measurement units (IMUs), commercially available MT9 sensors from Xsens Technologies B.V., in the Netherlands. The number of sensors selected corresponds to the three body segments they will be attached to; the

head, torso and hips. Each IMU is a "9-degree-of-freedom (DOF)" solid-state motion sensor, or, a miniature gyro-enhanced MARG (Magnetic, Angular Rate, Gravity) system that provides drift-free three dimensional orientations as well as calibrated 3 DOF linear accelerations (from micro accelerometers). They also incorporate 3 DOF angular velocity (from micro gyroscopes) and 3 DOF magnetic field data (from micro magnetometers). The sensors compensate for the drift errors resulting from temperature effects on the integration of the angular velocity data by using accelerometer and magnetometer measurements, and have singularity free orientation output.

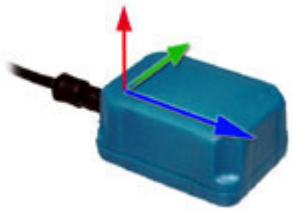

Figure 3.1 Xsens MT9 inertial measurement unit (IMU).

The sensors come equipped with a proprietary filtering and 'data-fusion' capabilities via a digital data bus, Xsen's XBus device, allowing simultaneous real-time measurements from each of the three sensors. The XBus system also has a Bluetooth-based wireless connection capability for combination with a personal server such as a PDA, allowing an increased level of portability ideal for on-field measurements. The XBus is capable of simultaneous measurement of up to 10 sensors. Output from the sensors can be directly transferred to the PC, via serial cable, using either the accompanying SDK (software development kit), or can be called using Xsens proprietary functions to directly interact with any PC loaded with software application development programs such as Matlab. The SDK software is useful for accuracy tests, such as magnetic compensation tests, and drift-over-time tests, as it directly stores the output files of the sensors as orientation data (quaternion, Euler angles, or rotation matrix) and calibrated and/or raw data format. Each sensor will output the orientation (with respect to calibrated 'world') of the object to which it is attached and calibrated. The sensor output options are illustrated in Fig. 3.2.

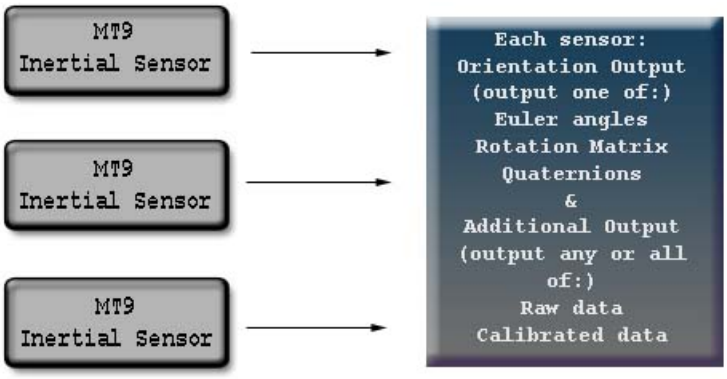

Figure 3.2 Inertial sensor output options.

3.2 Modeling of the Human Spine

Our spinal model has been developed to utilize the above three sensors. Each sensor measures the resultant motion of a group of spinal vertebrae with each group designated as a segment, corresponding with three intuitive segments of the spine. As shown in Fig. 3.3, the human spine is composed of three main sections of vertebrae, the cervical spine (neck), the thoracic spine (chest) and the lumbar spine (lower back). Each of these has a distinct curvature and range of motion. The cervical spine is the most mobile region of the column, made up of seven vertebrae, labeled in descending order as C1 through C7. The first vertebra, C1, is known as the atlas, the second, C2, as the axis. These two vertebrae form a unique structure that allows the wide range of rotational movement of the skull which sits on the atlas. The thoracic spine contains 12 vertebrae (descending T1-T12) and is a highly mobile portion of the spine that articulates with the twelve attached rib pairs. The lumbar spine is the least mobile portion of the main column, a weight bearing structure, and contains 5 vertebrae (descending L1-L5). The sacrum is a large triangular bone at the end of the spinal column which sits between the two hip bones like a wedge.

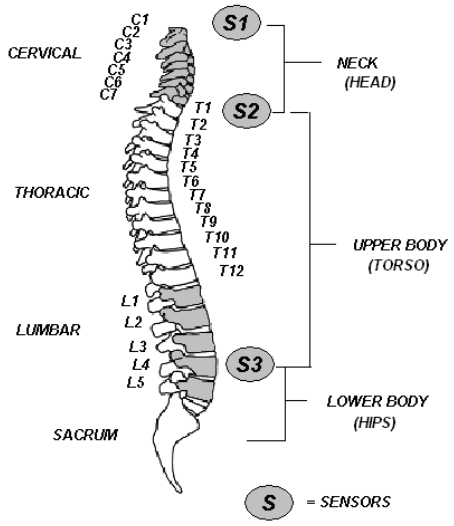

Figure 3.3 Human spine vertebrae and segment divisions.

In our application, three distinct regions are represented our model: the neck region (C1-C7/T1), the upper body region (C7/T1-L4), and the lower back region (L4-L5/Sacrum). Motion of the spine in three segments can be visualized using a compound flexible pole (CFP) model, as shown in Fig. 3.4. This approach allows us to represent the orientation of the spine with three sensors, with the measurements expressed in the intuitive clinically useful parameters of rotation, flexion-extension and lateral bending. Each CFP segment is represented as a flexible pole and a rigid body to which each sensor is attached. The rigid body at the shoulders and hips is considered rigidly attached to the connecting vertebrae of the next flexible pole.

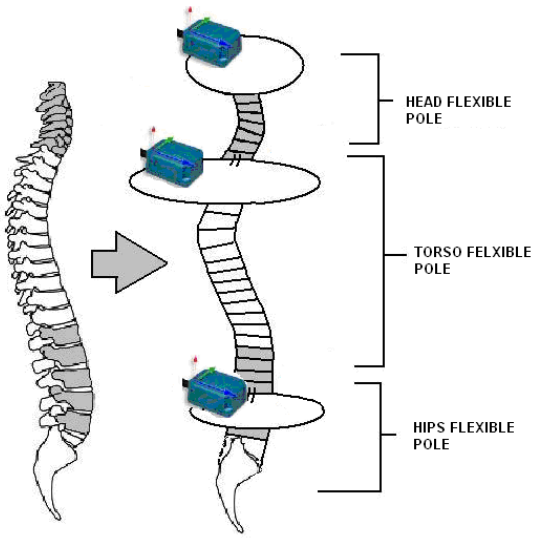

Figure 3.4 Compound flexible pole model with sensor placements on head torso and hips.

The flexible pole visualization is capable of accommodating the flexible bending and twist motions in three dimensions, with negligible deformations along its length. This allows us to visualize measurements at three strategic locations – the head, torso, and hips which are separated by three flexible poles capable of rotation, flexion-extension and lateral bending.

The orientation of the rigid-body component of each CFP can be measured using the rotation matrix output of the sensors. The rotation matrix is a representation of the sensor coordinate axes (local sensor coordinate frame) described in the global (or world) coordinate frame set during calibration. Each sensor has a calibration capability to align the world axes of the sensor to the object on which the sensor is attached, thereafter measuring orientation of the object in the world frame. For our modeling and measurements, the resting position of the body segments (i.e. head, torso, and hips) are set as the balanced position of the standing (or sitting) subject at rest, facing forward, relaxed with arms hanging at sides and with feet shoulder width apart. Effectively, the world axes become the resting position axes, as we have chosen this position to represent the most stable orientation. Each sensor is individually calibrated to the spine segment on which it is attached. Once calibrated, the orientation of the coordinate systems of the

segment and the attached sensor are equivalent, i.e. both with *X*-axis forward, and *Z*-axis opposite the gravity vector, as seen in Fig. 3.5. All sensor measurements are made with respect to the calibrated global (world) coordinate system. The calibrated *Z* direction is the vertical direction (opposite gravity) with the *X* direction representing the forward horizontal direction along the mid-sagittal plane, and the *Y* direction as designated by the right handed coordinate system convention (left).

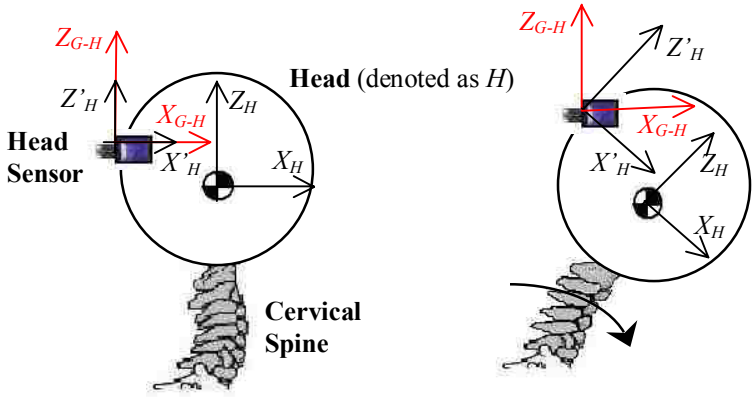

Figure 3.5 Location of the global (*G-H*), sensor (*H'*) and head (*H*) coordinate axes in the case of the head/neck region during *(i)* calibration and *(ii)* motion (refer to nomenclature).

A literature review yielded a published technique known as the tilt/twist method, used to measure the flexion/extension, lateral bending and rotation of the spinal vertebrae. Processing the sensor rotation matrices using the tilt/twist method [28] allows us to express motion parameters in the clinically useful and intuitive format of rotation (twist), flexion/extension and lateral bending. With a rest/world position, rotation can be described as motion about the *Z*-axis (opposite gravity vector) of the segment's rigid body. Flexion is the bending (tilt) forward, leaning forward or looking down motion along the mid-sagittal plane of the segment. Extension is a return to the rest position from a flexion position with hyperextension describing motion such as bending backwards, leaning backwards, or looking up, along the mid-sagittal plane from rest or reference position. Lateral bending can be described as motion along the frontal plane, or tilting of the segment right or left.

3.2.1 Vector representation of the spine

The rotation matrix orientation output describing the segment/sensor orientation in space from each sensor is the following 1×10 vector,

$$\boldsymbol{r}_{SEG} = [t \quad a \quad b \quad c \quad d \quad e \quad f \quad g \quad h \quad i] \tag{1}$$

with the first column representing the time count, and the remaining columns representing the indices of the 3×3 rotation matrix, i.e.

$$\boldsymbol{R}_{SEG} = \begin{bmatrix} a & d & g \\ b & e & h \\ c & f & i \end{bmatrix} \tag{2}$$

where the subscript *SEG* denotes a particular spinal segment (e.g., head, torso, or hips) to which a sensor is attached. The rotation matrix represents the orientation of the sensor in the global coordinate frame (denoted by subscript *G-SEG*), see Appendix A for full theory. Recall the global coordinate frame is set as the resting/relaxed position of the subject. The tilt/twist method translates the change in orientation of the object position vector $\hat{z}_{SEG}$, initially aligned during calibration with the global position vector Z_{G-SEG}, as seen in Fig. 3.6. The initial calibrated axis coordinate unit vectors for each segment can be defined as follows, e.g.

$$\hat{\boldsymbol{x}}_{SEG} = \begin{bmatrix} 1 \\ 0 \\ 0 \end{bmatrix} = \hat{\boldsymbol{i}}_{SEG} \;,\; \hat{\boldsymbol{y}}_{SEG} = \begin{bmatrix} 0 \\ 1 \\ 0 \end{bmatrix} = \hat{\boldsymbol{j}}_{SEG} \,,\; \hat{\boldsymbol{z}}_{SEG} = \begin{bmatrix} 0 \\ 0 \\ 1 \end{bmatrix} = \hat{\boldsymbol{k}}_{SEG} \tag{3}$$

For each sample time, the rotation matrix $\boldsymbol{R}_{SEG}$ is output by the sensor attached to the segment, representing the orientation of the segment with respect to the world axes. Using the matrix we can calculate the new orientation vector of the segment, i.e.

$$\hat{\boldsymbol{z}}'_{SEG} = \boldsymbol{R}_{SEG}\, \hat{\boldsymbol{z}}_{SEG} \tag{4}$$

where $(\bullet)'$ denotes that the quantity represents the sensor coordinate frame (see Fig. 3.6). The new orientation vector in Eq. (4) still maintains a unit length:

$$\left|\hat{z}'_{SEG}\right| = \sqrt{\left(\hat{z}'_{SEG\text{-}X}\right)^2 + \left(\hat{z}'_{SEG\text{-}Y}\right)^2 + \left(\hat{z}'_{SEG\text{-}Y}\right)^2} = 1 \tag{5}$$

The new vector in Eq. (4) is then further scaled to match the measured length dimension of the segment to which it is attached, l_{SEG}, the approximate distance from the sensor on the spine segment to the next sensor location, i.e.

$$z'_{SEG\ \ SCALED} = l_{SEG}\,\hat{z}'_{SEG} \tag{6}$$

As shown in Fig. 3.6, this is the new vector representation of the length of the segment, the orientation of the segment in world space, and the *Z*-axis of the segment's sensor coordinate frame (Z'_{SEG}).

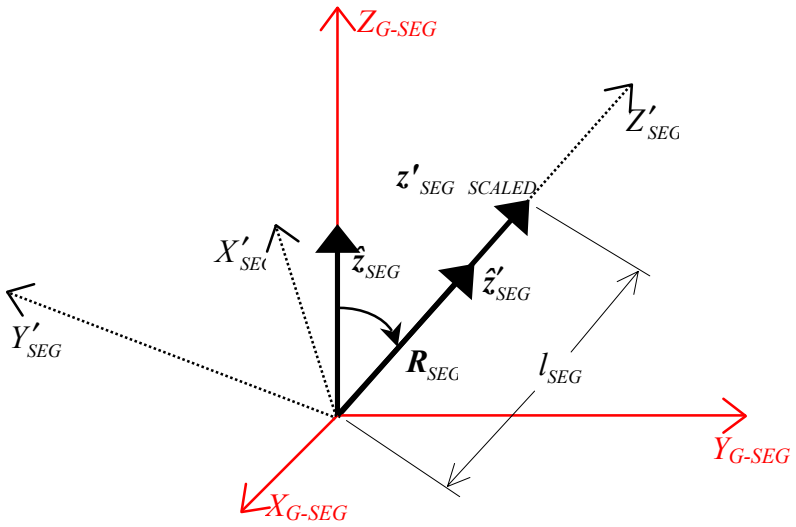

Figure 3.6 Illustration of the segment orientation and scale with respect to a global reference frame *G-SEG*.

With the known measurement of the subject segments, the length dimensions for the hips, l_{HIPS}, the torso, l_{TOR}, and the head, l_{HEAD}, are defined. Note that for the hips, the distance l_{HIPS} can be measured from the hip sensor to the floor. Now, using Eq. (6) with l_{HIPS} and $\boldsymbol{R}_{HIPS}$ available, we can begin the construction of a vector representation of the CFPs representing the spine segments by calculating the new scaled orientation of the hips: $z'_{HIPS\ \ SCALED} = l_{HIPS}\hat{z}'_{HIPS}$.

Subsequently, as illustrated in Fig 3.7, the position of the origin of the global torso coordinate frame (*G-T*) then coincides with the tip of the $\bar{z}'_{HIPS-SCALED}$ vector, which has the length l_{HIPS}. This relationship is based on the interconnected nature of the human spine represented by the CFP visualization. Using the length, l_{TOR}, and the torso rotation matrix, $\boldsymbol{R}_{TOR}$, we now have the following expression for the scaled orientation vector of the torso: $\boldsymbol{z}'_{TOR\ \ SCALED} = l_{TOR}\hat{\boldsymbol{z}}'_{TOR}$. This vector also represents the point of origin of the global head coordinate frame (*G-H*). Again, using the length l_{HEAD} and the head rotation matrix $\boldsymbol{R}_{HEAD}$, which is directly output from the head sensor, we can calculate the scaled orientation vector of the head: $\boldsymbol{z}'_{HEAD\ \ SCALED} = l_{HEAD}\hat{\boldsymbol{z}}'_{HEAD}$.

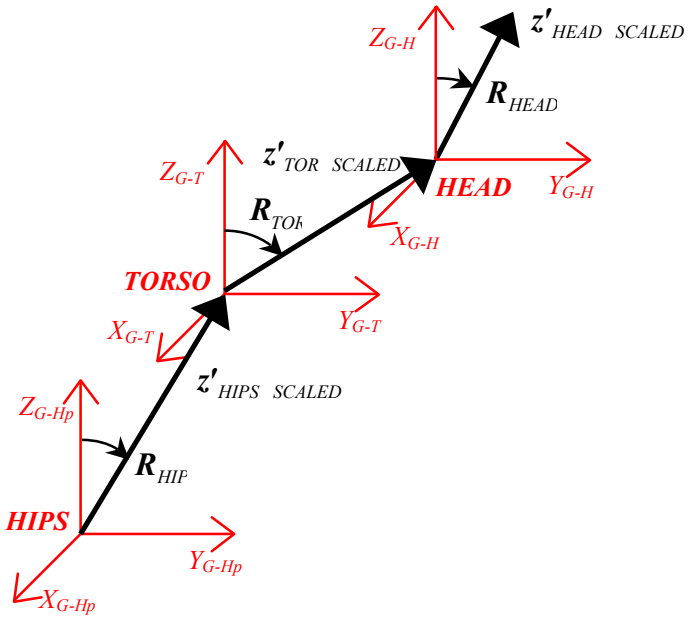

Figure 3.7 Vector description of overall CFP model of the spine with calibrated global coordinate frames for hips (*G-Hp*), torso (*G-T*), and head (*G-H*).

3.2.2 Relative orientation of spinal segments using vector model

Scaled orientation vectors, and the rotation matrices of the three segments expressed in the following notation, $\boldsymbol{R}_{HEAD} \equiv {}^{H}_{G}\boldsymbol{R}$, $\boldsymbol{R}_{TOR} \equiv {}^{T}_{G}\boldsymbol{R}$, and $\boldsymbol{R}_{HIPS} \equiv {}^{Hp}_{G}\boldsymbol{R}$, we can now express the

relative orientation relationships between the spinal segments. Note there are three global frames corresponding to each sensor. This new notation, ${}^{SEG}_{G}\boldsymbol{R}$, describes the rotation matrix of a spine segment in relation to its global reference frame *G-SEG*. To find the spine's relative rotation, flexion/extension and lateral bending angles between hips-torso, torso-head, and hips-head segments, the following relative rotation matrices are needed:

$$\text{From Hips to Torso: } {}^{T}_{Hp}\boldsymbol{R}={}^{G}_{Hp}\boldsymbol{R}\,{}^{T}_{G}\boldsymbol{R}={}^{Hp}_{G}\boldsymbol{R}^{-1}\,{}^{T}_{G}\boldsymbol{R} \tag{7a}$$

$$\text{From Torso to Head: } {}^{H}_{T}\boldsymbol{R}={}^{G}_{T}\boldsymbol{R}\,{}^{H}_{G}\boldsymbol{R}={}^{T}_{G}\boldsymbol{R}^{-1}\,{}^{H}_{G}\boldsymbol{R} \tag{7b}$$

$$\text{From Hips to Head: } {}^{H}_{Hp}\boldsymbol{R}={}^{G}_{Hp}\boldsymbol{R}\,{}^{H}_{G}\boldsymbol{R}={}^{Hp}_{G}\boldsymbol{R}^{-1}\,{}^{H}_{G}\boldsymbol{R} \text{ or } {}^{H}_{Hp}\boldsymbol{R}={}^{T}_{Hp}\boldsymbol{R}\,{}^{H}_{T}\boldsymbol{R} \tag{7c}$$

The transformation of these rotations into tilt/twist angles is presented in Sec. 3.3.

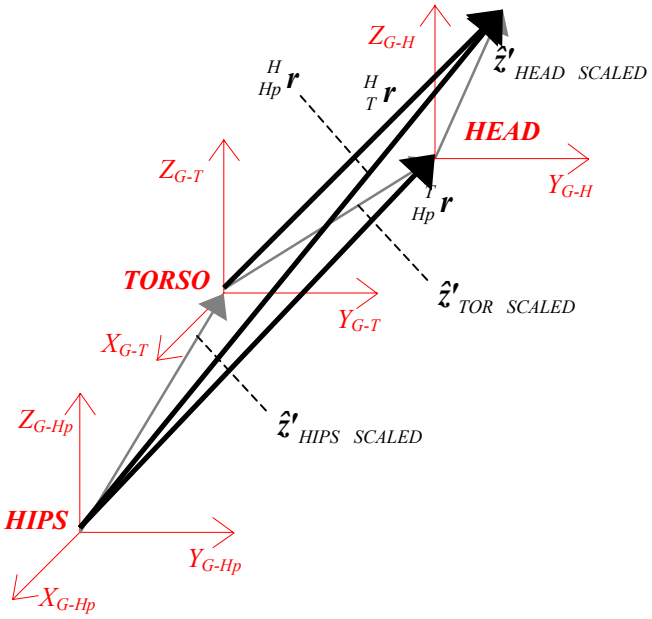

Figure 3.8 Vector description of the relative positions between the three spine segments.

Finally, in order to construct the overall motion of the interconnected spine segments the following relative position vectors need to be computed as well (see Fig. 3.8 for illustration):

$$\text{From Hips to Torso: } {}^{T}_{Hp}\boldsymbol{r}=\hat{z}'_{HIPS\ \ SCALED}+\hat{z}'_{TOR\ \ SCALED} \tag{8a}$$

$$\text{From Torso to Head: } {}^{H}_{T}\boldsymbol{r}=\hat{z}'_{TOR\ \ SCALED}+\hat{z}'_{HEAD\ \ SCALED} \tag{8b}$$

$$\text{From Hips to Head: } {}^{H}_{Hp}\boldsymbol{r}=\hat{z}'_{HIPS\ \ SCALED}+\hat{z}'_{TOR\ \ SCALED}+\hat{z}'_{HEAD\ \ SCALED} \tag{8c}$$

Later, in Sec. 3.4, these vectors will be used to generate an animated vector representation (AVR) of the overall spine motion in a GUI.

3.3 Tilt Twist Algorithm Implementation

Transforming the sensor data into tilt/twist notation allows us to intuitively measure the orientation of the spine segments (i.e. head, torso, and hips) in the world frame and relative to each other, together representing the full spinal orientation of the subject. The tilt/twist method [28] requires a defined initial (global reference) orientation unit vector ($\hat{z}_{SEG}$) and final orientation vector ($\hat{z}'_{SEG}$). See Appendix C for a full tilt/twist method description. The segment final orientation vector is continually output from the sensor at the specified sampling frequency and continually compared to the initial orientation world vector, set at calibration. The initial orientation vector for each sensor is set once during the first few seconds of the experiment.

With attachment and calibration to the body segment, the initial and final orientation vectors can then be described in terms of the tilt angle (ϕ_{SEG}), tilt azimuth angle (θ_{SEG}) and the twist (rotation) angle (τ_{SEG}), as shown in Fig. 3.9. For our measurements, the sensor Z'_{SEG}-axis and X'_{SEG}-axis is used to determine position and orientation of the spine segment, in combination with the tilt/twist transformation. From the initial calibrated global Z_{G-SEG}-axis position the measured 'tilt' range of the sensor Z'_{SEG}-axis from the initial position is 0 to 180 degrees (°) in any direction and is always a positive value. The following equations are used directly from the Tilt Twist method. Tilt can be calculated by using the projection of the sensor Z'_{SEG}-axis onto the global X-Y plane (X_{G-SEG}–Y_{G-SEG} plane in Fig. 3.9) requiring the use of the arc tangent function for all four quadrants ('atan2' command used in MATLAB) to accommodate sign variations:

$$\phi_{SEG} = \arctan\left(\frac{\hat{z}'_{SEG-Y}\sin\theta_{SEG} + \hat{z}'_{SEG-X}\cos\theta_{SEG}}{\hat{z}'_{SEG-Z}}\right) \tag{9}$$

where θ_{SEG} is the tilt azimuth angle given by:

$$\theta_{SEG} = \arctan\left(\frac{\hat{z}'_{SEG-Y}}{\hat{z}'_{SEG-X}}\right) \tag{10}$$

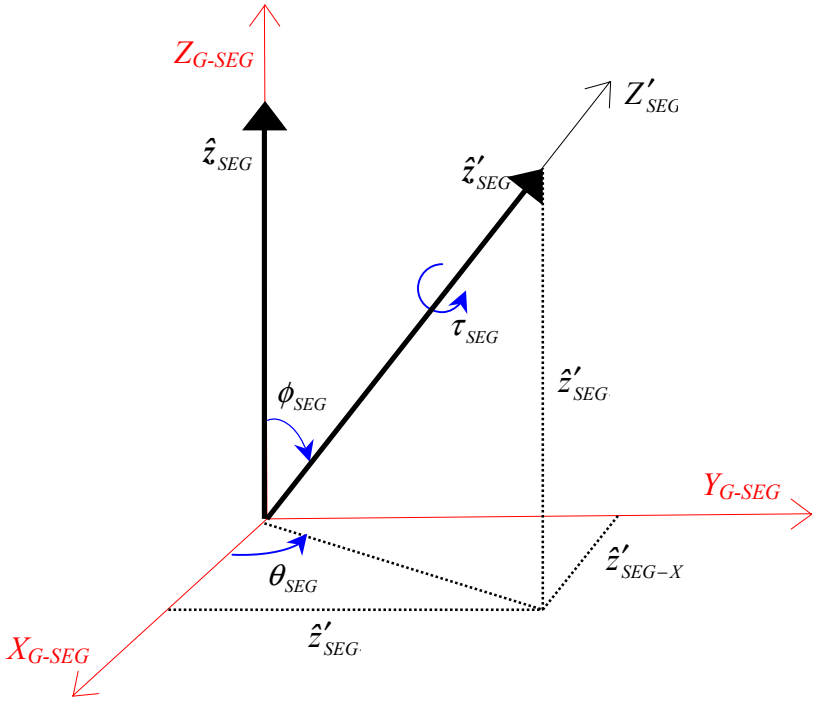

Figure 3.9 Spine segment's tilt (ϕ_{SEG}), tilt azimuth (θ_{SEG}) and the twist/rotation (τ_{SEG}).

The bending direction of the tilt is determined by the tilt azimuth angle θ_{SEG}. The azimuth angle is measured with respect to the positive Y_{G-SEG}-axis, with a positive counterclockwise (left turn) range to 180 ° and a negative clockwise (right turn) range to –180 °.

Once values have been obtained for the tilt and tilt azimuth angles we can express them in terms of the clinically meaningful parameters of flexion-extension and lateral bending. The flexion-extension angle, F_{SEG}, of a spine segment can be written as:

$$F_{SEG} = -\phi\cos\theta \tag{11}$$

where flexion is positive and extension is negative. The segment's lateral bending angle, L_{SEG}, can be written as:

$$L_{SEG} = -\phi \sin\theta \tag{12}$$

where right lateral bending is defined as positive. The twist angle τ_{SEG} represents the rotation (yaw) about the Z'_{SEG}-axis of the segment body from its initial position. This angle can be obtained from the initial and final values of the calibrated segments X_{SEG} − axis in the following manner:

$$\tau_{SEG} = arctan\left(\frac{\hat{x}'_{SEG-Y}}{\hat{x}'_{SEG-X}}\right) \tag{13}$$

The range of twist is −180° to 180°, with positive values in the counterclockwise direction from the mid-sagittal line (towards left) and negative values clockwise (towards right). As the tilt angle approaches 90° the location of the hatch mark degenerates and small variations in tilt produce large variations in twist. The twist (rotation) angle, τ_{SEG}, together with the tilt and tilt azimuth angle provide a complete description of the angular orientation of the segment.

3.4 Development of Graphical User Interface

To make the spinal motion measurements system commercially and clinically viable there is a need for an intuitive method by which to clinically interface with the devices. For preliminary demonstration, we have chosen to use MATLAB for the development of graphical user interface (GUI) for the spinal motion measurements system.

The MATLAB-based graphical user interface (GUI), which was developed with the help of Kevin Huang and Kel Sakaki of LACOBS, for the spinal measurement system allows the user to watch and analyze the real-time graphical representation of the spinal motion as the motion is performed, and includes 3D linear acceleration data for each spine segment in the display. The GUI has two main displays: *(i)* the one shown in Fig. 3.10 for generating the flexion, lateral bending and twist angles of the three spine segments in

real-time, as well as 3D linear acceleration data (*Ax*, *Ay*, *Az*) of the corresponding sensors; and *(ii)* the other shown in Fig. 3.11 for playback of the motion using an animated vector representation (AVR) of the spine for post analysis. As shown in Fig. 3.12, the AVR is a graphical illustration of the vector description of the CFP model representing overall spinal motion of the subject during movement.

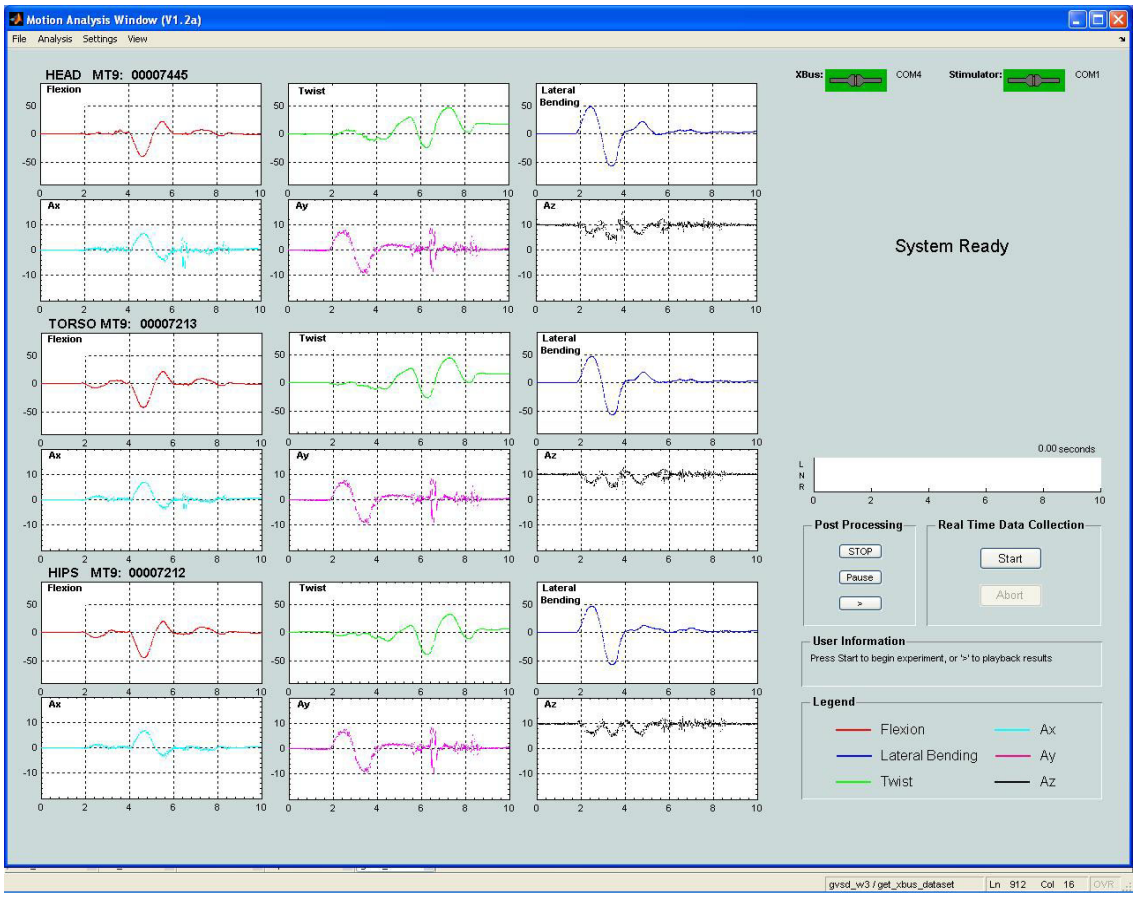

Figure 3.10 GUI window displaying real-time graphical representation of motion.

The playback window of the GUI, shown in Fig. 3.11, can also reprocess old data files while simultaneously animating the recoded motion with the AVR. The GUI includes an animated illustration of the vector representation of the spine. The GUI incorporates all algorithms presented in this chapter, and is a successful user-friendly method of recording, capturing and replaying spinal motion as recorded by the sensors.

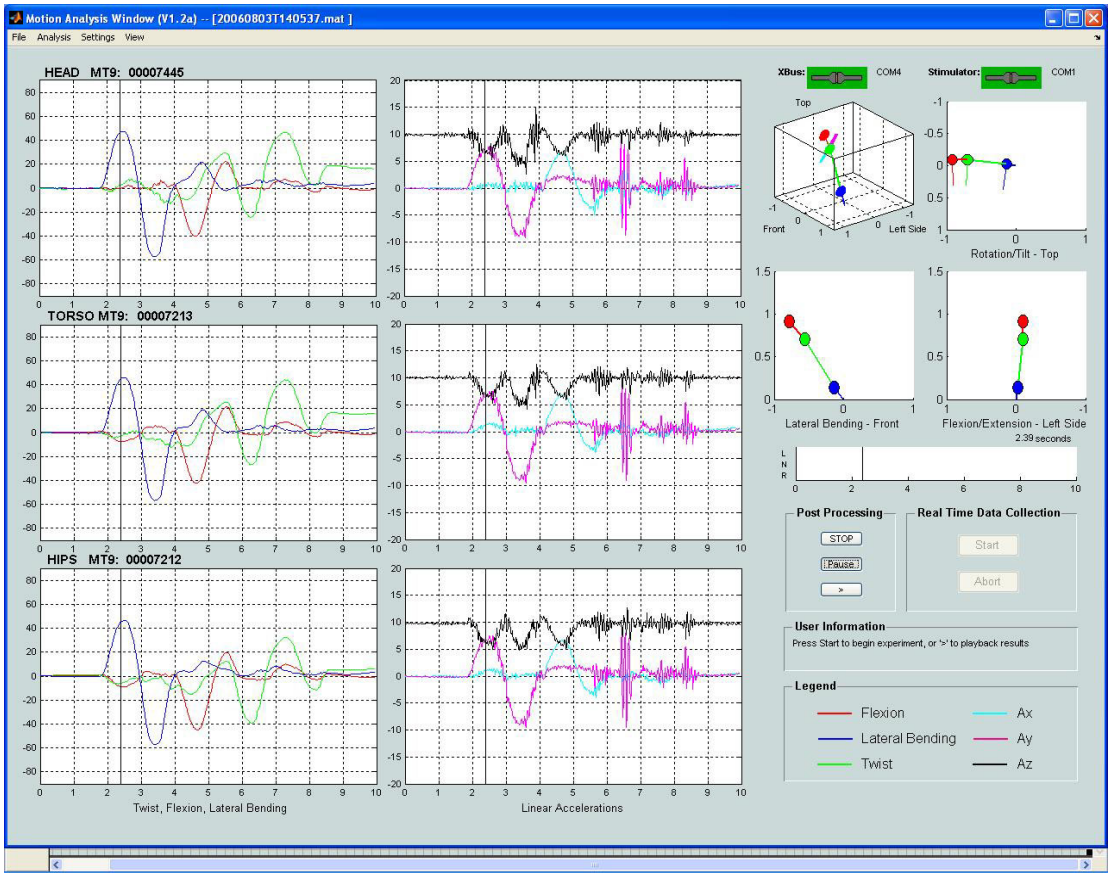

Figure 3.11 GUI playback window with animated vector representation (AVR) of the spine.

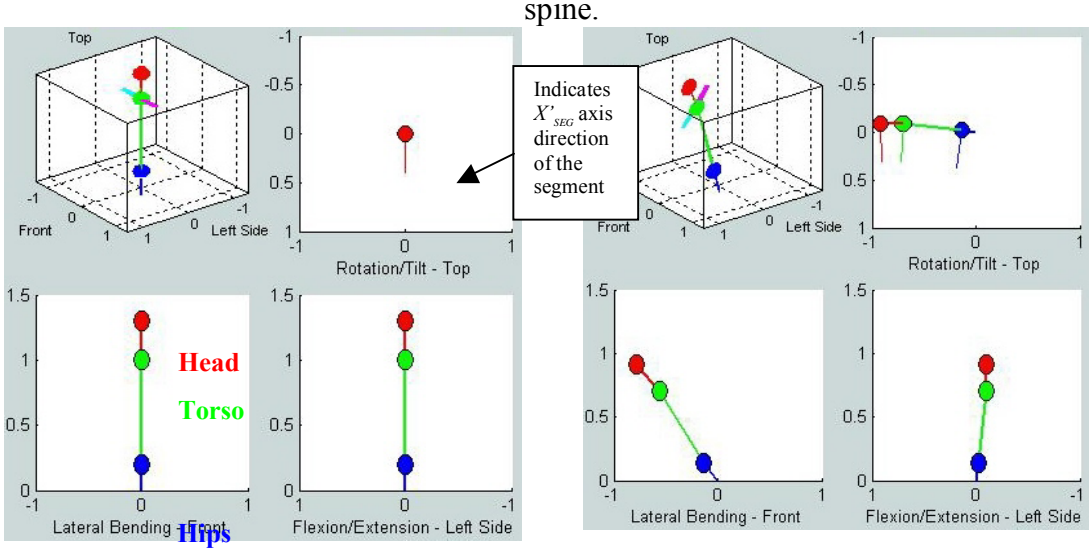

(i) *(ii)*

Figure 3.12 Close up view of AVR window during *(i)* initial position and *(ii)* motion.

Chapter 4

Experimental Setup

4.1 Sensor Placement and Calibration to Subject

Figure 4.1 shows the setup of the proposed spinal motion measurement system for subject testing. The first MT9 sensor is mounted to a light-weight plastic helmet worn on the head of the subject, with the sensor aligned horizontally with the Frankfurt plane (Fig. 4.2), and vertically with the frontal plane. The second MT9 sensor is attached to the torso of the subject, mounted on the back, approximately over the area between the 7th cervical vertebra (C7) and the 1st thoracic vertebra (T1), aligned with the mid-sagittal anatomical plane. The third MT9 sensor is placed over the hips, mounted on the lower back, approximately over the area of the 4-5th lumbar vertebra (L4-5) aligned with the mid-sagittal anatomical plane and the horizontal imaginary line between the highest tips of the iliac or pelvis bones. See Fig. 4.2 for the illustration of the anatomical planes. Placement of the sensors is based on the intuitive CFP visualization model, isolating one segment's movement from the others to obtain absolute and relative orientation information. Placements of sensors are considered unique for each subject. Subjects did not remove sensors during test, and movement of sensors was minimized with restraints. Future testing will involve the creation of a wearable apparatus that will allow the subject to remove and replace sensor with positional accuracy.

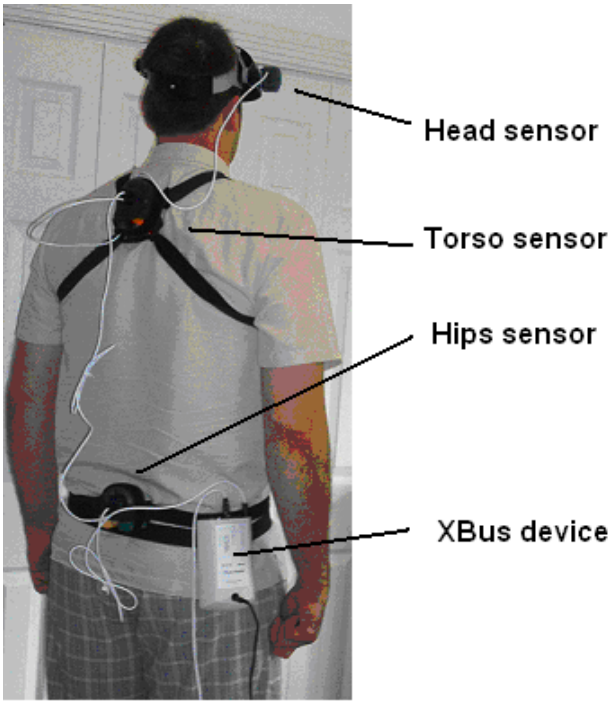

Figure 4.1 Spinal measurement system set-up for subject testing.

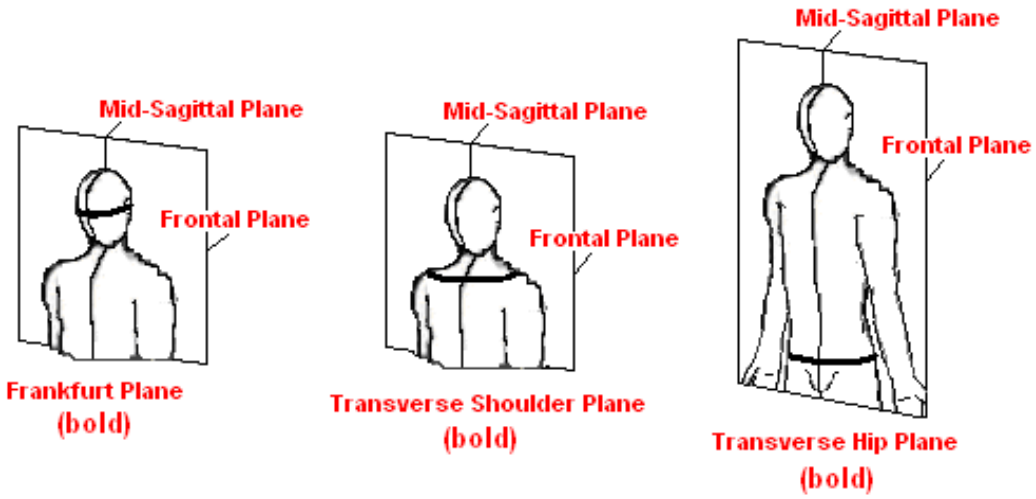

Figure 4.2 Anatomic planes for sensor alignment.

The torso and hip sensors are attached to the body using Velcro straps to place the sensors and housing comfortably. The sensor is housed in secure foam restraints using Velcro to eliminate slippage and maintain correct alignment of the sensor for calibration and measurement. The most critical part of the measurement is making sure the sensor

does not move with respect to the segment, once calibrated to the segment. Cables attaching the sensors to each other and the processing unit run between each of the components, minimizing interference in measurements by erroneous movement of the sensor and the possibility of restriction of subject motion. The sensor processing unit receives the rotation matrix, linear acceleration and rotational velocity signals from the each of inertial sensors and outputs the data to a PC via standard RS-232 interface.

4.2 Setup for Performance Verification

The goal of the performance verification step is to determine the accuracy of the proposed spinal measurement system, so that a high level of confidence can be obtained in the resulting measurements and processing algorithms. This is based on static magnetic compensation testing, and performance comparison against a standard optical motion measurement technique, the VICON motion analysis system.

4.2.1 Setup for magnetic compensation testing

Magnetic compensation testing is necessary to verify the compensation ability of the MT9 sensors to offset the effects of ferromagnetic disturbances present in the surrounding environment. The ferromagnetic disturbances affect the magnetometer measurements in the sensors, which are used to eliminate the yaw drift. The sensors come equipped with a magnetic compensation capability using a sophisticated Kalman filtering algorithm that can be enabled for use. Using a high-precision rotational table capable of ±180˚ in one plane, as seen in Fig. 4.3, static accuracy of the inertial sensor's yaw rotational measurement can be assessed. Recall that the accelerometers act as inclination sensors to correct for gyroscope drift in pitch and roll measurements, but leaves the yaw drift error uncorrected since the accelerometers cannot measure rotation about the vertical axis. Because the magnetic compensation ability of the sensors was supposedly limited, as explained by the manufacturer, we needed to determine the accuracy of the yaw measurements.

All three sensors were tested simultaneously, securely strapped together, and placed on the rotation table (made of aluminum and brass, which are non-ferromagnetic materials). The sensors were calibrated to the rotation table with the *x*-axes of the sensors and rotation table coincident. The results of the testing are presented in Sec. 5.1.

Figure 4.3 Magnetic compensation testing set-up for Xsens MT9 IMU.

4.2.2 Orientation measurement accuracy testing using VICON

Overall orientation measurement accuracy testing of the inertial motion measurement system was carried out using a VICON 460 optical motion tracking system, located in the Centre for Human Motion Analysis (CHUMA) at the Queen Alexandra Centre for Children's Health (QA). To record VICON measurements of the sensors, three reflective VICON markers were placed on the sensor fixture assembly to represent an *x*- and *z*-axis (see Fig. 4.4). Simultaneous recordings of body motion with the sensors and VICON optical system allowed us to compare the roll, pitch and yaw parameters obtained from each system. The inertial sensors directly output calibrated roll, pitch and yaw data. Transformation of the VICON data to roll, pitch and yaw parameters enabled us to directly compare the results graphically (presented in Sec. 5.2).

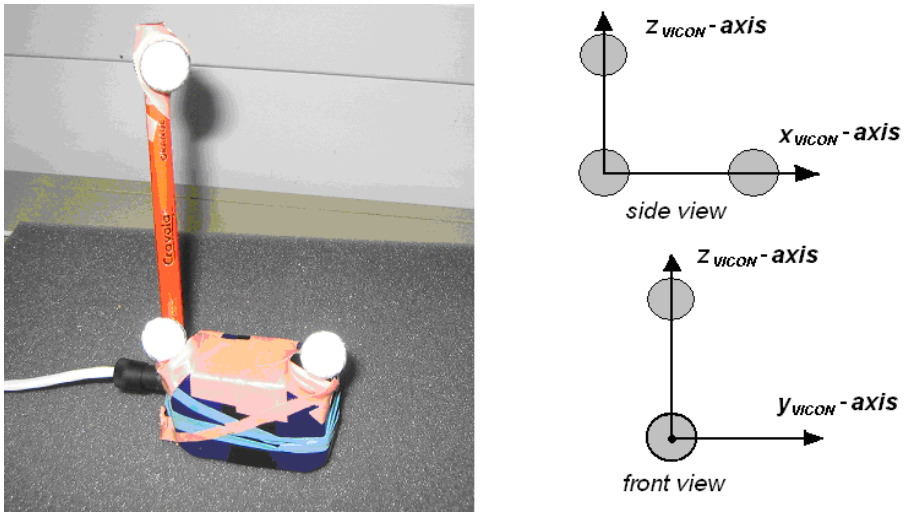

Figure 4.4 VICON marker placement and set up for simultaneous sensor and VICON motion capture.

Marker placement on the sensors were positioned by hand, set up to provide an orthogonal *z*-axis and *x*-axis. The markers are 10 mm reflective balls with a mounting platform to which sticky tape could be attached. The most accurate motion capture by the VICON system is when the VICON cameras can see the markers throughout the entire motion, avoiding positional interpolation for missing markers based on geometry relating the markers to each other, by the VICON software. As long as the majority of VICON cameras can see the markers they will record their locations in space. The inherent weakness of the technique is the occlusion of markers during motion. For simplification, the motions used in the verification process have been divided into three groups corresponding to head motion, torso motion and hip motion respectively, with the motions of less than 180° around each axis (roll, pitch, yaw) as subject range of motion permits. The VICON system outputs the absolute coordinates of the markers in space relative to its calibrated global coordinate frame origin. The global coordinate frame is determined during camera set-up, via a static and dynamic system calibration which sets the motion volume space, and calibrates the cameras to effectively capture motion of the markers within the set volume (see Fig. 4.5). The sensor/segment coordinate frame is calibrated to the VICON global coordinate frame by aligning the segment's initial position as near as possible to VICON global coordinate directions. The VICON capture

volume is set to capture motion of a subject wearing one sensor at a time, with the sensor no higher than 4 feet off the ground.

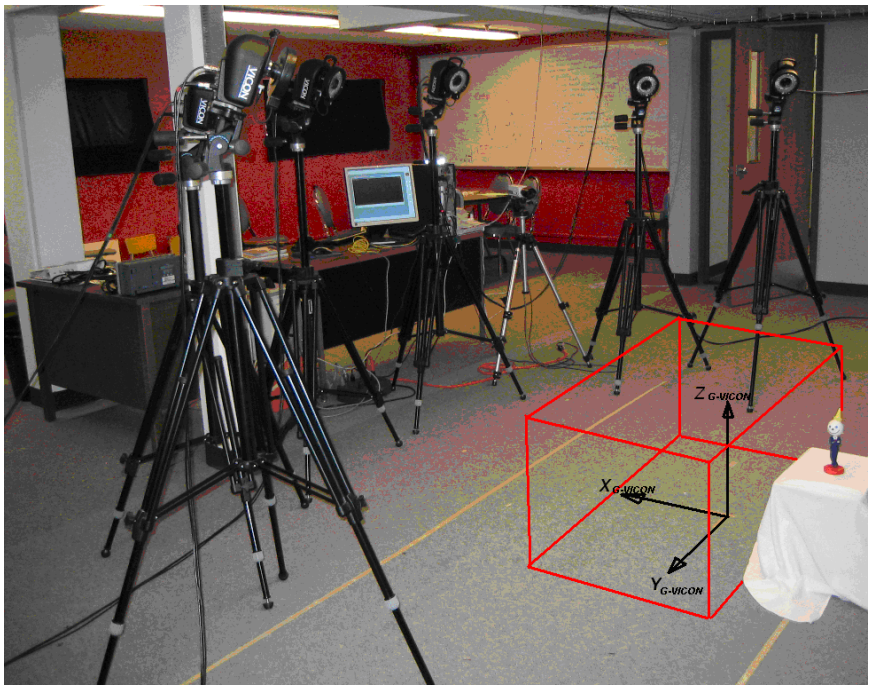

Figure 4.5 VICON camera set-up with VICON global axes, and VICON motion volume box.

The VICON verification specifically tests each sensor/segment individually on the body as the subject moves through a 'natural' motion range such as nodding the head, looking around, or balancing on one leg. During motion the VICON system calculates the position of each marker on the sensor relative to the origin of the VICON global coordinate frame, as seen in Fig. 4.5. With the position of each marker known we can construct a *z*- and *x*-axis from the marker data, representing the sensor in VICON space. We represent these constructed axes as x_{VICON} and z_{VICON}., with the global VICON axes represented as $X_{G-VICON}$, $Y_{G-VICON}$ and $Z_{G-VICON}$ (Figs. 4.4 and 4.5). Consider each marker labeled as P1, P2 and P3, as seen in Fig. 4.6.

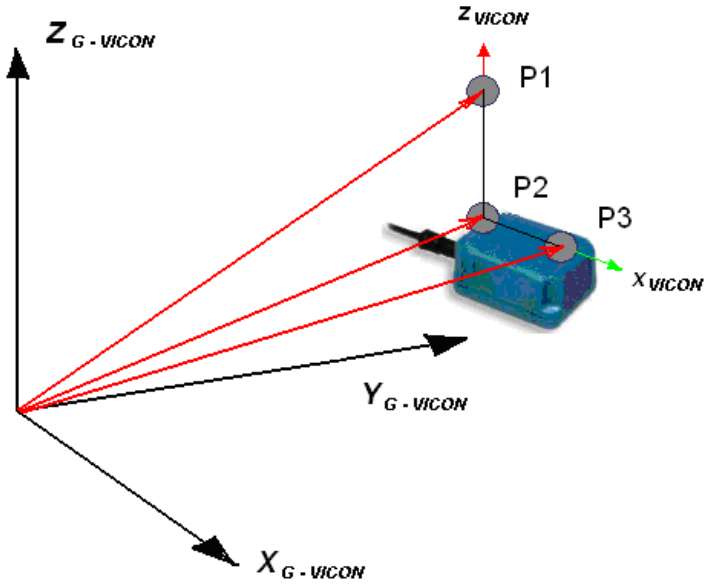

Figure 4.6 Markers on sensors in relation to VICON global coordinate frame.

With the marker positions known and measured relative to the VICON global coordinate reference axes and origin, the position vectors constructed from the marker data can be calculated and used to obtain the roll, pitch and yaw of the sensor/segment motion. It is important to align the sensor axes to the VICON coordinate reference axes during initial sensor calibration as this, along with orthogonal marker axes, will result in the most coherent data. Each marker set (P1-P2, P2-P3) allows us to assemble orientation vectors of the sensor as represented by the VICON system. For example, to determine $\boldsymbol{x}_{VICON}$ of the sensor we subtract the P3 *x*-coordinate from the P2 *x*-coordinate, the P3 *y*-coordinate from the P2 *y*-coordinate, and the P3 *z*-coordinate from the P2 *z*-coordinate:

$$\boldsymbol{x}_{VICON} = (P3_x - P2_x)\hat{\boldsymbol{i}} + (P3_y - P2_y)\hat{\boldsymbol{j}} + (P3_z - P2_z)\hat{\boldsymbol{k}} \tag{14}$$

The same is done to obtain $\boldsymbol{z}_{VICON}$, by subtracting the P1 *x*-coordinate from the P2 *x*-coordinate, the P1 *y*-coordinate from the P2 *y*-coordinate, and the P1 *z*-coordinate from the P2 *z*-coordinate:

$$\boldsymbol{z}_{VICON} = (P1_x - P2_x)\hat{\boldsymbol{i}} + (P1_y - P2_y)\hat{\boldsymbol{j}} + (P1_z - P2_z)\hat{\boldsymbol{k}} \tag{15}$$

The roll parameter is measured using the z_{VICON} vector, whereas the yaw and pitch parameters are measured using the x_{VICON} vector. By measuring pitch using the x_{VICON}

vector and not the z_{VICON} vector, we reduce singularities that occur when human motion results in a pitch of > 90°. Because the inertial MT9 sensor measures pitch and roll opposite to the right-hand-rule convention, the VICON measurement of roll and pitch will be of the opposite sign. This is fixed by the simple strategic placement of a negative sign in the VICON roll calculation. For the transformation algorithm of VICON output to roll, pitch and yaw parameters, please see Appendix B. The results of the VICON testing described in this section are presented in Sec. 5.2.

4.3 Development of a Galvanic Vestibular Stimulation Device

The GVSD was designed and prototyped (shown in Fig. 4.7) in parallel to the spinal motion measurement system by Ed Haslam and Ian Soutar of LACOBS under the Dr. Park's direction. As discussed in Sec. 2.3.1, the design parameters for the GVSD are based on the need for a commercially viable, portable stimulation device capable of safely delivering controllable amounts of current to the human vestibular system by way of electrodes placed on the mastoid processes (behind each ear).

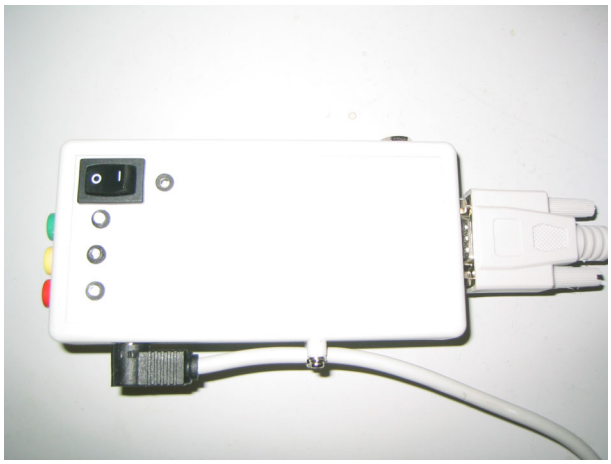

Figure 4.7 Prototyped AC galvanic vestibular stimulation device (GVSD).

The goal of this design phase was to set design parameters for the GVSD that will fulfill current and voltage requirements and begin preliminary testing. The circuit is designed to have a maximum average current of 5 milliamps (mA), with a maximum drive voltage of

24 volts (V), resulting in a design that has low risk for the subject, without the possibility of serious electrical shock. The GVSD design is capable of driving three electrodes to achieve our desired GVS stimulation parameters of bilateral bipolar GVS, bilateral monopolar GVS, and unilateral monopolar GVS (see Fig. 4.8, which is a duplication of Fig. 1.3). One electrode is placed behind each ear on the mastoid process, with the third (if used) placed on the neck. Bilateral bipolar GVS involves one anodal electrode behind on ear with the cathode electrode behind the other, with the third grounding electrode placed on the neck. Bilateral monopolar GVS involves respective electrodes of the same polarity (anode or cathode) behind each ear, with the third grounding electrode on the neck. Unilateral monopolar GVS has a stimulating electrode at one ear. The combination of these three types of GVS creates eight possible GVS scenarios (or modes) in total, which, in theory, can induce a sway response of the subject in every direction (see Fig.1.4).

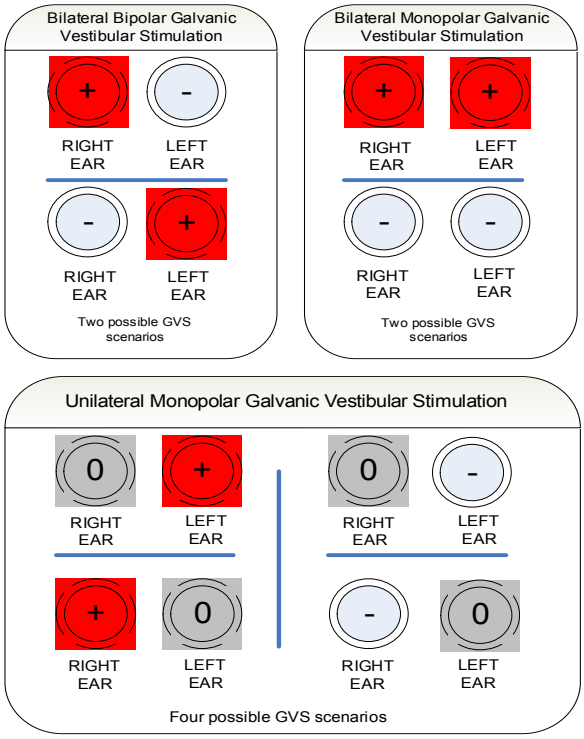

Figure 4.8 Desired GVS stimulation parameters for GVSD, '+' represents anode, '-' cathode and '0' is no electrode.

The nominal electrode current is between ±0-4 mA, with ±1-2 mA the average optimal stimulation current seen in similar GVS research. For our purposes our maximum most

positive current is 5 mA. The challenge is to overcome the effects of skin resistance seen in DC current based stimulation devices which require large unsafe stimulation currents and voltages to achieve optimal stimulation current set points. To meet this challenge of skin resistance a current source that is switched between a programmable maximum value and ground potential at a selectable frequency is employed. This modulates the direct current to create an alternating current (AC) waveform providing the desired current at the electrodes with much lower driving voltages.

The resulting AC-based GVSD is ideally capable of providing output signals of zero volts/zero current, a constant current set point, or a waveform that ranges between zero volts (zero current) and a maximum programmed current value within our current range. The possible waveforms can be sine, square, triangle or stochastic, programmed to have a frequency of up to 300 Hertz (Hz). A second method used to reduce skin resistance is to minimize resistance between the electrode and the skin; this has been accomplished through the choice of electrodes and the use of conducting gel. The electrodes and conducting gel chosen have been recommended by experts in the stimulation field.

The GVSD has a separate GUI that runs in a Visual Basic program, which was written by Kevin Huang of LACOBS. It is still undergoing human subject testing by Dr. Tim Inglis' human neurophysiology research group at UBC, and not reported in this thesis.

Chapter 5

Experimental Results

Subjects recruited for the experimental testing presented in this chapter have all satisfied the requirements of no history of back pain or problems, no balance disabilities, no leg pain, and no postural impairments. A human ethics approval (protocol number 2006-36) for this research was obtained from the Ethics Board representing joint council of the University of Victoria and the Vancouver Island Health Authority (VIHA).

Subjects were recruited to participate in the human testing to perform basic motion tasks while wearing the proposed spinal measurement system. Subjects were asked to stand or sit in the calibration 'resting' position for the first few seconds of the experiment to align sensor and object coordinate axis as well as set the segment world axes. Once the sensors were calibrated to the subject, the subject performed a series of tasks incorporating head, torso, and hip motions at various speeds. The three sensors were mounted to the subject as already outlined in Sec. 4.1 (see Fig. 4.1).

5.1 Magnetic Compensation Testing Results

The setup for the magnetic compensation testing was described in Sec. 4.2.1. Typical results obtained can be seen in Fig. 5.1, where the grey bars represent the range from ±85-95° in which the sensor readings should respectively peak in uniform agreement. The important relation to note is whether all three sensors reach the same peak values. The first inverted peak (Peak A) in the graphs, represents a 90° turn to the right, the second positive peak (Peak B) a turn to the left. Both turns were executed by hand and are approximate.

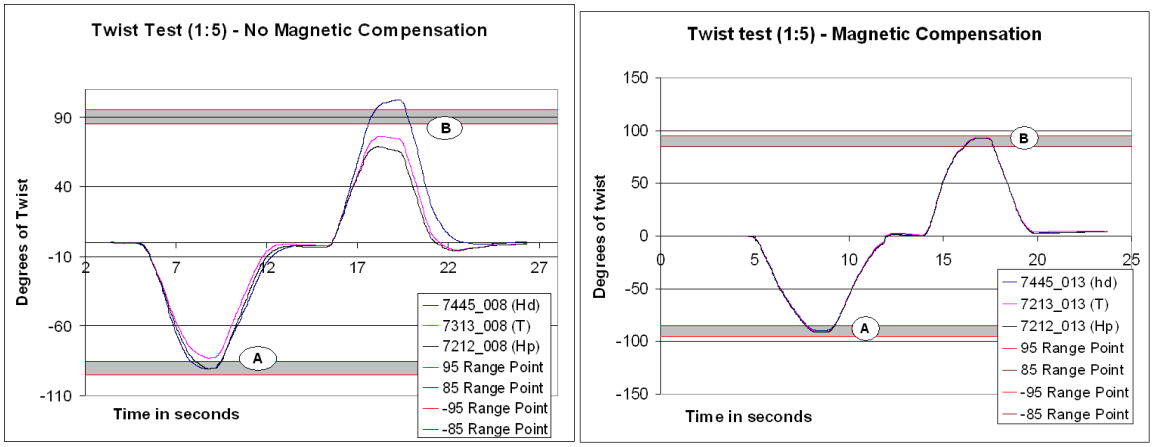

Figure 5.1 No magnetic compensation (left), and magnetic compensation (right), typical results.

Each test is designated with a sensor and test number of the format 7XXX_XXX, with the first four digits representing the sensor, and the last three digits representing the test number. All three sensors are run for each test, and remain consistently associated with their designated body position, i.e. the head sensor is designated as sensor 7445, the torso sensor as sensor 7213, and the hips sensor as sensor 7212, regardless of the fact they are currently unattached to the body during magnetic compensation tests.

The maximum and minimum peak values of each sensor were used to calculate a standard deviation for each peak for the three sensors. For example, the standard deviation in test _017 of Peak A for all three sensors (designated _017A) was 0.75°,

which is plotted in Fig. 5.2 (left). The magnetic compensation tests were run sequentially (i.e. _013 was the first test and _017 the last). Test _013 was run approximately 60 minutes after the sensors were turned on and calibrated to the rotational stage. Test _014 occurred at approximately 180 minutes, with subsequent Tests _015 and _016 occurring 185 and 190 minutes after sensors turned on and calibrated to gauge the effect of long sensor runtimes. The sensors were turned off for several minutes before restarted and recalibrated to the rotational stage for Test _017, from which it can be seen there was a significant drop in deviation (see Fig. 5.2). This is as expected as the zero-frequency offsets are removed. Note that for all tests the temperature remains consistent, with no significant ambient variations over the test period.

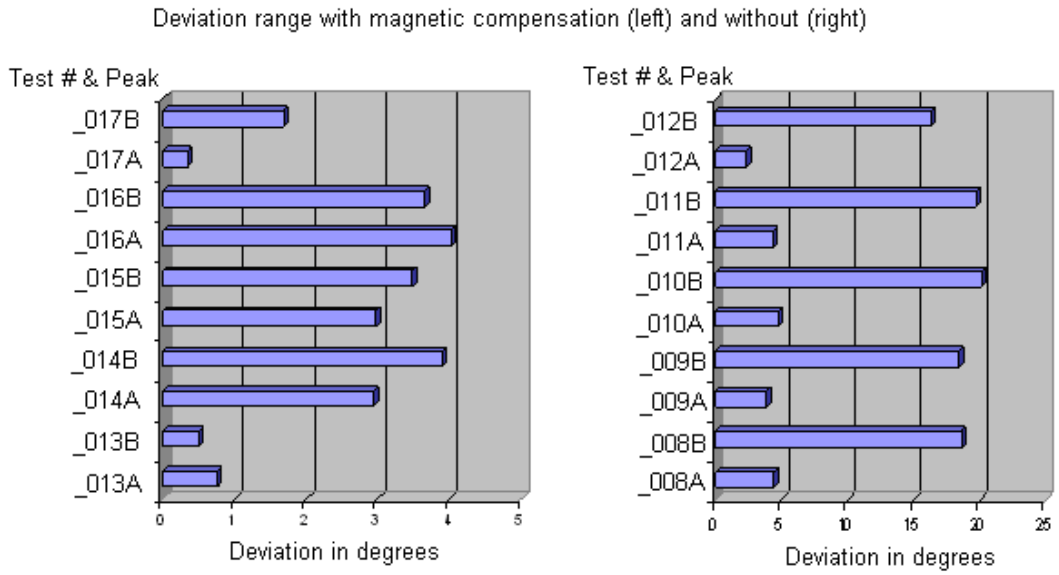

Figure 5.2 Standard deviation results of magnetic compensation tests, left graph denotes results with magnetic compensation, and right graph denotes non-compensated results.

A second set of five tests (_008 to _012), also shown in Fig. 5.2 (right) were run without magnetic compensation enabled, for the same motion of ±90°. Without magnetic compensation it can be seen that the standard deviation increases dramatically. All five tests run were run within one hour, and the sensors were not recalibrated during that time. Measurements of rotation (yaw), without magnetic compensation, exhibited significant drift from the expected values with a standard deviation (at Peaks A and B) of 11.3° over 5 trials. The exact cause of larger deviation at Peak B is unknown, but it would likely be

due to the presence of a larger magnetic disturbance in the test room towards that direction. With magnetic compensation activated the average standard deviation was 2.4° over 5 trials, with an approximate deviation increase from 0.73° to 2.4° noted after 3 hours of continuous monitoring. The increase was removed if the sensors were turned off for 30~60 seconds after 3~4 hours of continuous use, with deviation returning to less than 1°. The magnetic tests show that yaw compensation of the sensors is suitably accurate within 1-2 hours of continuous use. For all subsequent trials magnetic compensation has been enabled and trial times are less than one hour.

5.2 Results of Orientation Accuracy Testing Using VICON

The VICON setup for verifying the inertial sensor's orientation accuracy was described in Sec. 4.2.2. The VICON system was set to simultaneously start when the inertial sensors were triggered to begin recording data. This allowed for simultaneous time units between the VICON and inertial sensors. Once started, the inertial sensors are calibrated and the task motions begin.

Each sensor, attached to the head, torso, or hips, was tested individually with the VICON system. The subject was first asked to wear the head sensor (sensor 7445) to run through a set of three trials involving range-of-motion tests. Following tests required the subject to wear the torso (7213) and hip (7212) sensors respectively. For all trials the parameters of roll, pitch and yaw were output from the sensor and calculated from the VICON marker data.

5.2.1 VICON verification of head motion

For the head motion trials, with the rest of the body motionless, the subject went through roll, pitch and yaw of natural head motions of no greater than 90° to avoid occlusion problems with the VICON motion measurements. Roll, pitch and yaw were used as a less complicated output of the sensors to avoid error introduction during verification comparison. Any head motion approaching 90°, if possible, required mathematical

correction and estimation of the 'lost' marker position, automatically done by the VICON software. Head motion followed the basic pattern of *(i)* yaw right then left, *(ii)* pitch down then up, and *(iii)* tilt left then right. All three parameters are output simultaneously from the inertial sensor. All three parameters can be calculated from VICON data and compared to the inertial sensor (i.e. MT9) result graphically, as shown in Fig. 5.3. Subsequently, Fig. 5.4 shows a direct comparison of VICON and inertial parameters. Note that the inertial sensor graph shows the calibration alignment to the object in the first few seconds of the trial.

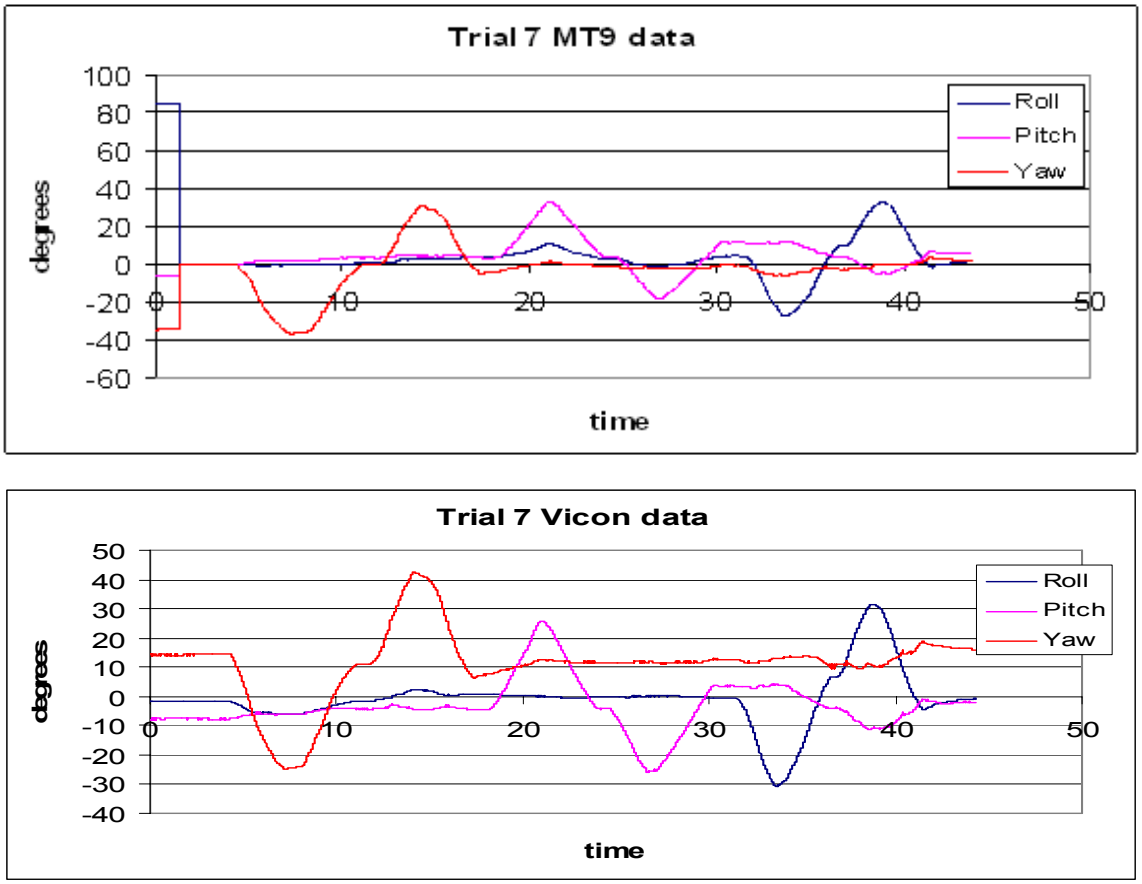

Figure 5.3 Head motion VICON verification trials, *(top)* direct sensor (MT9) output of head motion, and *(bottom)* direct transformation of VICON data to roll, pitch, and yaw parameters.

The results of the comparison between the VICON data and the inertial sensor data show an offset distance between the two (Fig. 5.4). The non-aligned results, between the sensor and VICON values, for all head trials is an average offset of 3.72° in roll, 5.18° in pitch,

and 12.64° in yaw. The non-aligned offset between the sensor and VICON values seen in the graphs remain fairly consistent after calibration, meaning if there is a 5.6° offset at calibration, the offset remains fairly consistent throughout the experiment. These offsets can be directly attributed to the misalignment of the sensor global frame and the VICON global frame.

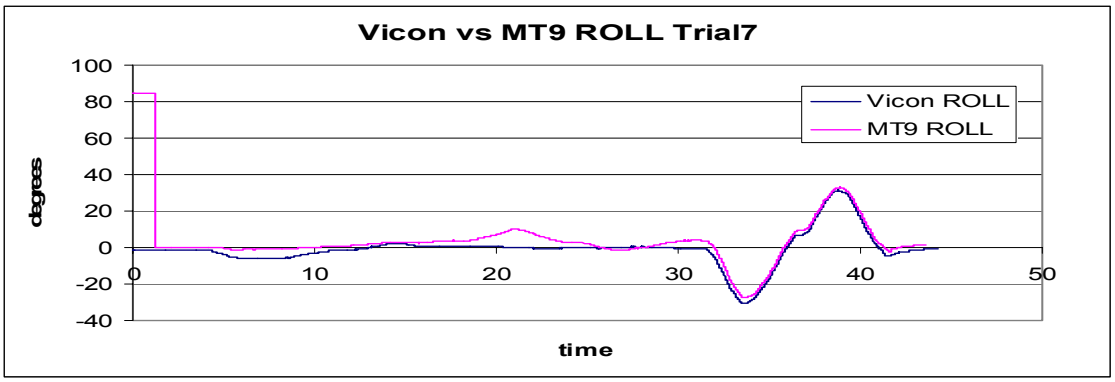

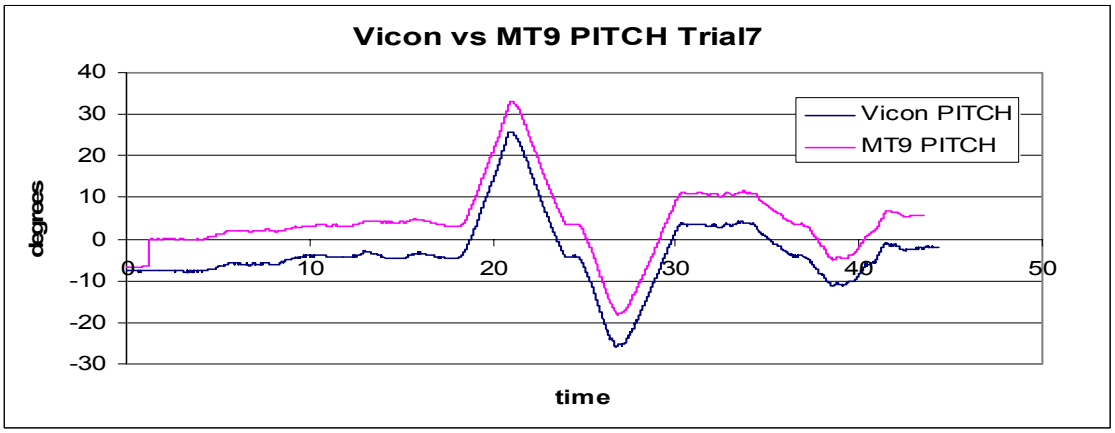

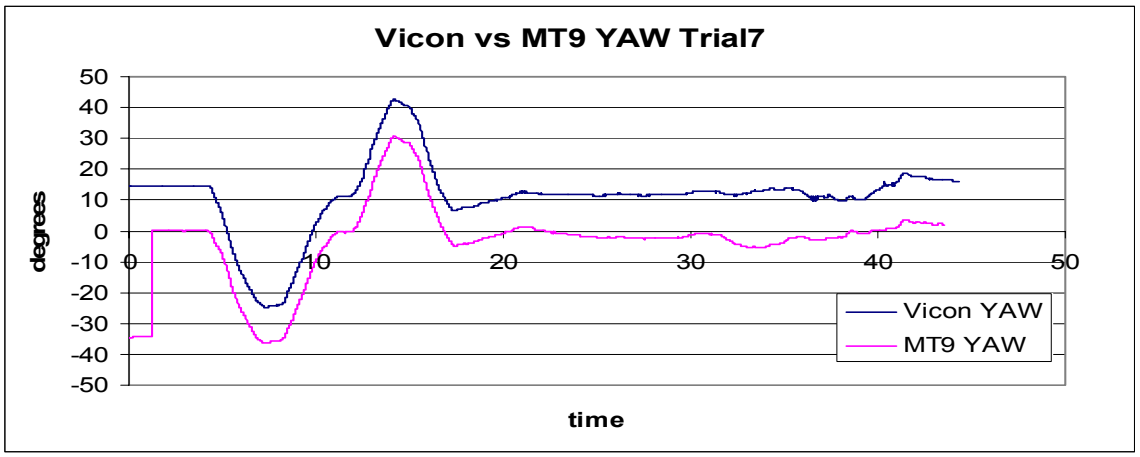

Figure 5.4 Comparison of head roll, pitch and yaw between sensor (MT9) and VICON results.

By calculating the offset orientation between the sensor and VICON global axes, easily obtained during the few seconds of initial calibration, the data can be manually 'aligned' by subtracting or adding the difference in alignment from the results. Once done, the aligned global sensor axes and the global VICON axes are equivalent in orientation. With aligned global axes the roll average offset decreased to 1.49°, the pitch average offset to 0.73 °, and the yaw average deviation to 0.86 °. Typical offset compensation results can be seen in Fig. 5.5.

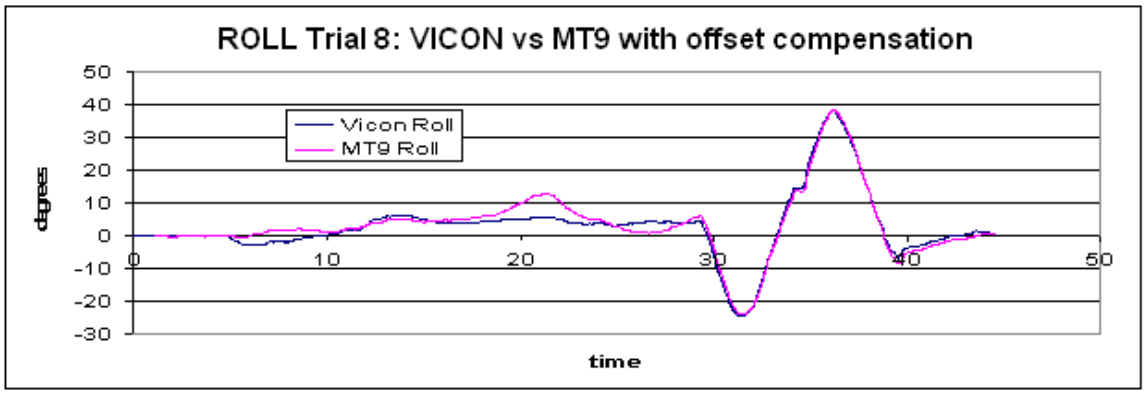

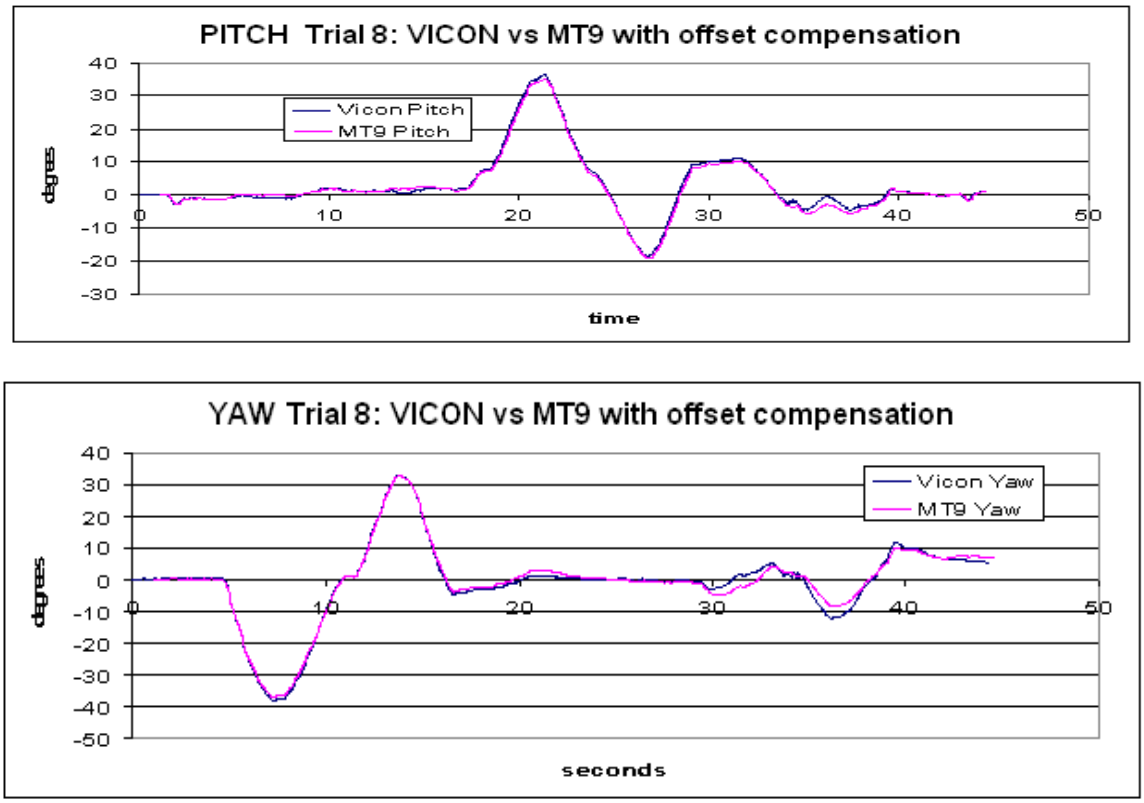

Figure 5.5 Comparison of head roll, pitch and yaw between sensor (MT9) and VICON results, with offset compensation.

5.2.2 VICON verification of torso motion

For the torso motion trials the subject went through roll, pitch and yaw of natural torso motions no greater than 90° to avoid occlusion problems with the VICON motion measurement system. The hips were held to natural anchored position during the motion (i.e. standing or kneeling in one spot while performing torso motions). Any motion over 90° required mathematical correction and estimation of the 'lost' marker position. In order to enable the VICON software to estimate lost markers, the researcher must re-identify the lost marker using software tools. The time consuming process resulting in position estimation can be removed by staying within a 90° motion range. Torso motion recorded followed the basic pattern of *(i)* yaw right then left, *(ii)* pitch forward then back, and *(iii)* tilt right then left.

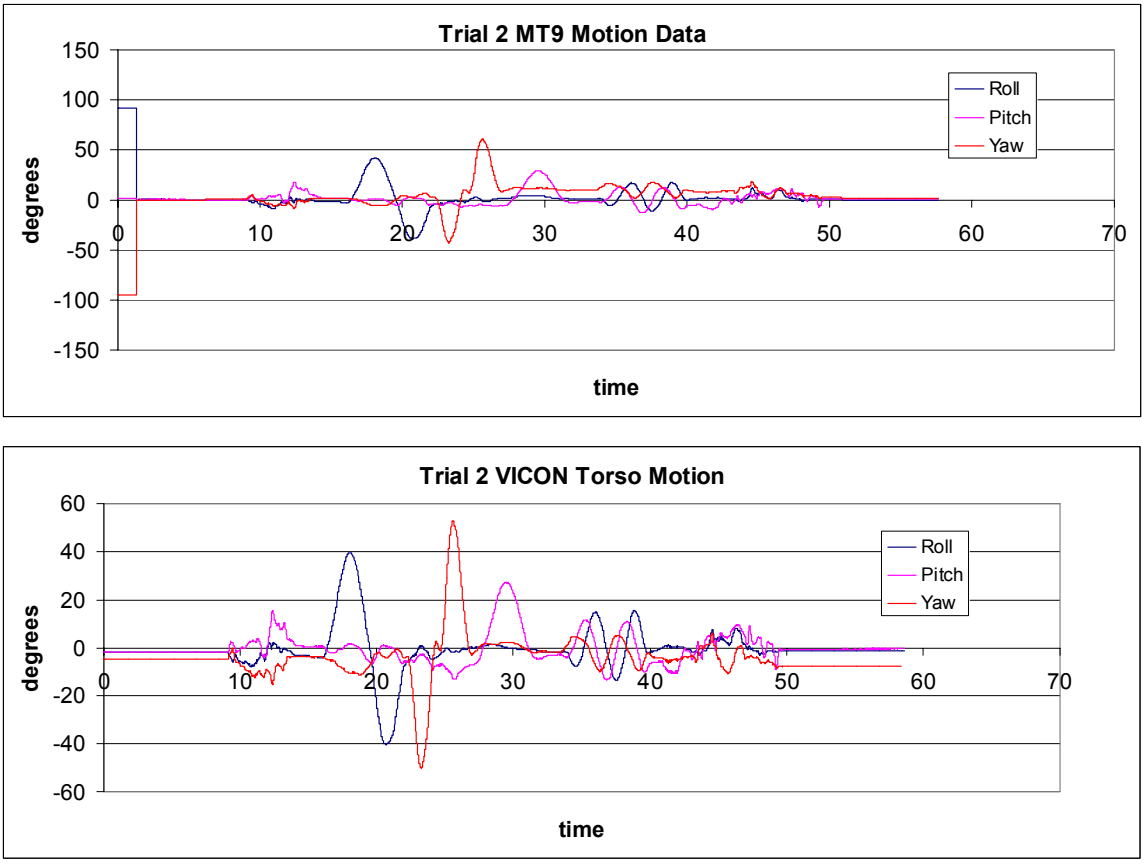

Figure 5.6 Torso motion VICON verification trials, *(top)* direct sensor (MT9) output of torso motion, and *(bottom)* direct transformation of VICON data to roll, pitch, and yaw parameters.

In addition to the basic roll, pitch, and yaw motion of the torso, two clockwise tilt rotations of the torso were performed while sitting in the same position as the other motions, motions seen between 32 and 40 seconds in Fig. 5.6. Following the two clockwise tilt rotations, the subject breathed as deep a breath as possible while sitting in an upright position (simply to see what data resulted), seen between 40-43 seconds in the same figure. The first (after calibration) and last motions of the sensor are those involved in taking the sensor to/from the torso and placing from/on the ground.

The non-aligned results for the torso trials is an average offset of 1.54° in roll, 1.21° in pitch, and 8.2° in yaw. When the two global frames were aligned, the roll average offset decreased to 0.68°, the pitch average offset to 0.76°, and the yaw average deviation to

2.82°. Typical results for aligned global axes (denoted 'offset correction' in graph labels) can be seen in Fig.5.7.

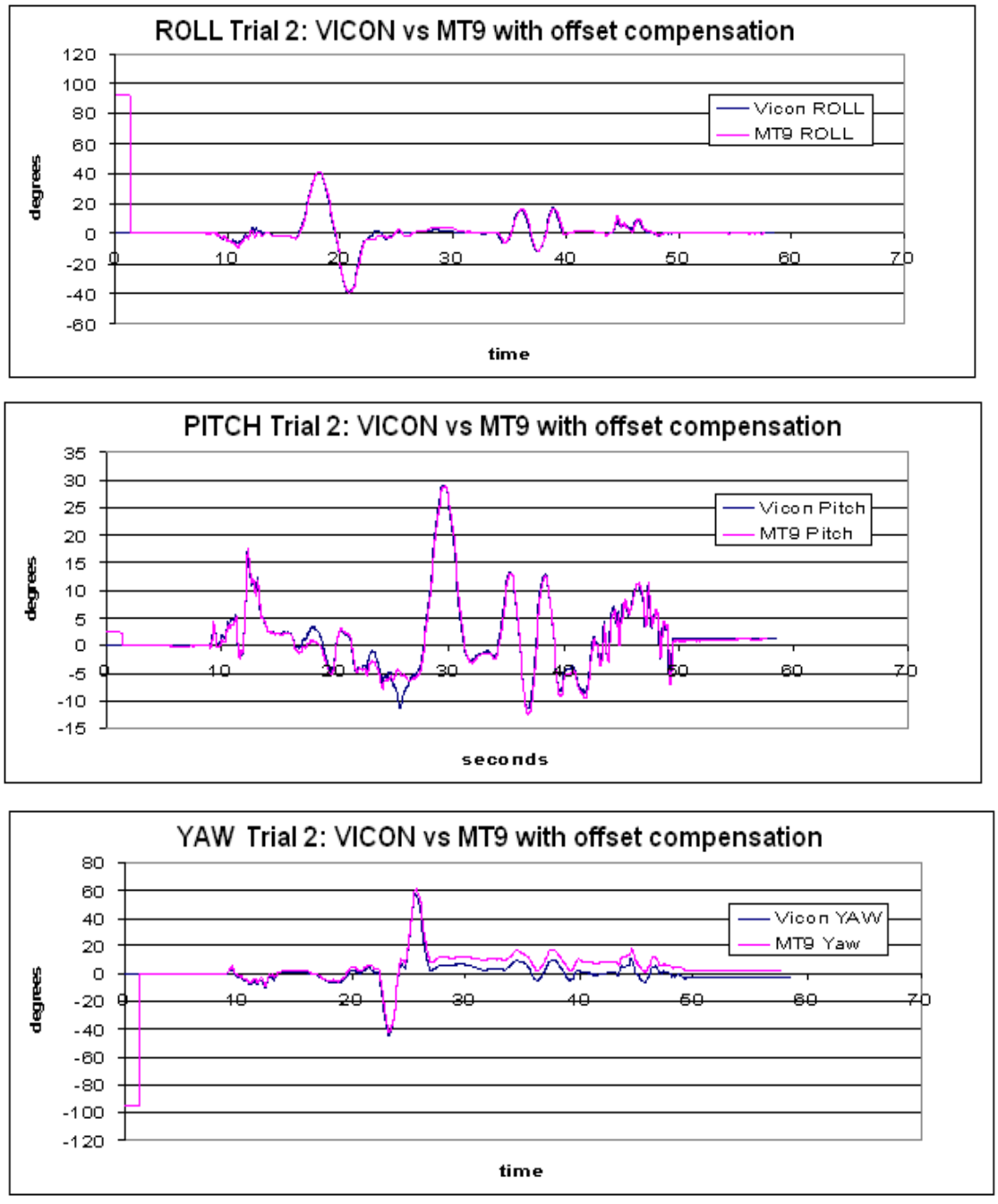

Figure 5.7 Comparison of torso roll, pitch and yaw between sensor (MT9) and VICON results, with offset compensation.

5.2.3 VICON verification of hip motion including speed trials

For the hip motion trials the subject went through roll, pitch and yaw of natural hip motions no greater than 90° to avoid occlusion problems with the VICON motion measurement system. Any motion over 90° required mathematical correction and estimation of the 'lost' marker position by the VICON system.

The hips were held to a naturally constrained position during the motion by keeping the knees placed firmly on the ground. Recorded hip motion included *(i)* yaw fast and slow, *(ii)* pitch, and *(iii)* tilt right and left. In addition to the basic roll, pitch, and yaw motion of the hips, speed trials were added – i.e. rotating the hips as fast as possible between slow rotation motions. The rotation (yaw) motion for the hips was easiest to control at speed. Results obtained from the sensors and calculated from VICON vector positional data are seen in Fig. 5.8.

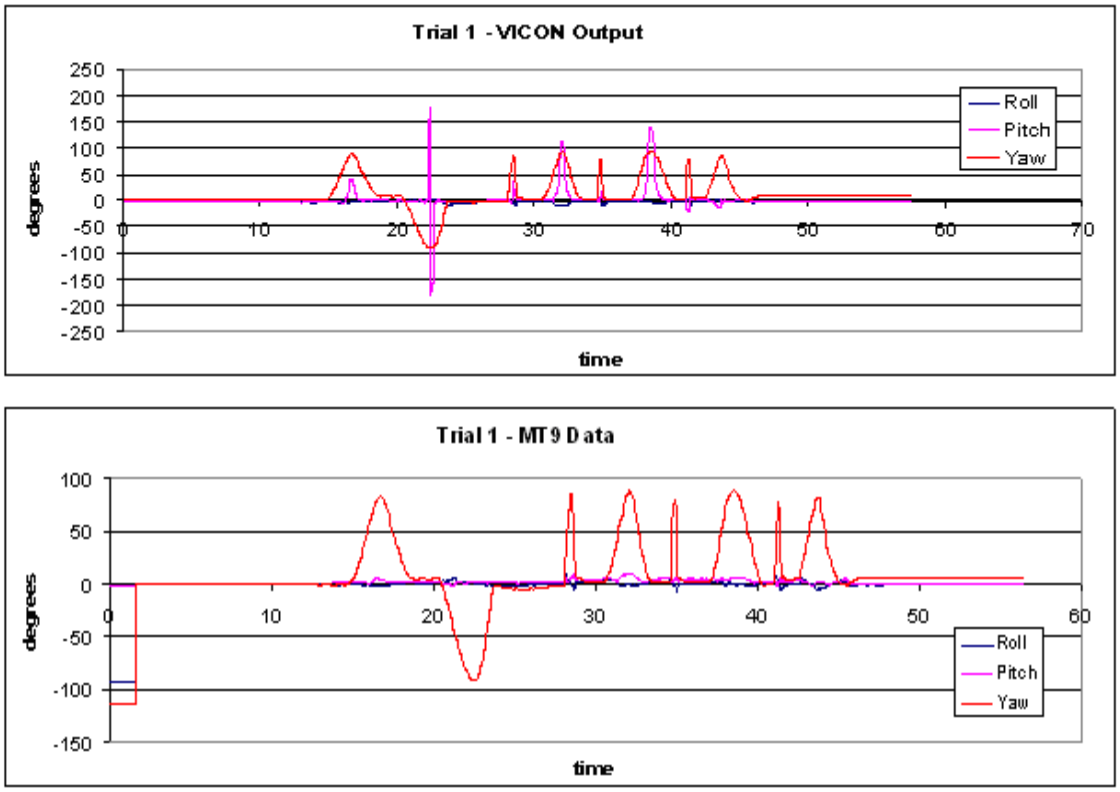

Figure 5.8 Hips motion VICON verification trials, (top) direct sensor (MT9) output of hips motion, and (bottom) direct transformation of VICON data to roll, pitch, and yaw parameters.

The sensors had no problems with fast motions, as verified by the VICON results. However an abnormal, though not unexpected, behavior was noted in the VICON data. Because we have chosen to calculate pitch using the $\boldsymbol{x}_{VICON}$ vector the calculation has an inherent singularity whenever $\boldsymbol{x}_{VICON}$ pitch approaches 90°. The reason is that the pitch angle (β) is calculated using Eq. (16) below, using the z and x component of $\boldsymbol{x}_{VICON}$; and when yaw approaches 90° the x component of $\boldsymbol{x}_{VICON}$ approaches zero, resulting in a false large variations of the pitch angle. Note again that in the *atan2* function is used in processing.

$$tan\beta = \left(\frac{x_{VICON-z}}{x_{VICON-x}} \right), \tag{16}$$

This type of singularity would also cause a problem with the yaw (α) calculation in Eq. (17) when pitch approaches 90° for the same reason. These singularities effect only the VICON results, the inertial sensors show no singularities of his type.

$$tan\alpha = \left(\frac{x_{VICON-y}}{x_{VICON-x}} \right) \tag{17}$$

The non-aligned results for the hip trials had an average offset of 3.1° in roll, 7.8° in pitch and 2.25 ° in yaw. When the offset between the two global frames was incorporated into the data (global axes aligned), the roll average offset decreased to 0.82°, the pitch average offset to 6.5°, and the yaw average deviation to 1.7°. Offset compensation typical results can be seen in Fig. 5.9. Note that the VICON pitch results suffer from large deviations (circled parts of Fig. 5.9) due to singularities.

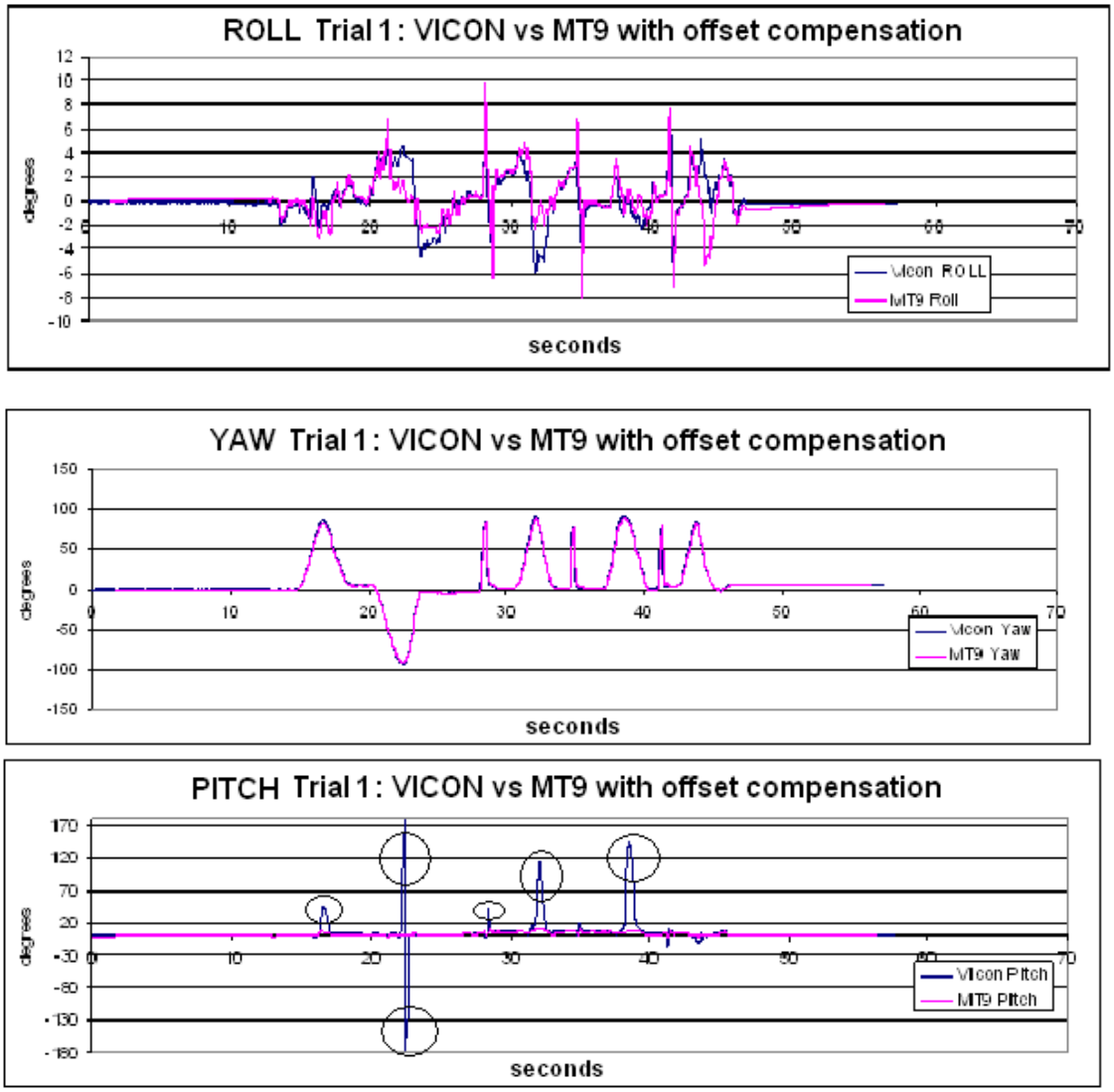

Figure 5.9 Comparison of roll, pitch and yaw between sensor (MT9) and VICON results, with offset compensation data.

5.3 Spinal Motion Analysis

The next step is to record the spinal motion of subjects engaged in a set of three motion tasks while wearing all three sensors. Each task is repeated a minimum of three times by the subject consecutively, in as close to exact order of motions, with the sensors recalibrated at the beginning of each task and iteration. The first task required the subject to stand beside (left side) a chair, move to sit in the chair, pick up a pencil on the floor to

the right side of the chair, sit back up, and then place the pencil on the floor on the left side of the chair, then stand up and return to the initial position beside the chair (without stepping on pen). The second motion involved bending down to pick up a 6 lb ball on the floor directly in front of the subject, hold the ball waist height against the body for a moment, then return the ball to the floor and resume standing relaxed position. The third motion requires the subject to step up onto a 9 inch platform, and then step back down.

Implementation of the tilt/twist algorithm to transform the rotational matrix output by each sensor has resulted in the following motion convention outlined in Table 5.1, which will assist in reading the following graphs.

Table 5.1 Motion convention key

Motion	Positive	Negative
Rotation	Towards left side	Towards right side
Flexion/Extension	Flexion	Extension
Lateral bending	Towards right side	Towards left side

The first task (Task #1) has a large lateral bending component, both to the right and left as the subject bends to pick up and place the pencil on the floor from the sitting position. Four trials were recorded for Task 1, and typical lateral bending results are presented in Fig. 5.10. For full results please see Appendix D.

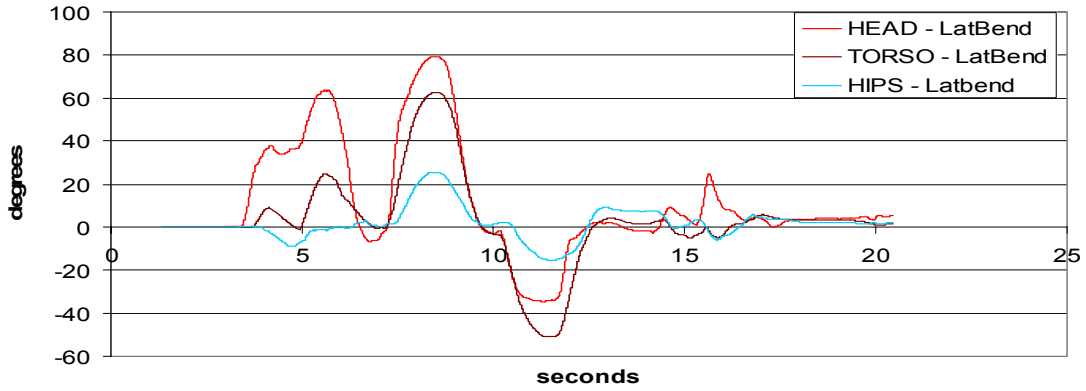

Figure 5.10 Sitting motion task (Task #1) analysis lateral bend components for all three spine segments.

The results show expected representation of the subject as they go through the first task. Progressing through the balance task the subject's head will turn to look at the chair, watching the chair as they sit, a motion seen in the results Recall lateral bending is a motion of leaning to the right or left along the medial plane. The graph shown in Fig. 5.10 is typical of the lateral bending results obtained for this task. Fig. 5.11 shows the typical rotational and flexion component obtained for Task 1. For additional graphical results please see Appendix I.

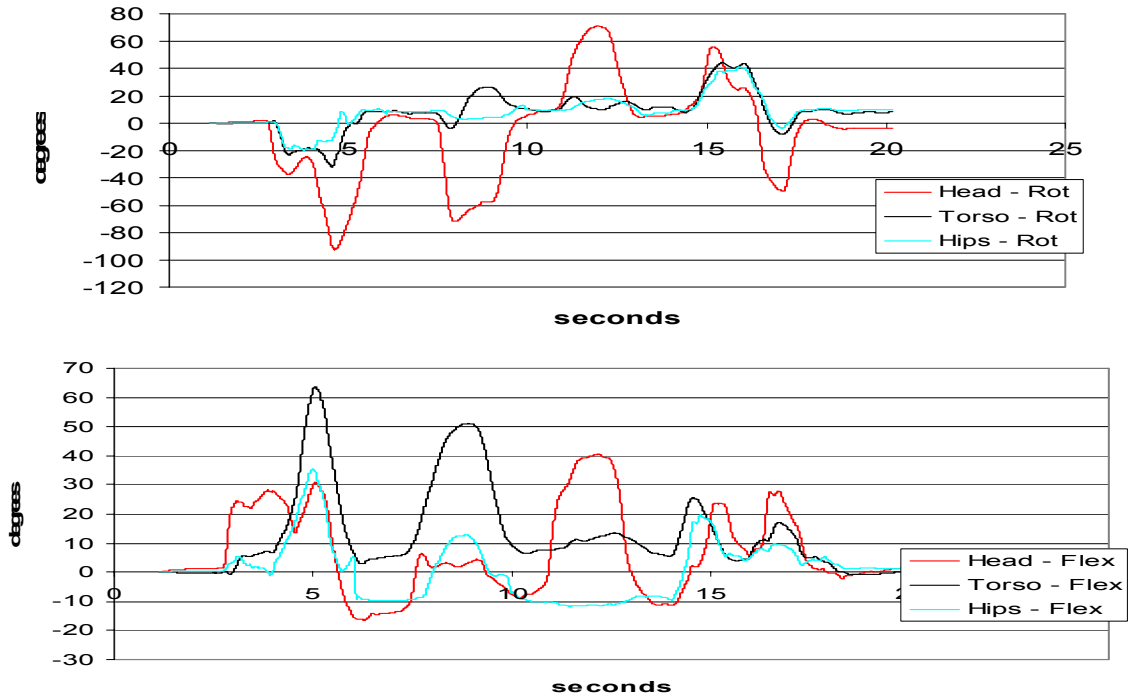

Figure 5.11 Sitting balance task (Task #1) rotational (top) and flexion-extension (bottom) components for all three spine segments.

The second task (Task #2) has a large flexion-extension component as the subject is required to bend down and pick up a 6 lb ball placed on the floor, hold the ball for a pause at waist height, and then return the ball to the floor. The results for flexion-extension are as expected for this balance task motion, seen in Fig. 5.12. For additional graphical results please see Appendix J.

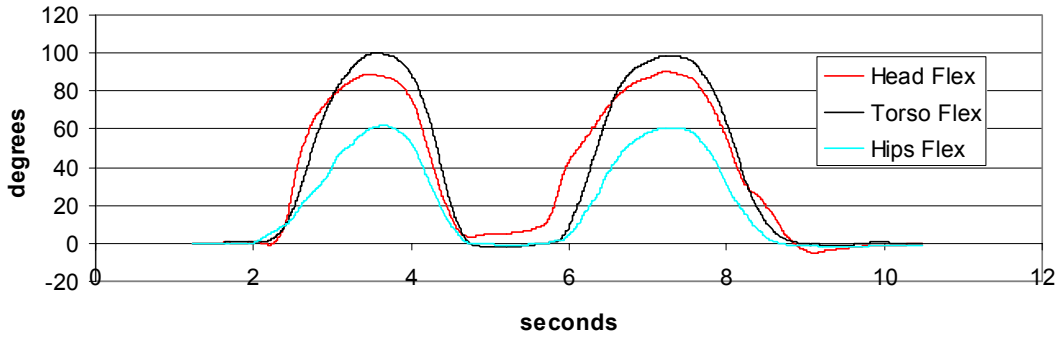

Figure 5.12 Ball balance task (Task #2) flexion-extension components for all three spine segments.

The third task (Task #3) is a stepping motion, requiring the subject to step up onto a 9 inch platform, pause, and step back down. The graph shown in Fig. 5.13 is typical of the results obtained for this task. For full graphical results please see Appendix K.

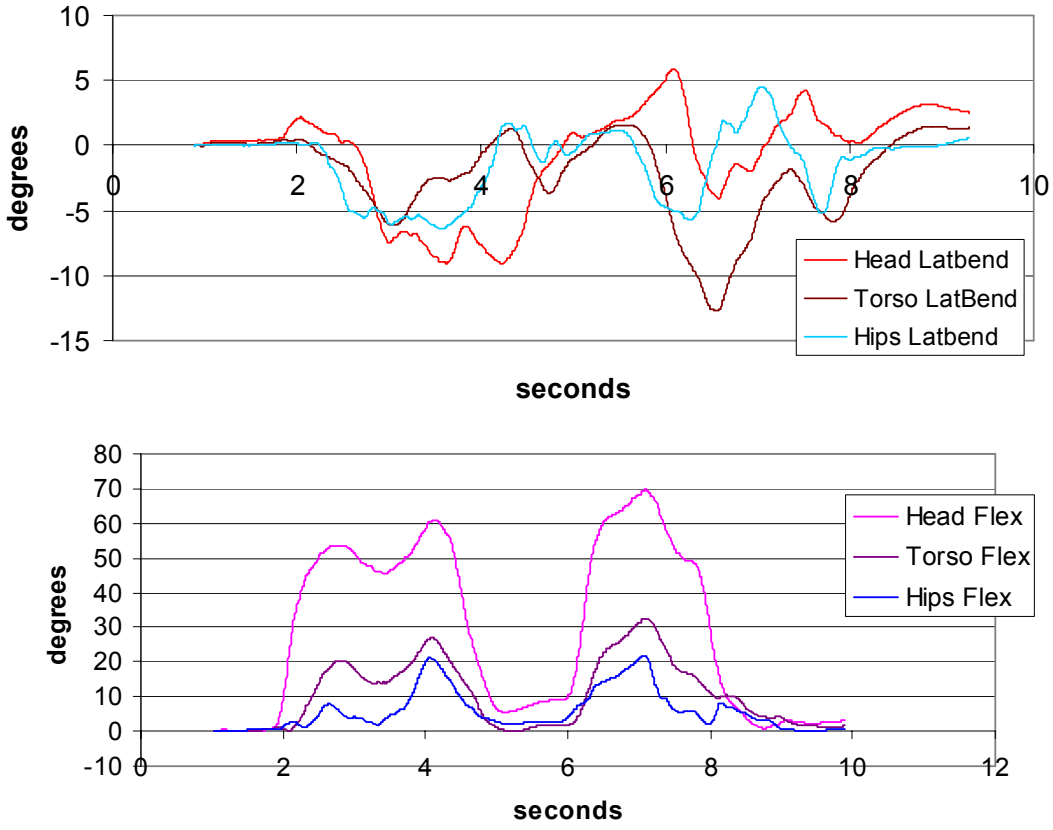

Figure 5.13 Stepping up onto platform balance task (Task #3) lateral bend and flexion components for all three body segments.

The ball task and step task were very similar for a purpose: to isolate flexion in one motion to less than 90° (the step task, Task #3).Without constraining motion of the torso and hips, the sensors now experience motion >90°. In particular, the motion task involving picking up a ball (Task #2) results in the head sensor experiencing a pitch (forward tilt) of >90°, resulting a singularity not seen in previous data. This singularity was first noted in the rotational data of the Task #2 trials (Fig. 5.14), which showed a large rotational component for the head and torso, abnormal for a flexion dominant motion where the body should have minimal rotation. The rotational component of all segments should have been within 5-10° at most, to account for natural motion.

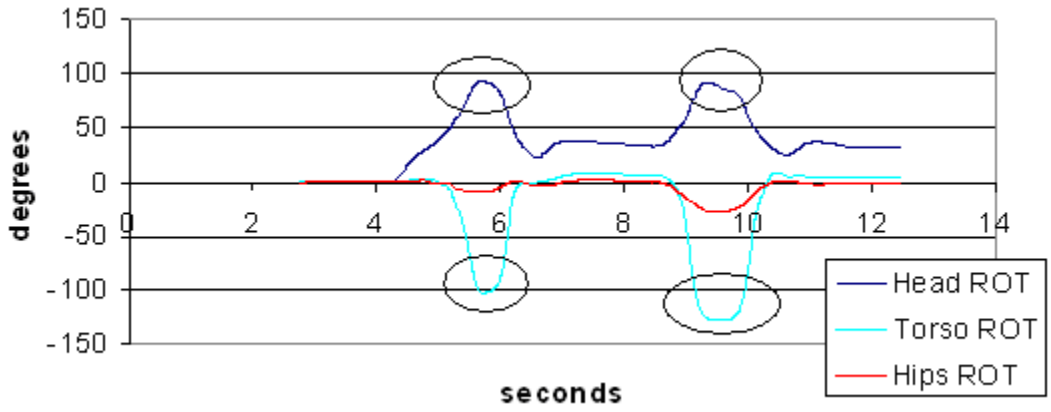

Figure 5.14 Abnormal (as circled) rotational motion of head and torso noted in Task #2 results.

After examination of the data it was noted that any pitch motion approaching 90° will result in abnormal rotational values. To test this finding a series of tests were performed using the sensor's SDK to eliminate the possibility this error was a result of post-processing of the sensor data (tilt/twist transformation algorithms, etc.). All three sensors were strapped together such that they would all experience the same motion, once calibrated to each other.

The motion tested was the troublesome pitch motion, when the sensors were moved from the calibrated position of 0°, rolling them to >90°, back to 0, and roll to >-90°. As the results show in Fig. 5.15, the sensors did each experience a pitch motion of near exact magnitude, with a positive peak at 87° and a negative peak at -86°. However, while the

pitch motion should show minimal yaw and roll of no greater than 10°, Fig. 5.16 shows the abnormal large changes in the roll and yaw data (the circled portions in the figure).

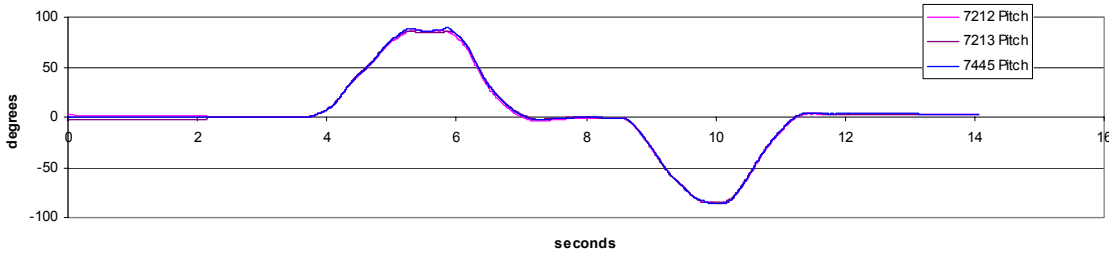

Figure 5.15 Pitch test motion results for head sensor (7445), torso sensor (7213) and hips sensor (7212).

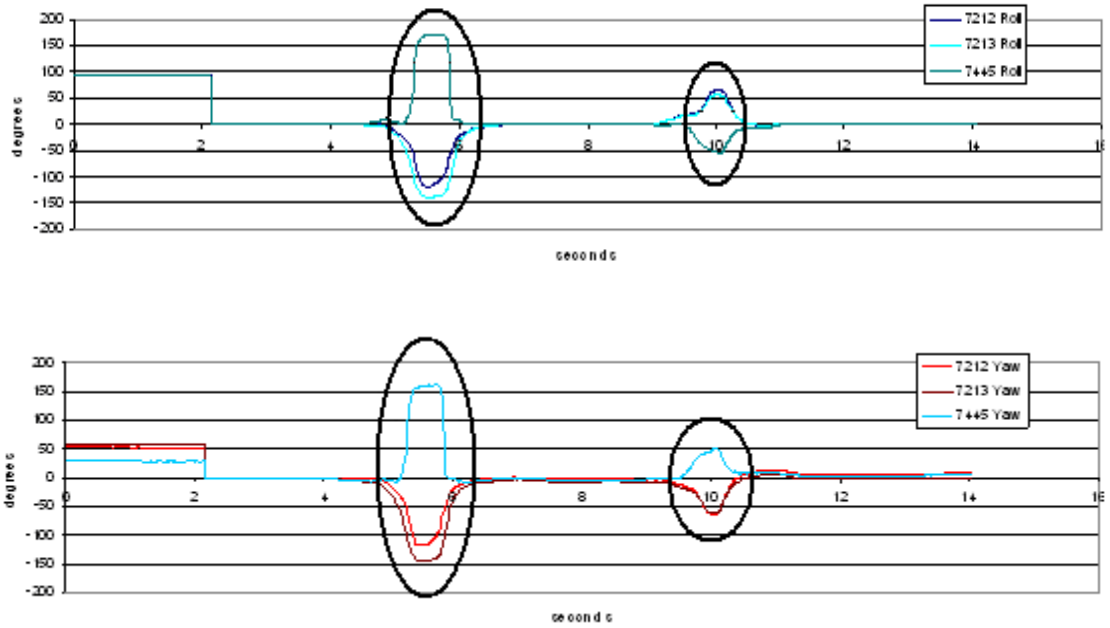

Figure 5.16 Roll and yaw test motion results for head sensor (7445), torso sensor (7213) and hips sensor (7212).

Using graphical analysis, we note that pitch values above 71° or below -60° the readings of roll and yaw are compromised, with minor effects showing at pitch values as low as ±50°. The result from this preliminary test indicates a singularity present before the processing algorithms, for roll, pitch and yaw parameters. The significance of these results do not effect VICON verification, as all VICON tests did not exceed a pitch range > ±40°, therefore the yaw and roll results were not compromised. Recall that VICON

testing measured the motion range of one segment (head, torso or hips) individually, with constraints, resulting in a much smaller range of motion.

With these results we can now direct the search for the singularity to examination of the rotational output of the SDK, after transformation into tilt/twist parameters via the tilt twist method [28], as done for Tasks #1-3. The purpose of this test is to determine how the observed anomalies seen in the pitch data (using roll, pitch and yaw sensor output, in Fig. 5.16) and the transformed rotational data are related. One sensor, calibrated and mounted to the head via the helmet fixture, was used for the tests.

The first test involved pitch motion of the sensor (head), down then up, with peak magnitude less than ±45°. The results are well within expected values for human motion of the head, showing no obvious singularities. While looking down the head tilts slightly to the left, while looking up the head tilts to the right, and the rotation of the head remains fairly constant, returning almost to the calibrated position after the motion (Fig. 5.17).

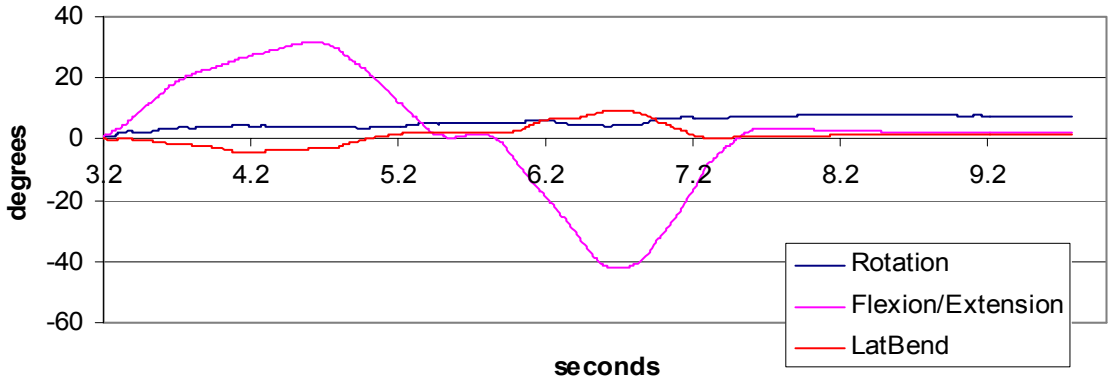

Figure 5.17 Head mounted sensor results for pitch motion less than 90°, rotational matrix output transformed to tilt/twist parameters.

The next test of the sensor involves testing of the roll and yaw motions, using rotational output transformed via the tilt/twist method, up to approximately ±90°, respectively. Both results are acceptable (Fig. 5.18) and show no problems with yaw and roll motions of > ±90° (but less than ±180°).

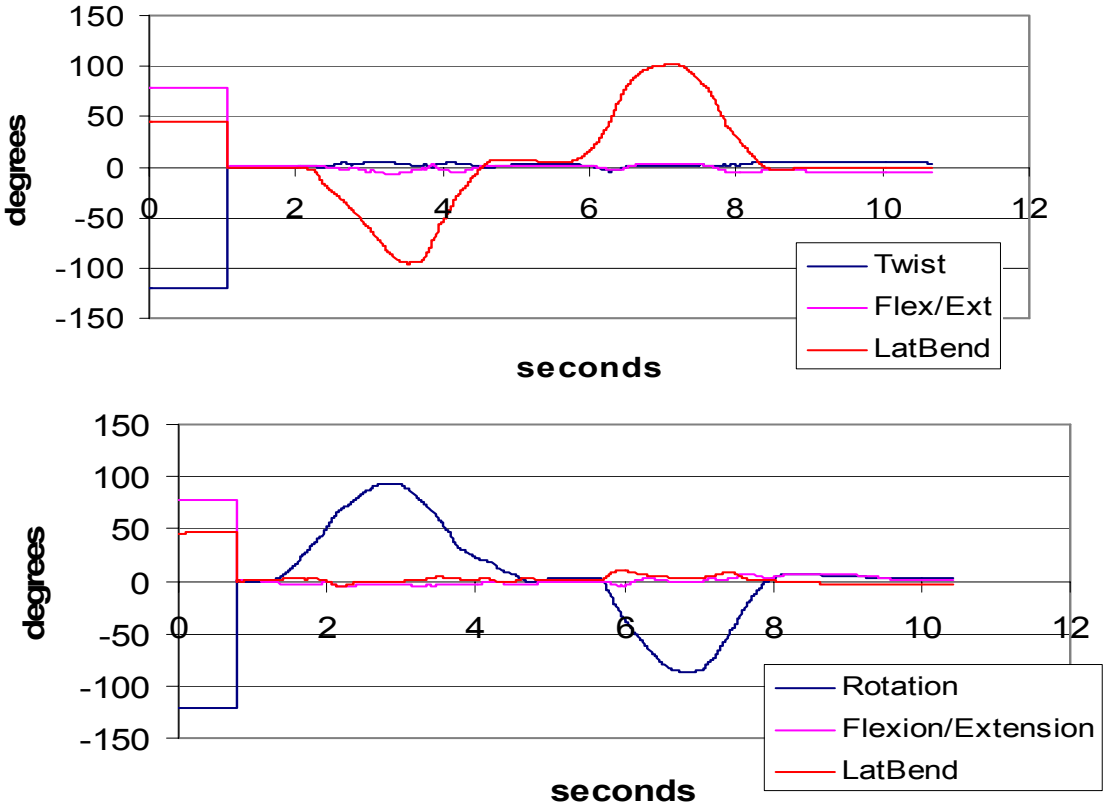

Figure 5.18 Head mounted sensor results for roll motion (top), and yaw motion (bottom) greater than 90°, rotational matrix output transformed to tilt/twist parameters.

The final tests involve pitch motion of > ±90°, and > ±180°. These tests also continue the observation between the pitch value and lateral bending response noted in Fig. 5.17, which was a reasonable response for the motion, but still may be related to the pitch singularity. The pitch test of > ±90° showed the singularity anomaly (Fig. 5.19), with a strong rotation response to pitch motions above 60°, and below - 75° (graphical observation). The lateral bending response to this motion is unique from that already observed for similar pitch motions, decreasing the possibility of error related to the pitch motion.

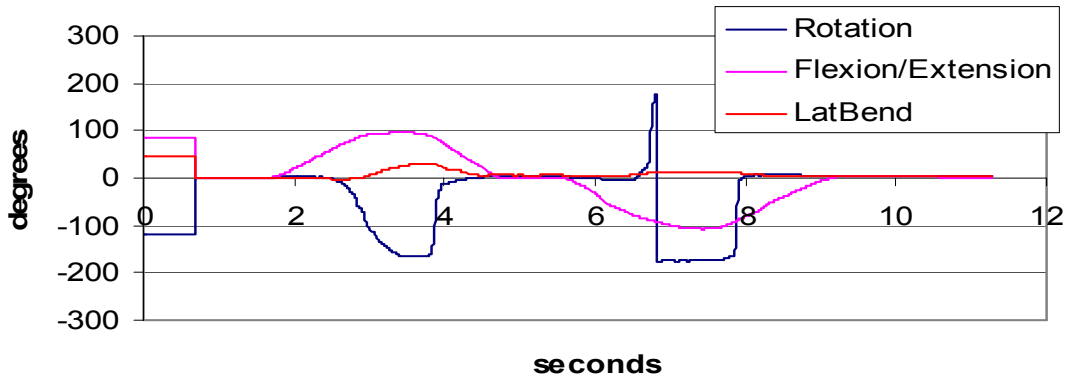

Figure 5.19 Head mounted sensor results for pitch motion greater than 90°, rotational matrix output transformed to tilt/twist parameters.

The pitch test of > ±180° showed (Fig. 5.20) the singularity very clearly, with a strong erroneous rotation response to pitch motions above 89°, and below - 75° (graphical analysis). The lateral bending response to this motion is unique from that already observed, further decreasing the possibility of lateral bending error in response to the pitch motion.

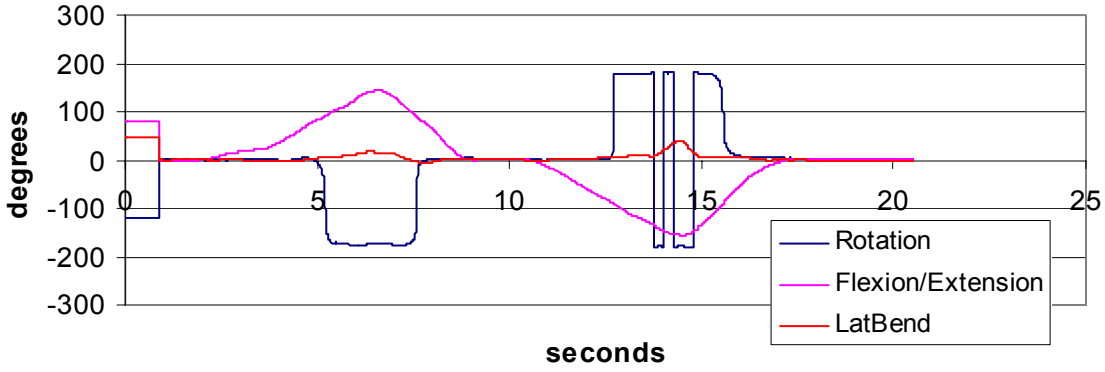

Figure 5.20 Head mounted sensor results for pitch motion greater than 180°, rotational matrix output transformed to tilt/twist parameters.

To summarize the observed singularities to this point, a table has been prepared and presented as follows (Table 5.2). It is worthwhile to mention again that for the sensor rotation matrix output the data must be transformed via a transformation algorithm to tilt/twist parameters of rotation, flexion/extension and lateral bending.

Table 5.2 Singularity results for sensor output

Sensor Output	Motion	Singularity Observed Graphically
Roll, pitch, yaw	Roll > ±110°	None
Roll, pitch, yaw	Yaw > ±110°	None
Roll, pitch, yaw	Pitch > ±110°	Pitch > ±50° effects yaw and roll
Rotation matrix	Flexion/Pitch < ±45°	None
Rotation matrix	Flexion/Pitch > ±110°	Pitch > 60°, < -75° effect rotation*
Rotation matrix	Flexion/Pitch > ±180°	Pitch > 89°, < -75° effect rotation*
Rotation matrix	Rotation/Yaw > ±110°	None
Rotation matrix	Lateral tilt/Roll > ±110°	None

* Note possible effect on lateral bending not consistently observed.

The testing shows that large pitch motions are problematic in both transformed rotation matrix and roll, pitch and yaw output. However, these may not be due to the same singularity. It is still possible the processing of the rotational matrix data is introducing similar singularities as those observed using the roll, pitch and yaw sensor output. To explore this possibility we will next examine the *atan2* function used in the transformation algorithm, as explained below.

The *atan2* function is used in computation to correctly determine the quadrant of a position vector between ±180°. Without use of this function (i.e. use of the *atan* function) we would be restricted to ± 90° motion, as a position vector falling outside this range would give incorrect angular values. Testing a series of points within each quadrant, i.e. (1, 1) (1, -1) (-1, 1) (-1, -1) the *atan2* function outputs the correct angles, i.e. 45°, 135°, -45°, and -135°. We have determined from this that as long as we stay within the atan2 constraint of ±180° we will not have any sign errors.

The next stage in finding our singularity is examining the rotation matrix data, particularly its behavior around the singularity itself (Figs. 5.14, 5.19and 5.20). Recall from Chapter 2 and Appendix A that to express our segment position vector in terms of the global (world) coordinate frame we use the form of the rotation matrix that expresses the object orientation with regards to a fixed global coordinate frame, i.e.

$$\boldsymbol{R}_{SEG} = \begin{bmatrix} a & d & g \\ b & e & h \\ c & f & i \end{bmatrix} = \begin{bmatrix} \hat{x}'_{SEG} \cdot \hat{x}_{G-SEG} & \hat{y}'_{SEG} \cdot \hat{x}_{G-SEG} & \hat{z}'_{SEG} \cdot \hat{x}_{G-SEG} \\ \hat{x}'_{SEG} \cdot \hat{y}_{G-SEG} & y'_{SEG} \cdot \hat{y}_{G-SEG} & \hat{z}'_{SEG} \cdot \hat{y}_{G-SEG} \\ \hat{x}'_{SEG} \cdot \hat{z}_{G-SEG} & \hat{y}'_{SEG} \cdot \hat{z}_{G-SEG} & \hat{z}'_{SEG} \cdot \hat{z}_{G-SEG} \end{bmatrix} \tag{18}$$

To calculate the tilt/twist parameters we use *a, b, c, h,* and *i* to determine the tilt azimuth angle, the tilt angle and the twist angle of the segment position vector, as explained in Chapter 3.

To determine whether the observed pitch singularity is present in the rotational matrix data we observed when the singularity occurred during the most controlled flexion motion trial – the ball task (Fig. 5.21). The rotation matrix parameters were plotted and examined (Fig. 5.22). What was found was a common trend in the rotational matrix values for any frontal pitch or flexion greater than 45°, showing that any overlap of *g*, *a*, and *i*, resulted in incorrect tilt/twist parameters of rotation and possibly flexion. This overlap can be observed in the following graph, representing the head motion rotation matrices for the ball task (Fig. 5.22).

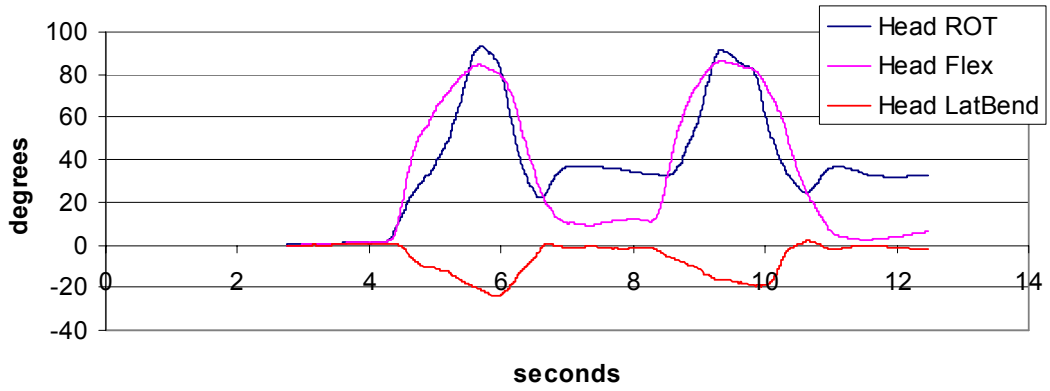

Figure 5.21 Ball task controlled flexion results showing rotation singularity.

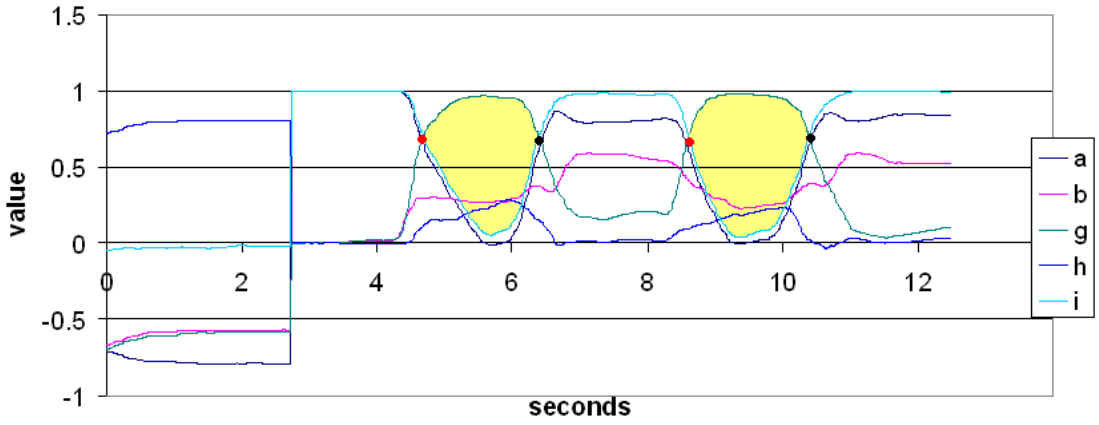

Figure 5.22 Ball task orientation parameters (top) and rotation matrix values (bottom) for head sensor motion showing areas causing singularities in tilt/twist parameters.

The areas between the red and black dots (in Fig. 5.22) exactly correspond to the beginning, duration (yellow or shaded area), and end of the singularities noted in the rotational and (possibly) lateral bending data. This observation holds true for all trials that showed abnormal rotation data for flexion approximately above ± 60°. Knowing that the overlap in these parameters is an indicator of incorrect rotation and possibly lateral bending data, observation of the rotation matrices of the other tasks allowed us to determine accuracy of the orientation data. A correlation between the overlap in the rotation matrices and the flexion data indicates a loss of accuracy of the tilt/twist parameters when flexion approaches or exceeds ± 45°. For those sensors that did not exceed these flexion values the rotation matrices show no overlap, and indicate reasonable results (Fig. 5.23).

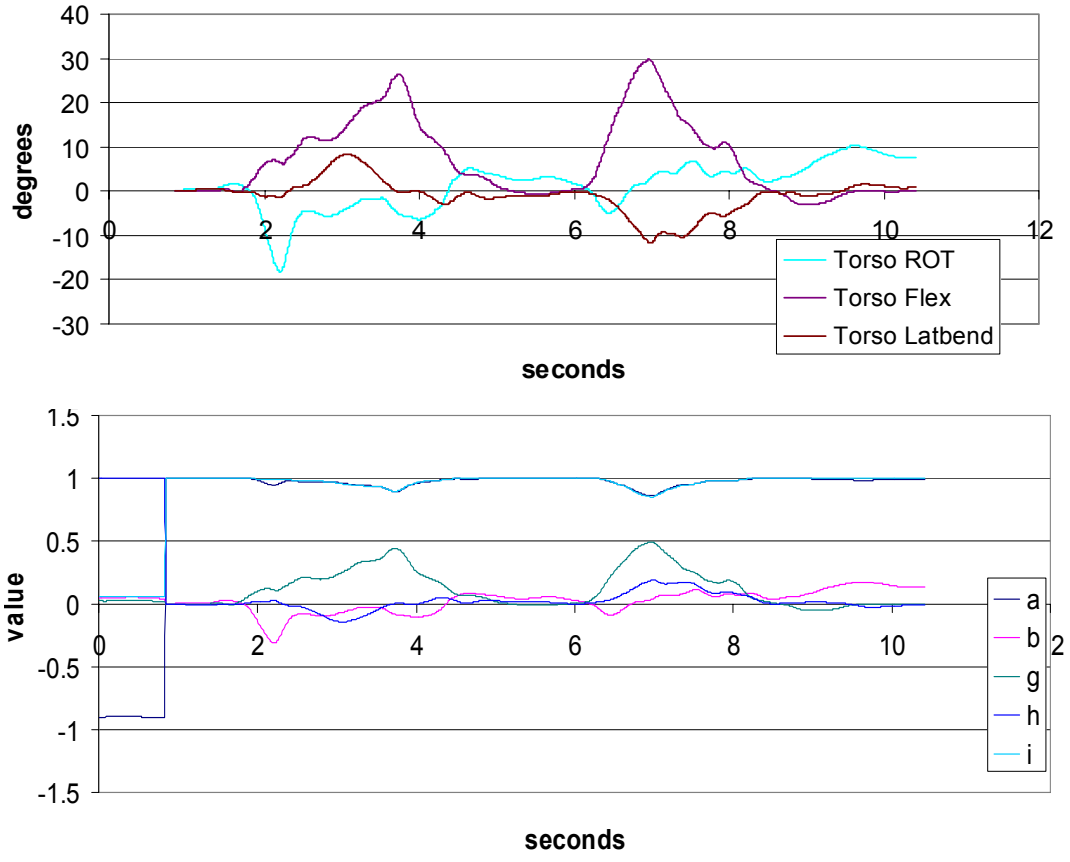

Figure 5.23 Step task orientation parameters (top) and rotation matrix values (bottom) for torso sensor motion.

To determine whether the singularities are a result of the sensor rotation matrices or the tilt/twist transformation process, a series of rotation matrices were collected corresponding to areas bordering and within the singularity zones. When tested for orthogonality the selected rotation matrices did not show any unexpected behaviors, indicating the source of the singularity is within the tilt/twist calculations. Using the rotation matrices to graph the orientation of the position vector, we are able to gain a preliminary visual on the behavior of the singularity. For example, plotting the collected rotation matrices for trial -004 we were able to determine the orientation of the segment at the border and within the singularity simply by reassembling the rotation matrix values as vectors. It is noted that the orientation of the segment at the border of the singularity typically shows flexion of ~ 45°, with a small rotation bringing the orientation vector away from the *X-Z* plane. Orientation of the segment within the singularity shows a high flexion >45° with a significant rotation taking the vector further from the *X-Z* plane.

The collected rotation matrices have a time index that allows us to reference the exact calculated tilt/twist parameters of flexion/extension, lateral bending and rotation. Since we suspect the method of calculating the tilt/twist parameters is introducing the singularity, we can also use the rotation matrices to alternatively calculate flexion/extension, lateral bending and rotation using an alternate theorem, in particular the *Cauchy-Schwartz* theorem, Eq. (19) below, a variation of the dot product calculation used to solve for the angle between two vectors, $\boldsymbol{V}_1$ and $\boldsymbol{V}_2$:

$$\cos\psi = \frac{V_{1x}V_{2x} + V_{1y}V_{2y} + V_{1z}V_{2z}}{\left|\boldsymbol{V}_1\right|\left|\boldsymbol{V}_2\right|} \tag{19}$$

Flexion/extension is motion of the segment along the *X-Z* plane, allowing us to calculate flexion using the *Cauchy-Schwartz* by measuring the angle between the projection of the orientation vector onto the *X-Z* plane and the *z*-axis. The same is done for rotation in the *X-Y* plane, and lateral bending in the *Y-Z* plane. Using the *Cauchy-Schwartz* to determine the flexion, lateral bending and rotation for a matrix (Matrix 8 of the Ball Task Motion at the selected time) collected from within the singularity boundary, we achieve very different results. The tilt/twist transformation for Matrix 8 show flexion of 84.12°,

rotation of 90.3°, and lateral bending of -19.8°. We know the rotation result is an effect of the singularity, as there should be very little rotation for this motion task. The *Cauchy-Schwartz* calculation results show flexion of 86.2°, rotation of 13.2°, and lateral bending of 15.2°, all of which are exactly as expected from the graphical representation of Matrix 8 expressing the orientation of the segment coordinate axes.

Repeating these calculations other motions we see that it is in fact the tilt/twist algorithm that has introduced the singularities into our results. Since we can obtain the flexion/extension, lateral bending and rotation parameters without using the tilt/twist algorithm, the data can be reprocessed. The challenge is to calculate the parameters using a variant of the *Cauchy-Schwartz,* which incorporates the *atan2* function to avoid limiting human motion. To achieve this, the lateral bending and rotation parameters were calculated using the projection of the segment *y*-axis on the *Z-Y* and *X-Y* planes respectively. This avoids any singularities that arise when human motion results in flexion greater than 90°, which results in geometric singularities due to vanishingly small vector components. This can be avoided entirely by using the segment y-axis, though does introduce a singularity at ± 180° (limitation of *atan2*). The flexion is calculated using the *z*-axis of the segment as projected onto the *X-Z* plane, measuring the angle between it and the global *z*-axis. The tilt/twist method is discarded, and data is reprocessed using the new method, designated non-tilt/twist or non-TT.

By removing the tilt/twist transformation method and reprocessing the data for the motion tasks we now obtain results that make intuitive sense (Fig. 5.24), as well as confirm error-checking done by hand.

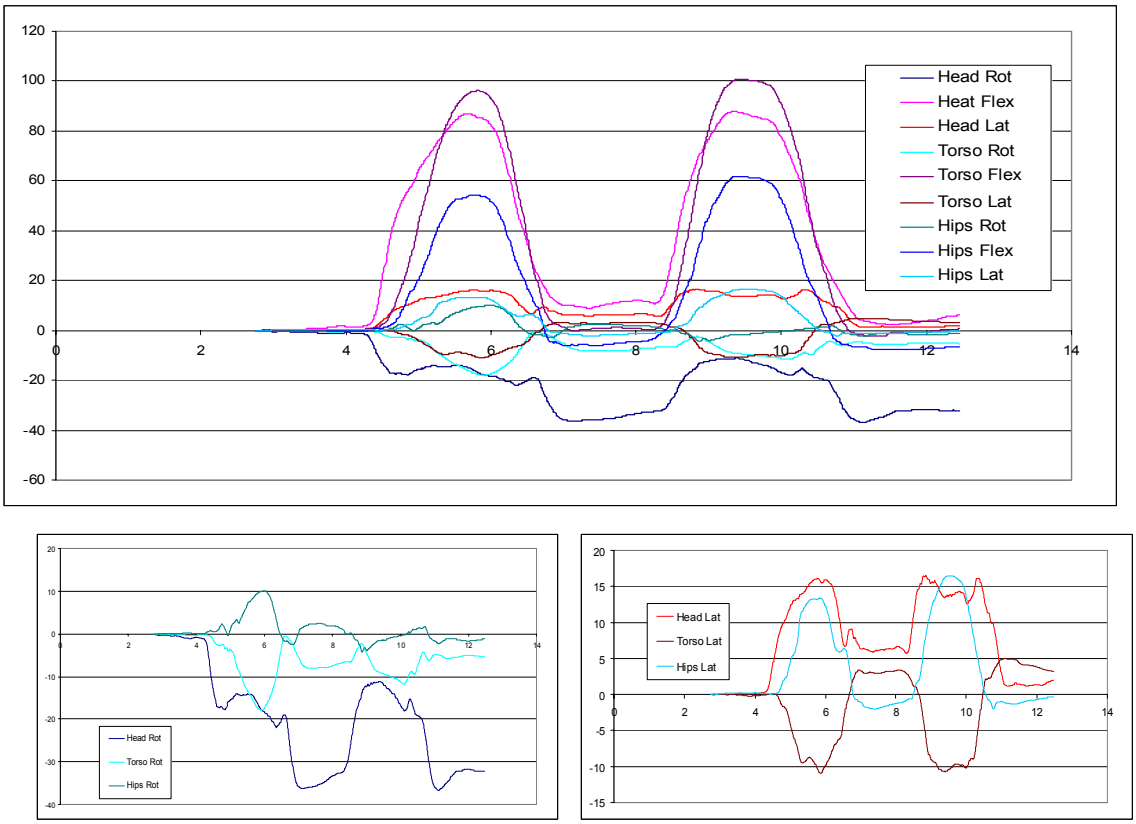

Figure 5.24 Ball task motion results using non-TT method (y-axis in degrees, x-axis in seconds).

For the ball task (Task #2) motion that resulted in such large singularities, the re-processed non-TT data is much more coherent and intuitive. Between the two methods (tilt/twist method and non-TT processing), the flexion values remain very similar. It is with the rotation and lateral bending results that we see the largest variation in the graphs. As seen in Figs. 5.24 and 5.25 the non-TT rotation results are much more coherent and intuitive to the motion than those obtained using the tilt/twist method.

Recall that this task is the ball task, which involves a large flexion component and an expected small rotation and lateral bending. Note that rotation towards the right (turning to the right) is graphed as positive for non-TT data, and negative for TT data.

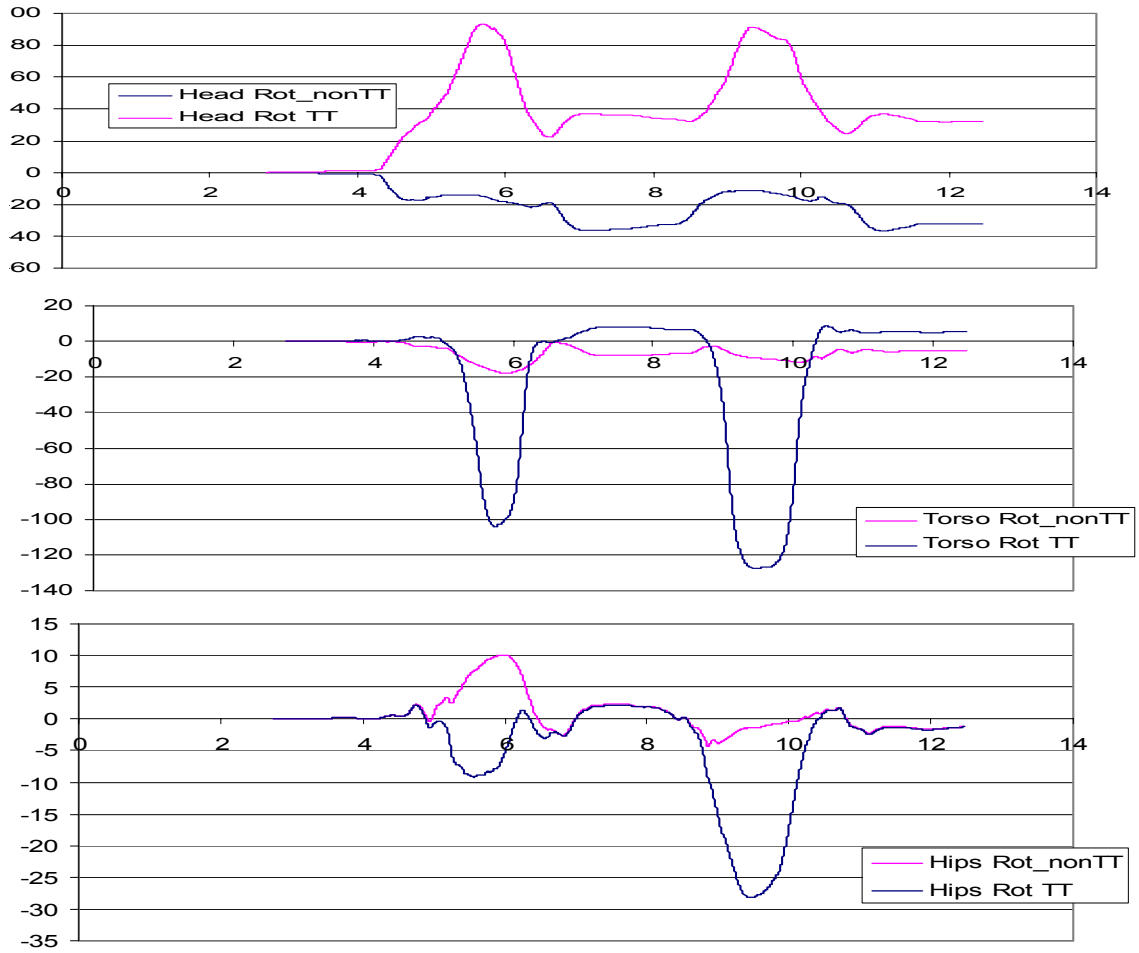

Figure 5.25 Comparison between rotation results obtained with the tilt/twist method (TT) and without (nonTT) for Ball task (y-axis in degrees, x-axis in seconds).

The same non-TT method is applied to the Sitting task, as seen in Fig. 5.26. Note that the graphs represent absolute orientation of the segments in space, and by processing the data further we can also obtain the relative angles between the head and torso and hips, as described in Sec. 3.2.2.

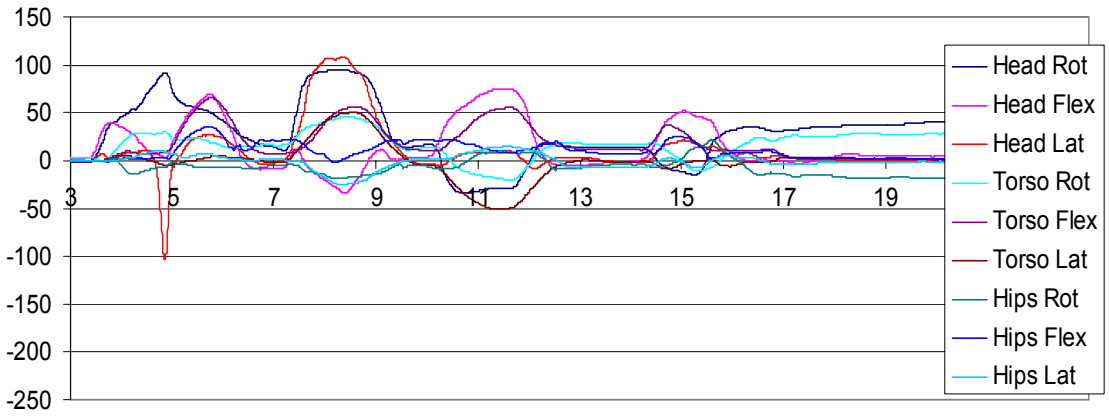

Figure 5.26 Sitting task, trial 000, results (y-axis in degrees, x-axis in seconds).

With corrected the transformation of the sensor data into absolute (or relative) orientation of the segments, we now have a system that is accurate, portable, non-invasive, clinically useful due to small size, and capable of real time measurement. We can now apply the sensors further by monitoring galvanic vestibular stimulation (GVS) response, and develop a user interface that also processes and displays the real-time measurements in real-time.

5.4 GVS Motion Analysis

The UBC Human Neurophysiology Laboratory (HNL) has a DC-based GVS device approved for use by their research team. We have established a collaboration partnership with the HNL allowing us to conduct data collection with our spinal motion measurement sensor system on location at UBC. Collection of data using the DC-based device allows us to direct the development of our own AC-based device which uses smaller driving voltages and therefore is more likely to be approved for use as a clinical device. The subject at UBC is the primary researcher, an expert in GVS. These tests have been approved by the UVic/VIHA Joint Research Ethics Sub-Committee, in an amendment to protocol 2006-36, Appendix H. The sensors are securely placed on the participant, one on the head (on a helmet), one on the torso and one on the hips (both using Velcro bands). The sensors are calibrated to the subject as the participant stands at rest, and records the

motion response (if any) as the subject experiences GVS stimulation protocol. All GVS testing remains within the protocol, as described.

These tests are considered preliminary, and are used only to gain general understanding of the complex human motion responses to GVS stimulation and help verify our inertial sensing system for GVS applications.

The GVS tests involve two modes of bilateral bipolar galvanic stimulation. Bilateral bipolar stimulation requires an anode behind one ear, and a cathode behind the other, both on the mastoid processes or the bony knob felt behind the ear. Tests with the anode behind the right ear are designated ‘Anode Right’ or ‘AR’. Tests with the anode behind the left ear are designated ‘Anode Left’ or ‘AL’. Bilateral bipolar galvanic vestibular stimulation has a suggested response of sway towards the anodal (positive) electrode, which manifests as a lateral bending of the body towards the anodal side.

The purpose of the experimentation is to measure and observe response of the subject to various current levels of no greater than 3.5 milliamps (mA), for a stimulus duration of 2 seconds. Five discrete current levels were set for experimentation, 1 mA, 2 mA, 2.5 mA, 3 mA and 3.5 mA. The goal of the tests is simply to observe the GVS response of the subject at each of the current levels, observing the results for coherent intuitive motion response.

Results for the 1 mA stimulus GVS measurements are shown in Fig.5.27. The results show the expected trend, with positive lateral bending (right bend) towards the anodal electrode, placed behind the right ear. The torso and hips show similar motion patterns to the head, with a decrease in the sway angle, indicating they remain relatively motionless with respect to each other throughout the stimulus response, as would be expected of a standing subject. The response of the hips is opposite to the head and torso, an expected intuitive response for the body to remain balanced while standing with both feet placed on the ground.

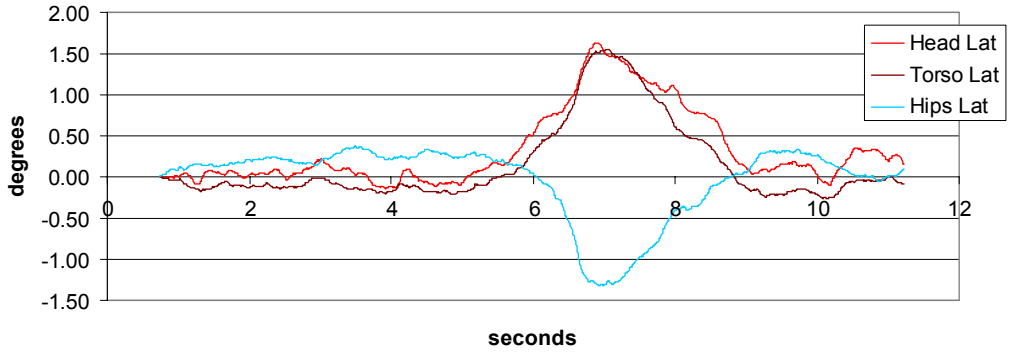

Figure 5.27 AR (anode right) GVS lateral bending response for 1mA stimulus applied for 2 seconds.

The rotational components of the AR GVS 1 mA experiment remain less than ± 1°., as seen in Fig. 5.28. This is as expected for a stimulus typically known to evoke a lateral bending response. What is interesting is the flexion response of the body to the same stimulus. Here it is interesting to note the timing of the stimulus, which is known to last for two seconds, starting at approximately 6 seconds and ending at approximately 8 seconds of measured experiment time. The flexion response in Fig. 5.28 can be seen to begin occurring near the end of the lateral sway response to the stimulus, and is thought to be a compensation motion of the body to the stimulus.

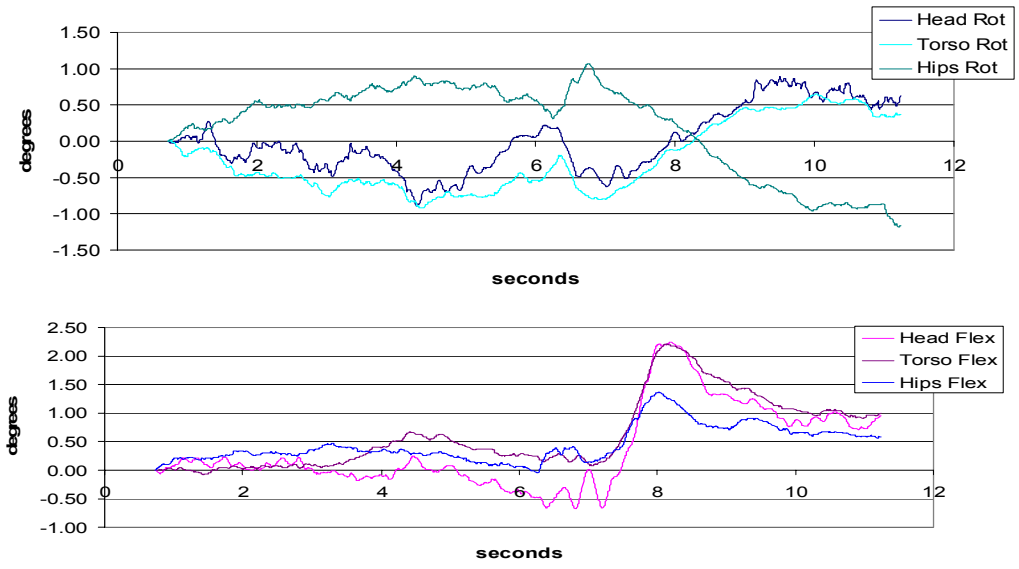

Figure 5.28 AR (anode right) GVS rotation and flexion response for 1mA stimulus applied for 2 seconds.

The same 1 mA stimulus applied for 2 seconds to the left ear (anode left or AL) produces a similar set of graphs (Fig. 5.29). In both the anode right and anode left scenario the flexion response is nearly equal in magnitude to the lateral bending response. From literature, the suggested typical response is primarily a lateral sway, provided the head is facing forward and in parallel with the mid-sagittal plane.

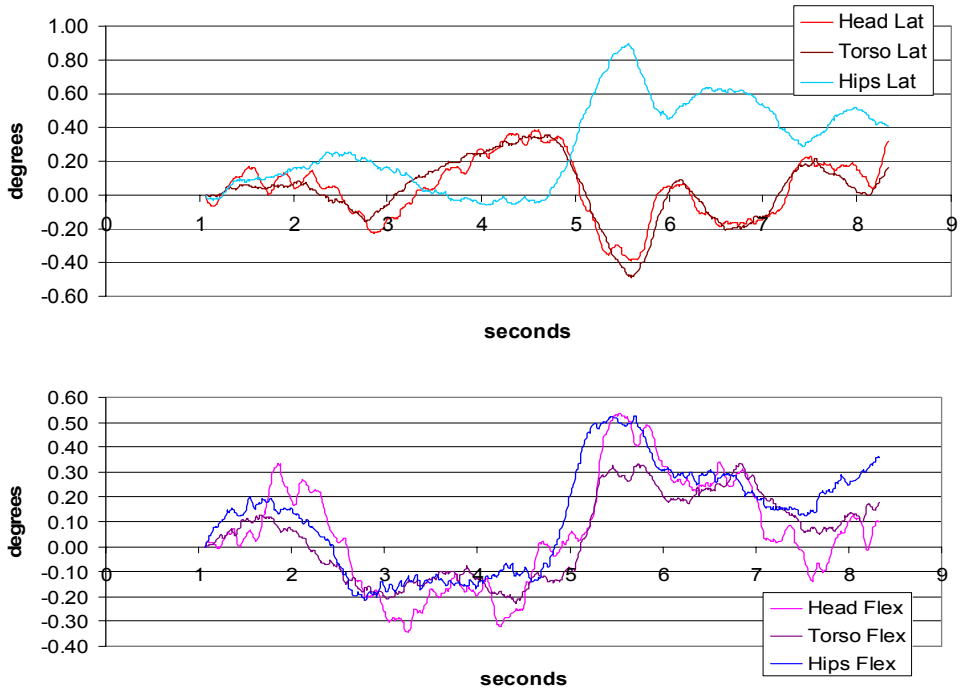

Figure 5.29 AL (anode left) GVS lateral bending and flexion response for 1mA stimulus applied for 2 seconds.

For increasing electrical stimulus the responses measured with the anode behind the right ear are presented in Fig. 5.30, with the anode left results available in Appendix K. Note that the data is not coordinated such that the stimulus start times are coincident. This will be addressed in concluding recommendations for formal GVS testing. We can see from the data (Fig. 5.30) that the largest lateral bending response happens at 2.5 or 3 mA for the head, torso and hips. As expected, the magnitude of the lateral bending sway response decreases in the torso, and further in the hips. The sway response shows an overall increase with increasing stimulus up to 2.5 – 3 mA, but a decrease in response at 3.5 mA.

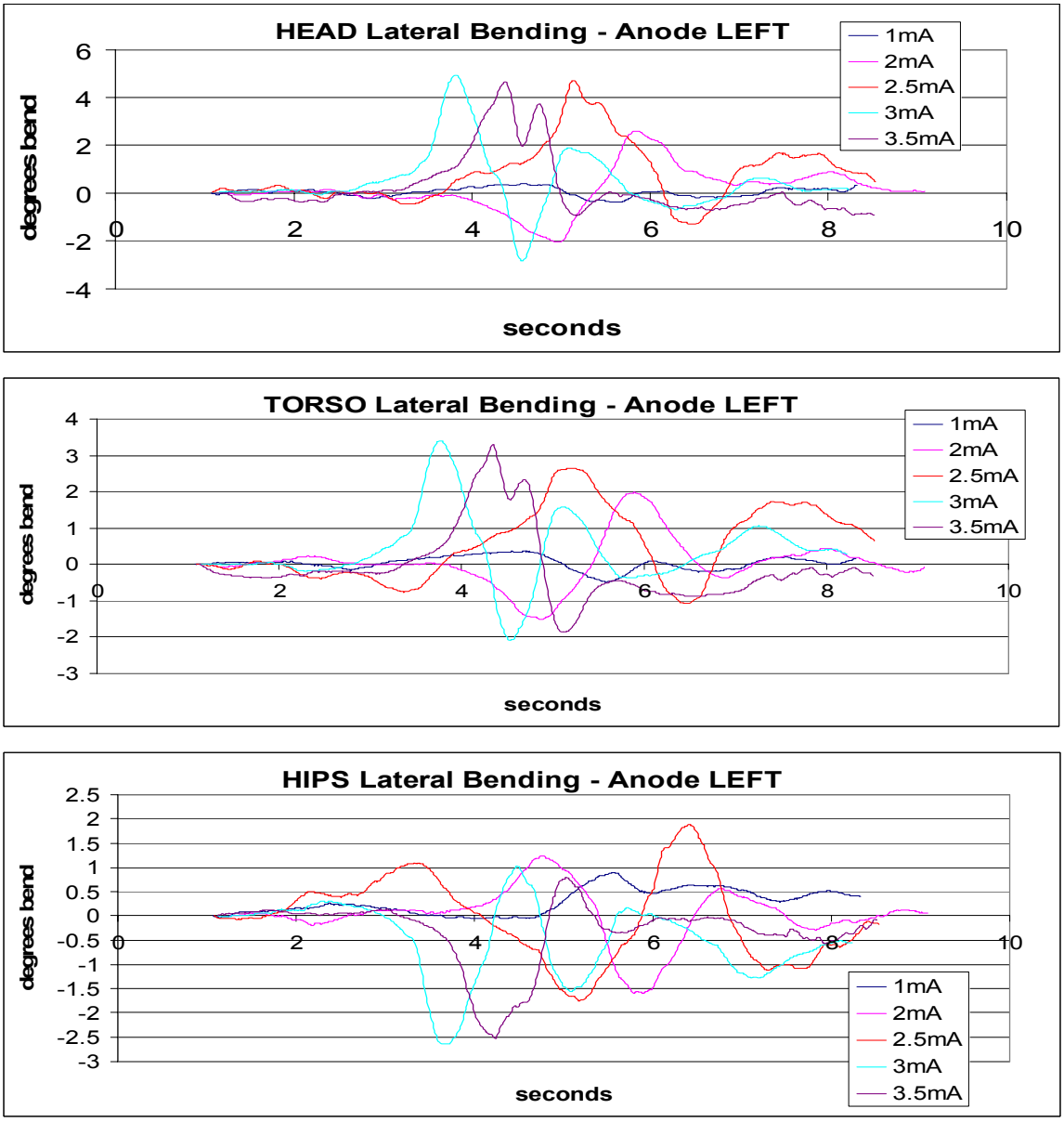

Figure 5.30 Lateral bending response of head, torso and hips to anode right stimulation.

We can see that the flexion (bending forward) data (Fig. 5.31) follows similar characteristic peak response patterns in the head, torso and hips, with the largest response seen in the head measurements, decreasing to the smallest response seen in the hips measurements. The 3 mA stimulus shows the largest flexion sway response for the anode right measurements, and 2.5 mA for the anode left measurements (Appendix K). Overall the flexion sway response increases with increasing stimulus current up to a peak response at 2.5-3 mA, with a decrease in response after peak stimulus. It is as yet

unknown why the flexion response is nearly equal to the lateral bending sway response, as it indicates we have more stimulation occurring other than bilateral bipolar GVS, or that the response to stimulation is much more complicated than literature would suggest.

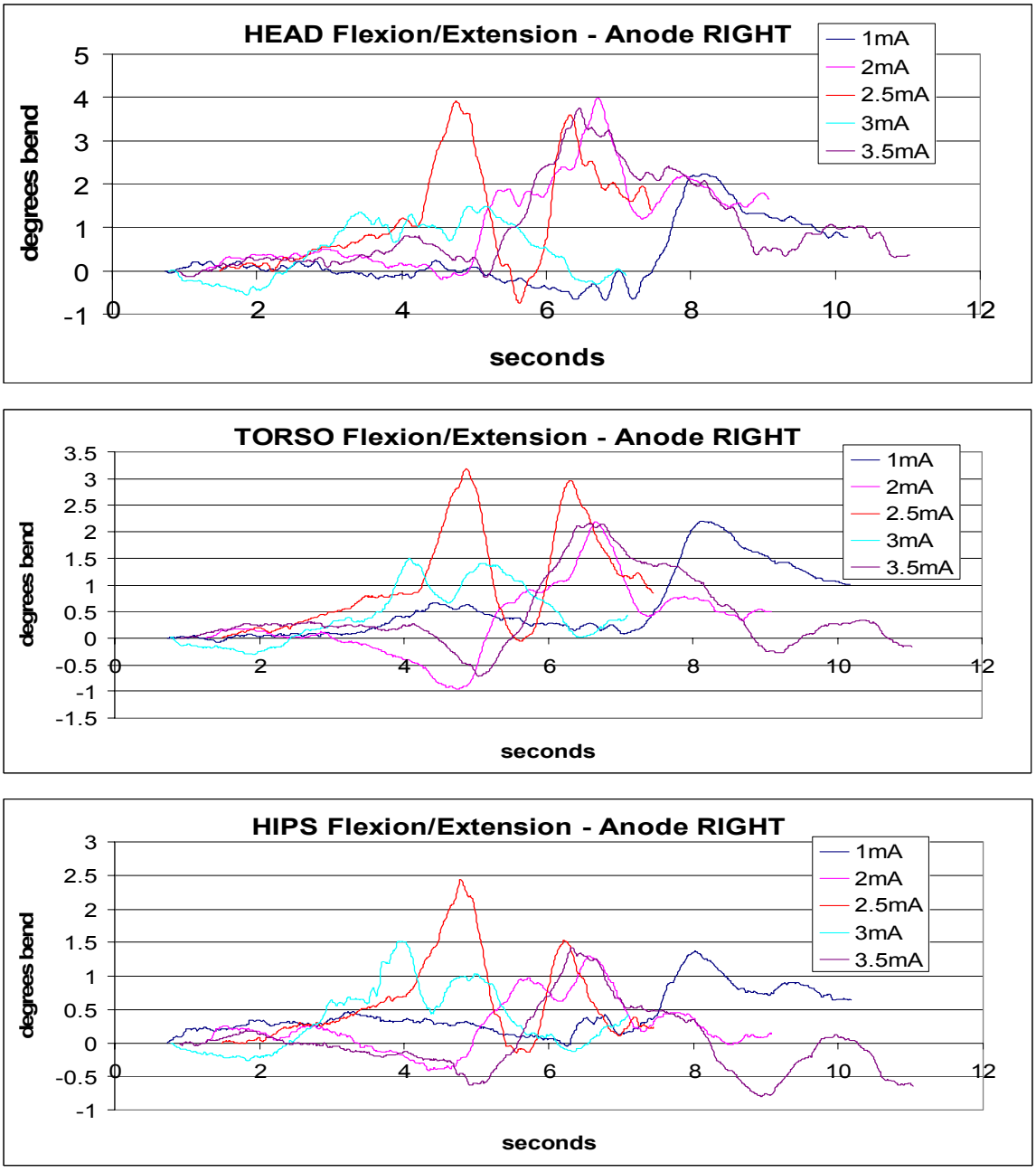

Figure 5.31 Flexion response of head, torso and hips to anode right stimulation.

The 2 mA flexion response is similar in magnitude to the lateral bending sway response, though occurs in a staggered pattern usually a fraction of a second after the lateral

bending sway response. Note that for many of the balance responses the hips counterbalance the upper body during the sway motion, thereby keeping the center of mass over the feet. Full results can be seen in Appendix K.

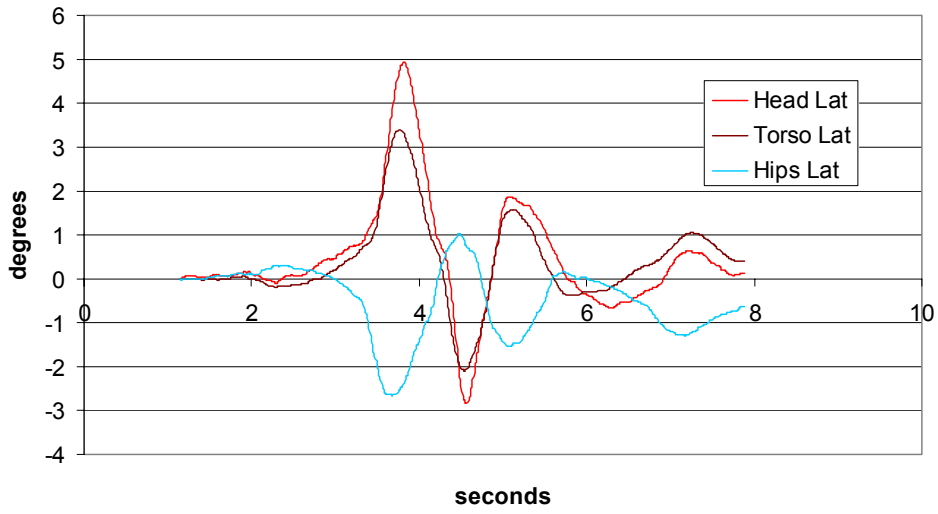

Figure 5.32 Lateral bending sway response of head, torso and hips to anode left 2mA stimulation.

It is of particular interest to note that we would expect the lateral bending response to be positive for anode right stimulation, indicating a lateral sway to the right, and negative for anode left stimulation. This is based on [20, 35], which indicates sway should be towards the anodal (positive) electrode. We do see this result for the 1 mA stimulus, but find a different behavior for the larger stimulus currents. For stimulus currents above and including 2 mA the response shows an opposite behavior, with an initial lateral sway in the cathode direction, followed by a lateral sway in the anode direction. This response behavior is suggested in [9], who also notes that GVS stimulation has no rotational equivalent that the body could experience, indicating the response should be towards the cathodal electrode (negative). Typical results for the larger stimulation currents can be seen in Fig. 5.32. Literature [9, 35] suggests lateral sway responses to average stimulation currents of 1.5 mA or less. However, because we are using stimulation current considered to be higher than typically used, it is possible that the whole body response to the

stimulation has become more complex than the responses typically noted for stimulation currents less than 1.5 mA.

Chapter 6

Conclusions

This chapter summarizes the achievements to date, including their impact on the research questions raised in Chapter 2. Any open issues still remaining are discussed and directions for recommended further work are mentioned with an estimate of relevance, importance and amount of work needed. Here we determine whether we achieved the goals/objectives of the thesis.

6.1 Sensor Verification

The sensors have an onboard magnetic compensation function, which combined with advance onboard Kalman filtering, allows the sensors the capability of compensating for yaw drift. However, this magnetic compensation ability is limited as explained by the manufacturer, and it was our task to determine whether this made the sensors unsuitable for use. Results show that without magnetic compensation the sensors exhibit large yaw drift, the parameter most sensitive to drift as it is the only one unable to be corrected by the accelerometers acting as inclinometers. Magnetic compensation tests ran continuously over a period of 3 hours, though without a consistent timing schedule (i.e. a test every 15 minutes). Despite this, an increase in drift was noted for magnetically compensated measurements. However, this drift was removed when the sensors were recalibrated (turned off for a few seconds, then turned back on and calibrated to the fixture). It is determined that for tests within a few minutes, as was the duration of all of our tests, the

magnetic compensation is sufficiently accurate. This level of accuracy was tested further in the VICON verification tests.

The sensor output of roll, pitch and yaw (Euler output) is automatically derived from the rotation matrix expressing the change in orientation of the sensor from its calibrated global position representing the global or world axes. Using a VICON 460 optical motion measurement capture system, a gold standard in motion capture technology, we compared the Euler parameters obtained from the sensor with the Euler parameters calculated from the VICON optical markers. Euler output was selected for the verification tests to keep calculations simple and minimize processing, staying as close to the raw data as possible and eliminating unnecessary steps that could introduce error. The VICON markers, attached to the sensors to represent the *z*- and *x*-axes of the calibrated sensor's coordinate system, allowed comparison of the sensor's position in space between sensor measurements and VICON.

The results show small consistent offset values, a result of misalignment of the VICON global axes and the sensor's calibrated global axes. With this offset removed, and discounting the inherent singularities of Euler parameters, the average magnetically compensated roll and pitch offset was less than 1 degree, and the average yaw offset less than 1.8 degrees. Recall that yaw is the parameter most often beset by drift errors. Note that verification tests involved only one sensor at a time, in a limited range of motion no greater than 45 degrees (natural motion of one segment with all others held rigid) of roll, pitch or yaw to avoid occlusion problems with the VICON system. In VICON verification testing the sensors were found to accurately represent the roll, pitch and yaw motion of the segment to which they were attached.

The rotational matrix output of the sensors, from which the Euler orientation parameters are derived, is a singularity free representation of the sensor orientation with respect to the calibrated global axes. The rotation matrix was translated via a developed transformation algorithm into the tilt/twist parameters of flexion/extension, rotation and lateral bending. After receiving ethics approval, subjects were recruited and asked to

perform balance tasks representing common motions experienced in everyday life, such as bending to pick up and object, sitting and standing, and stepping up onto a stable platform. Results showed that forward tilt (pitch/flexion) motions greater than 45° caused inexplicable errors in rotational data. Investigation of the pitch motion using the Euler parameters showed that a pitch outside of ±45° resulted in incorrect roll and yaw data. Because the VICON tests did not involve motions outside of this range (only one segment/sensor pair was in motion for each test while the rest remained stationary) our verification results are unaffected, as noted in data comparison.

Examination of the rotational matrix output for a forward flexion motion of ~90° showed the pitch/flexion anomaly clearly, furthering the conclusion that such a motion results in incorrect rotation and lateral bending. With the cause of the anomaly still unknown, but assuming the rotation matrix output from the sensor was singularity free (as claimed), the next step was to examine the transformation algorithm that converts the rotation matrix to tilt/twist parameters. The *atan2* function was tested as a possible source of error introduced by the evaluating software, but was found to be correct in application.

Next, to determine whether the observed pitch/flexion singularity is present in the rotational matrix data we observed when the singularity occurred during the most controlled flexion motion trial – the ball task. What was found was a common trend in the rotational matrix values for any frontal pitch or flexion greater than 45°, showing that any overlap of the plotted rotation matrix output parameters (Eq. 18) of g, a, and i, resulted in incorrect tilt/twist parameters of rotation and possibly flexion and lateral bending. Further investigation ensued. To gain an understanding of the orientation vector and observe possible trends leading to the singularity, matrices were collected for the boundary points of the singularities (Fig. 5.22), as well as a matrix from within the singularity. When graphed by hand the orientation vector of the boundary matrices described a vector with a flexion of ~ 45°, with a small rotation bringing the vector away from the X-Z plane.

Orientation of the described vector within the singularity shows a high flexion >45° with a significant rotation taking the vector far from the *X-Z* plane. From observation the singularity occurs when the flexion reaches 45° combined with a significant rotation component that rotates the vector out of the *X-Z* plane. The orientation of the vector when graphed by hand showed a reasonable segment position, unlike the position indicated using the tilt/twist algorithm. All motions that exhibited the observed pitch/flexion singularity were examined by plotting their rotation matrix parameters to search for the rotation matrix overlap. The result was that all motions showing singularities satisfied the overlap observation, with the overlap boundaries corresponding to flexion of ± 45°. This correlation between the overlap in the rotation matrices and the flexion data indicates a loss of accuracy of the tilt/twist parameters when flexion approaches or exceeds ± 45°. This pointed to the tilt/twist algorithm as the source of error, implemented from a published technique known as the 'Tilt Twist Method' [28].

To pinpoint the cause of the tilt/twist error, we examined other motions and their resulting rotation matrices. The collected rotation matrices have a time index that allows us to reference the exact calculated tilt/twist parameters of flexion/extension, lateral bending and rotation. Since we suspect the tilt/twist method is introducing the singularities, we can also take the rotation matrices and calculate flexion/extension, lateral bending and rotation using and alternate theorem, in particular the *Cauchy-Schwartz* theorem (Eq. 19), a variation of the dot product calculation used to solve for the angle between two vectors: $\boldsymbol{V}_1$, $\boldsymbol{V}_2$. For our axes designation as *Z* upwards, *X* forwards, and *Y* left, flexion/extension is motion in the *X-Z* plane, with rotation in the *X-Y* plane and lateral bending in the *Z-Y* plane. The tilt/twist calculation results for flexion/extension, rotation and lateral bending are significantly different for those calculated using the *Cauchy-Schwartz,* at the boundaries and within the plotted rotation matrix overlap zones. The result is that the tilt/twist method results in erroneous data wherever the rotation matrix values of *g*, *a*, and *i* overlap in the described manner, a tilt motion of ~ 45° or greater.

To correctly transform the sensor rotation matrices into the orientation parameters of flexion/extension, lateral bending and rotation, a modified version of the *Cauchy-Schwartz* was developed by the author and implemented. This modified version utilizes the *atan2* function, to give us a range of ±180° in each plane, a range more than adequate to capture natural human motion. It has been observed that calculating the rotation of the segment/sensor using the *z*-axis or *x*-axis projection of the orientation vector on the *X-Y* global plane introduces singularities into the measurements when flexion approaches 90°. Similar singularities occur when lateral bending is calculated using the *z*-axis projection on the *X-Z* global plane. Because human motion is primarily that of flexion/extension and rotation, minimal singularities occur when the lateral bending and rotation measurements are calculated using the projection of the segment's *y*-axis on the *Z-Y* and *X-Y* global planes respectively. The flexion measurement is calculated with the segment's *z*-axis projection in the *X-Z* global plane. The resulting data is both intuitively correct and agrees with *Cauchy-Schwartz* error checking calculations.

Using the modified *Cauchy-Schwartz* theorem in transforming the sensor rotation matrix into the clinically intuitive parameters of flexion/extension, rotation and lateral bending of the spine results in absolute (or relative) orientation of the head, torso and hips. Relative measurements can also be calculated for the spinal segments. The sensors are also capable of wireless communication through Bluetooth technology, allowing a greater range of use as the current wires limit the system to be within 5 meters of the operating PC. The result is a spinal motion measurement system that is accurate, portable, non-invasive, clinically useful due to small size and intuitive output parameters, and capable of real time measurement or natural human motion. We have developed a spinal motion measurement technique capable of capturing real-time motion of a subject's body segments within a 180° range of flexion/extension, lateral bending and rotational motion.

6.2 GVS Results

The UBC Human Neurophysiology Laboratory (HNL) has a galvanic vestibular DC-based stimulation (GVS) device approved for use by their research team, with which we

recorded subject response with our sensors to bilateral bipolar GVS. The GVS tests were performed to gain an understanding of expert subject response to bilateral bipolar GVS, with which we could direct the design of our own AC-based GVS stimulation device (see future work). The subject at UBC is an expert in GVS. Five discrete stimulating current levels were used in experimentation; 1 mA, 2 mA, 2.5 mA, 3 mA and 3.5 mA. The GVS tests involved two modes of bilateral bipolar galvanic stimulation, with an anode behind one ear, and a cathode behind the other. Tests with the anode behind the right ear are designated 'Anode Right' or 'AR'. Tests with the anode behind the left ear are designated 'Anode Left' or 'AL'. Bilateral bipolar GVS has a suggested response of sway towards the anodal (positive) electrode in some literature [20, 35] and a suggested sway towards the cathodal (negative) electrode in other literature [9]. Human response to GVS is highly complicated and dependant on the individual, with no two responses the same between subjects. The purpose of this testing is to gain a general preliminary understanding of GVS response.

Results for the 1 mA stimulus GVS measurements are as expected, showing positive lateral bending (right bend) towards the anodal electrode, placed behind the right ear. The response of the hips is opposite to the head and torso, an expected intuitive response of the body to remain balanced while standing with both feet placed on the ground. Rotational response was minimal, as expected. An unexpected result, seen in all stimulation currents, was the flexion response of the body in nearly equal magnitude to the peak lateral sway. It was observed that the flexion response lagged behind the lateral sway response, indicating a possible compensation response. For the stimulation currents above 1 mA, an anomaly was noted in the measured response of the subject. As with the 1 mA response, it would be expected that the subject would experience lateral sway towards the anode. What is seen for all stimulating currents above 1mA was an initial sway response towards the cathode, followed by a smaller magnitude sway towards the anode, continuing in a sinusoidal oscillation. Within the stimulation range the magnitude of the sway response peaked at 2.5-3 mA. The hip sway also counterbalanced in an opposite sinusoidal oscillation.

The GVS results to stimulation via the UBC Human Neurophysiology Laboratory (HNL) DC-based GVS device were very encouraging. The graphs were easily understood to represent intuitive human motion. The lateral sway oscillating response for stimulation currents above 1 mA was unexpected, as was the large flexion component response. Literature [9, 35] suggests lateral sway responses to average stimulation currents of 1.5 mA or less. However, because we are using stimulation current considered to be higher than typically used, it is possible that the whole body response to the stimulation has become more complex than the responses typically noted for stimulation currents less than 1.5 mA. However, this was simply a first step into understanding the human body's complex balance response, and the results were extremely encouraging. Additional steps could incorporate markers for stimulus start and end points, to maximize data usability.

We have developed a graphical user interface (GUI) in MATLAB that visually illustrates real time motion of the subject in flexion/extension, lateral bending and rotation. A playback window/option replays the same data using both an animated vector representation of the spine. This GUI is at the development stage, and has yet to be verified.

The result is incorporation of the spinal motion measurement technique with a GVSD device, capable of recording coherent and accurate motion of the body in response to electrical stimulation.

6.3 Future Work

Because the magnetic compensation abilities of the sensors have yet to be defined as to their exact loss of accuracy over time, tests need to be devised to determine long term accuracy. Running the sensors for several hours, testing a prescribed yaw motion every 10–15 minutes, would be an excellent test. A variation with which to compare would be to run the same test and to recalibrate every 10-15 minutes before the yaw motion was performed. Using smaller time intervals may also be useful. These tests may be valuable to define exact 'in field' levels of accuracy. The sensors have been verified using

VICON, an optical motion measurement system. It may be of use to verify them using a popular electromagnetic tracking system. This may provide a basis towards the development of a motion sensor that combines the two technologies to make a more robust system.

To continue towards our ultimate research goal of incorporating the spinal motion measurement technique with GVS as a balance prosthetic or diagnostic device, we need to develop our own stimulation unit device safe for use in a clinical setting. This device has been developed by the research team, for research applications. The resulting AC-based GVSD, developed in parallel to the spinal motion measurement system by research colleagues, is capable of providing output signals of zero volts/zero current, a constant current set point, or a waveform that ranges between zero volts (zero current) and a maximum programmed current value within our current range, maximum most positive current is 5 mA.. The possible waveforms can be sine, square, triangle, or stochastic, programmed to have a frequency of up to 300 Hertz (Hz). The electrodes and conducting gel chosen have been recommended by experts in the stimulation field.

The next step is to determine whether this device is capable of the desired stimulation parameters, or if it is capable of a new stimulation pattern previously unachieved in research applications. Characterization of the device is required to determine whether it is stimulating correctly, particularly as compared to the stimulation device used at the UBC HNL. A question to be asked is whether we can characterize human response to either device, looking for trends that can provide additional design objectives.

The next step with the spinal motion measurement system is to develop an intuitive and accurate GUI that incorporates the real-time balance response of the subject via graphical data in response to GVSD stimulation. Both the spinal motion measurement system and the GVSD will be controlled, measured and monitored via the GUI, which will need to be tested itself for accuracy. The GUI will also need to be redeveloped using an institutionally appropriate programming environment, other than MATLAB. Eventually, both the spinal motion measurement system and the GVSD will both be completely

wireless and portable, capable as acting as a balance feedback device, possibly with the addition of force plates for additional data on the subject's center of mass. The spinal motion measurements system will monitor the balance of the subject, whose balance response to GVS has been characterized. When the subject's stability is endangered the device will compensate by stimulating the appropriate sequence to recover balance.

References

[1] National Institute of Health, *National Strategic Research Plan: Language and Language Impairments, Balance and Balance Disorders, Voice and Voice Disorders*.

[2] Hendrick Balance Center, available online: <http://www.hendrickhealth.org/balance.disorders.htm>, cited November 12, 003.

[3] Vestibular Disorders Association, "Vestibular Disorders: An Overview", available online: <http://www.vestibular.org/overview.html>, cited November 12, 2003.

[4] Merfeld, D.M. and Rabbitt, R.D., "Vestibular Prosthetics", *Neuroprosthetics*, K. Horch *et al.* (ed.), World Scientific Pub. Co., 2003 (in press).

[5] Goodvin, C. and Park, E.J., "Implantable Prosthesis for the Inner Ear", *Proceedings of CDEN Design Conference*, Montreal, QC, July 29-30, 2004

[6] Wall III C, Weinberg M (2003). Balance prostheses for postural control. IEEE Engineering in Medicine and Biology Magazine pp.84-90.

[7] Liu J, Shkel AM, Nie K, Zeng FG (2003). System design and experimental evaluation of a MEMS-based semicircular canal prosthesis. Proceedings of IEEE EMBS Conference on Neural Engineering; Capri Island, Italy, March 20-22: 177-180.

[8] Desmond A (2004). Vestibular function: evaluation and treatment. Thieme Medical Publishers Inc., New York.

[9] Fitzpatrick R, Day B (2004). Probing the human vestibular system with galvanic stimulation. Journal of Applied Physiology 96:2301-2316.

[10] Bonato P (2005). Advances in wearable technology and applications in physical medicine and rehabilitation. Journal of Neuroengineeing and Rehabilitation 2:2.

[11] Balan A, Sigal L, Black M (2005). A quantitative evaluation of video-based 3D person tracking. In: Proceedings of IEEE Int Workshop on Visual Surveillance and Performance Evaluation of Tracking and Surveillance, Beijing, China, 349-356.

[12] Zheng Y, Nixon MS, Allen R (2003). Lumbar spin visualization based on kinematic analysis from videofluoroscopic imaging. Medical Engineering & Physics 171-179.

[13] Klein P, Broers C, Feipel V, Salvia P, Van Geyt B, Dugailly PM, Rooze M (2003). Global 3D head-trunk kinematics during cervical spine manipulation at different levels. Clinical Biomech 18:827-831.

[14] Jordan K (2000) Assessment of published reliability studies for cervical spine range of motion measurement tools. Journal of Manipulative and Physiological Therapies 23:3

[15] Cipriano J. Photographic Manual of Regional Orthopedic and Neurological Tests 2nd Ed pp. 49-54.

[16] Magee D (1987). Orthopedic Physical Assessment. pg 178.

[17] Gibbs P, Asada H (2005). Wearable conductive fiber sensors for multi-axis human joint angle measurements. Journal of NeuroEngineeing and Rehabilitation 2:7.

[18] Gajdosik RL, Bohannon RW (1987). Clinical measurement of range of motion: review of goniometry emphasizing reliability and validity. Physical Therapy 67:1867-72.

[19] Taylor M, Hipp J, Gertzbein S, Gopinath S, Reitman C (2006). Observer agreement in assessing flexion-extension X-rays of he cervical spine, with and without the use of quantitative measurements of intervertebral motion. The Spine Journal. Article in press.

[20] Desmond A (2005). Common misconceptions about ENG. Vestibular Disorders Association, short publication.

[21] Bussman J, Martens W, Tulen J, Schasfoort F, Van Den Berg-Emons H, Stam H (2001). Measuring daily behavior using ambulatory accelerometry: The Activity Monitor. Behavior Research Methods, Instruments & Computers 33(3):349-356.

[22] Luinge H, Veltink P (2005). *Measuring orientation of human body segments using miniature gyroscopes and accelerometers.* Medical & Biological Engineering & Computing., 43:273-282.

[23] Mayagoitia R, Nene A, Veltink P (2002). Accelerometer and rate gyroscope measurement of kinematics: an inexpensive alternative to optical motion analysis systems. Journal of Biomechanics 35:537-542.

[24] Barshan B, Durrant-Whyte H (1995). Inertial navigation systems for mobile robots. IEEE Transactions on Robotics and Automation 11:328-342.

[25] C.V.C. Bouten, K.T.M. Koekkoek, M. Verduin, L. Kodde, J.D. Janssen (1997). A triaxial accelerometer and portable data processing unit for the assessment of daily physical activity. IEEE Trans. Biomed. Eng., 44: 136-147.

[26] Foerster F, Smeja M, Fahrenberg J (1999). Detection of posture and motion by Accelerometry: a validation study in ambulatory monitoring. Comput Human Behav., 15:571-583.

[27] Zhou H. Hu H. Tao Y (2006). Inertial measurement of upper limb motion. Med Bio Eng Comput 44:479-487.

[28] Lee R, Laprade J, Fung E (2003). A real-time gyroscope system for three-dimensional measurement of lumbar spin motion. Medical Engineering & Physics 25:817-824.

[29] Zhou H, Hu H, Harris N. Hammerton J (2006). Applications of wearable inertial sensors in estimation of upper limb movements. Biomedical Signal Processing and Control 1:1 pp22-32.

[30] Williamson R, Andrews B (2001). Detecting absolute human knee angle and angular velocity using accelerometers and rate gyroscopes. Medical & Biological Engineering & Computing 39:294-302.

[31] Boonstra M, Slikke M, Keijsers N, van Lummel R, de Waal Malefijt, Verdonschot N (2006). The accuracy of measuring the kinematics of rising from a chair with accelerometers and gyroscopes. Journal of Biomechanics 39:2 pp 354-358.

[32] Roetenberg D, Luinge HJ, Baten CTM, Veltink PH (2005). Compensation of magnetic disturbances improves inertial and magnetic sensing of human body segments orientation. IEEE Transactions on Neural Systems and Rehabilitation Engineering 13:395-405.

[33] Yim-Chiplis P, Talbot L (2000). Defining and measuring balance in adults. Biological research for nursing 1:4:321-331.

[34] Berg KO, Maki BE, Williams JI, Holliday PJ, Wood-Dauphinee SL (1992). Clinical and laboratory measures of postural balance in an elderly population. Arch Phys Med Rehabil 73: 1073-80.

[35] Pavlik AE, Inglis JT, Lauk M, Oddsson L (1999). The effects of stochastic galvanic vestibular stimulation on human postural sway. Exp Brain Res 124:273-280.

[36] R.E. Mayagoitia, J.C. Lötters, P.H. Veltink, H. Hermens, Standing balance evaluation using a triaxial accelerometer, Gait and Posture, vol. 16, pp. 55-59, 2002.

[37] Wardman D, Day B, Fitzpatrick R (2003). Position and velocity responses to galvanic vestibular stimulation with human subjects during standing. Journal Physiology 547:293-299.

[38] Baselli G, Legnani G, Franco P, Brognoli F, Marras A, Quaranta F, Zappa B (2001). Assessment of inertial and gravitational inputs to the vestibular system. Journal of Biomechanics 34:821-826

[39] Blanks R, Curthoys I, Markham C (1975). Planar relationships of the semi-circular canals in man. Acta Otolaryngol 80:185-196.

[40] Bent L, Bradford JM, Merkley VF, Kennedy PM, Inglis JT (2000). Magnitude effects of galvanic vestibular stimulation on the trajectory of human gait. Neuroscience letters 279:157-160.

Appendix A: Rotation Matrix Theory

Describing an orientation by three unit vectors denoting the principle axes of a body attached coordinate system, and stacking the three unit vectors as the columns of a 3x3 matrix, results in a rotation matrix describing the vectors of the body frame relative to the desired frame of reference, the global frame. All the columns of the rotation matrix have unit magnitude, and are orthogonal.

$$ {}^{G}_{B}\boldsymbol{R} = \begin{bmatrix} {}^{G}\hat{\boldsymbol{X}}_{B} & {}^{G}\hat{\boldsymbol{Y}}_{B} & {}^{G}\hat{\boldsymbol{Z}}_{B} \end{bmatrix} = \begin{bmatrix} {}^{B}\hat{\boldsymbol{X}}_{G}^{T} \\ {}^{B}\hat{\boldsymbol{Y}}_{G}^{T} \\ {}^{B}\hat{\boldsymbol{Z}}_{G}^{T} \end{bmatrix} \tag{A.1} $$

The columns of the rotation matrix are the unit vectors of the body frame{B} written in the global frame {G} and the rows are the unit vectors of {G} written in {B}. The rotation matrix output of the MT9 sensor is in the following format for each sensor, with *t* as the time code:

$$ \boldsymbol{R} = [t, a, b, c, d, e, f, g, h, i] \tag{A.2} $$

To describe orientation of the sensor in the global frame we assemble the matrix as follows:

$$ \boldsymbol{R} = \begin{bmatrix} a & d & g \\ b & e & h \\ c & f & i \end{bmatrix} \tag{A.3} $$

Note that the transpose of this matrix expresses the global frame in the sensor or body frame. This definition allows us to define the unit vectors of the body frame as expressed in the global frame as:

$$ {}^{G}\hat{\boldsymbol{X}}_{\boldsymbol{B}} = \begin{bmatrix} a \\ b \\ c \end{bmatrix}, \; {}^{G}\hat{\boldsymbol{Y}}_{\boldsymbol{B}} = \begin{bmatrix} d \\ e \\ f \end{bmatrix}, {}^{G}\hat{\boldsymbol{Z}}_{\boldsymbol{B}} = \begin{bmatrix} g \\ h \\ i \end{bmatrix} \tag{A.4} $$

We also know the unit vectors of the global frame as expressed in the body frame:

$$ {}^{B}\hat{\boldsymbol{X}}_{\boldsymbol{G}} = \begin{bmatrix} a \\ d \\ g \end{bmatrix}, \; {}^{B}\hat{\boldsymbol{Y}}_{\boldsymbol{G}} = \begin{bmatrix} b \\ e \\ h \end{bmatrix}, \; {}^{B}\hat{\boldsymbol{Z}}_{\boldsymbol{G}} = \begin{bmatrix} c \\ f \\ i \end{bmatrix} \tag{A.5} $$

We have defined the body axes as our orientation vectors. The initial positions of the respective body segment axes are set during calibration of the sensors such that the initial position vectors define the global coordinate frame. The subsequent orientation of the body axes as they go through motion is continually expressed in the rotation matrix output by the sensors, allowing us to continually calculate the new orientation of the body segment in the global frame. The components of a vector are simply the projections of the vector onto the unit directions of its coordinate system axis:

$$ \begin{aligned} {}^{G}\hat{Z}_{x} &= {}^{B}\hat{X}_{G} \cdot \hat{Z}_{B} \\ {}^{G}\hat{Z}_{y} &= {}^{B}\hat{Y}_{G} \cdot \hat{Z}_{B} \\ {}^{G}\hat{Z}_{z} &= {}^{B}\hat{Z}_{G} \cdot \hat{Z}_{B} \end{aligned} \tag{A.6} $$

With equivalent expressions holding true for the *x*- and *y*-axes. Therefore we can express the rotation matrix completely as follows:

$$ {}^{G}_{B}R = \begin{bmatrix} {}^{G}\hat{X}_{B} & {}^{G}\hat{Y}_{B} & {}^{G}\hat{Z}_{B} \end{bmatrix} = \begin{bmatrix} {}^{B}\hat{X}_{G}^{T} \\ {}^{B}\hat{Y}_{G}^{T} \\ {}^{B}\hat{Z}_{G}^{T} \end{bmatrix} = \begin{bmatrix} a & d & g \\ b & e & h \\ c & f & i \end{bmatrix} = \begin{bmatrix} \hat{x}_{B} \cdot \hat{x}_{G} & \hat{y}_{B} \cdot \hat{x}_{G} & \hat{z}_{B} \cdot \hat{x}_{G} \\ \hat{x}_{B} \cdot \hat{y}_{G} & \hat{y}_{B} \cdot \hat{y}_{G} & \hat{z}_{B} \cdot \hat{y}_{G} \\ \hat{x}_{B} \cdot \hat{z}_{G} & \hat{y}_{B} \cdot \hat{z}_{G} & \hat{z}_{B} \cdot \hat{z}_{G} \end{bmatrix} \quad \text{(A.7)} $$

Appendix B: VICON Coordinate Transformation

With the marker positions known and measured relative to the VICON global coordinate reference axes, the position vectors constructed from the marker data can be calculated and used to obtain the roll, pitch and yaw of the sensor/body segment motion. It is important to align the sensor axes to the VICON coordinate reference axes during sensor calibration, as this will result in the most coherent data. Any misalignment between the global coordinate frame of the sensor and that of the initial VICON global ready can be compensated for, simply by calculating the difference in orientation and factoring it into the calculations.

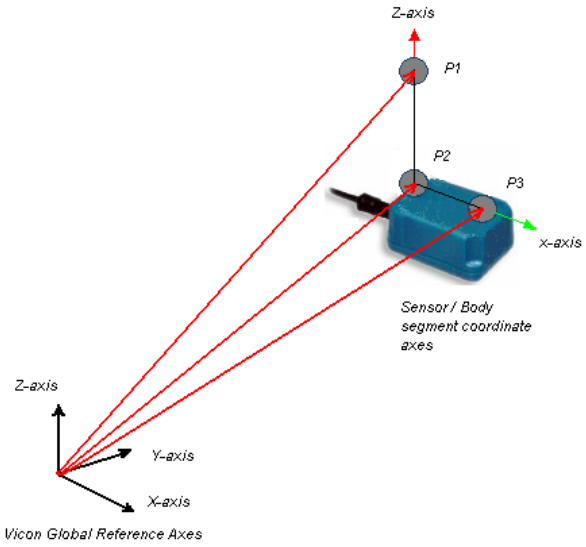

Figure B.1 VICON global axis and relation to markers places on sensor

The VICON output of the marker orientation is in the following VICON format:

$$t \quad T10x \quad T10y \quad T10z \quad C7x \quad C7y \quad C7z \quad STRNx \quad STRNy \quad STRNz \tag{B.1}$$

Where *t* is the time index, *T10* designates the P2 marker, *C7* the P1 marker and *STRN* the P3 marker. The components of each marker position are subscripted with *x, y or z*. We can now assemble the vectors representing the *z*- and *x*- axes, with which we can then calculate roll, pitch and yaw of the body as seen by the VICON system. The *z*- axis can be found by subtracting the *T10* (P2) components from the *C7* (P1) components, and the *x*-axis can be found by subtracting the *STRN* (P3) components from the *T10* (P2) components:

$$\begin{aligned} Z'_{SEG-x} &= T10x - C7x \\ Z'_{SEG-y} &= T10y - C7y \\ Z'_{SEG-z} &= T10z - C7z \end{aligned} \quad , \quad \begin{aligned} X'_{SEG-x} &= T10x - STRNx \\ X'_{SEG-y} &= T10y - STRNy \\ X'_{SEG-z} &= T10z - STRNz \end{aligned} \tag{B.2}$$

With these two relations known we can now calculate the roll, pitch and yaw of the axes, with respect to the calibrated global, as they change orientation. Note that the sensors have an opposite sign convention for pitch, so the below calculations have been adjusted accordingly.

$$\text{Pitch angle} = atan2\left(\frac{-X'_{SEG-z}}{X'_{SEG-x}}\right) \tag{B.2}$$

$$\text{Roll angle} = atan2\left(\frac{Z'_{SEG-y}}{Z'_{SEG-Z}}\right) \tag{B.3}$$

$$\text{Yaw angle} = atan2\left(\frac{X'_{SEG-y}}{X'_{SEG-x}}\right) \tag{B.4}$$

Appendix C: Tilt Twist Method

The objective of the tilt twist method is to represent 3D joint angles in a physically meaningful (clinical) and mathematically stable way based on a cylindrical model of joints. The method provides stable angles through both small and large movements that are physically meaningful in the same way as Euler/Cardan angles and projection angles [28].

Each joint is represented using a double overlapping cylinder (one joint = two cylinders) model where the top cylinder represents the upper moving vertebra and the lower is the fixed vertebra. The most interesting and meaningful motion of a joint is the angular motion. Our goal is to express mathematically stable planar rotation angles about the *x*-, *y*- and *z*-axis in terms of flexion/extension, lateral bending and twist (rotation). The flexion/extension and lateral bending parameters are derived from the tilt angle. This technique can also model the knee and other joints, expressing the planar rotations of the joints in terms of flexion/extension, ab/adduction, and endo/exorotation. The following equations are exactly as presented in the Tilt Twist Method.

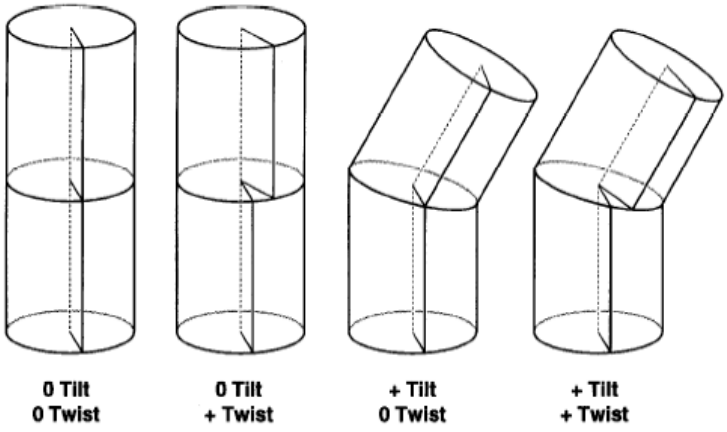

Figure C.1 Visualization of tilt twist.

Joint reorientation is described by three angles calculated from the known coordinate axis aligned initial and final orientation vectors: the tilt angle, the tilt azimuth angles and the twist angle. The method is intended for use with directly measured spinal joint angles.

The initial and final orientation vectors can be described in terms of their directional unit vectors, ***i, j, k, i', j'*** and ***k'***. It is from these directional unit vectors that we will calculate the tilt angle (ϕ), tilt azimuth angle (θ) and the twist angle (τ). The *z* direction is the vertical direction (opposite gravity) with the *x* direction representing the forward frontal direction, and the *y* direction as designated by the right handed coordinate system convention. The orientation vector of the cylinder/joint is designated the vertical axis or z-axis and extends from the top surface of the cylinder.

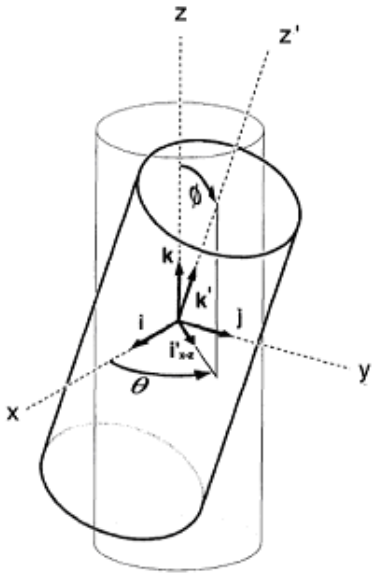

Figure C.2 Visualization of azimuth and tilt angles.

C.1 Tilt

We will assume the initial or 'natural' position of the cylinder to be level. From this position the cylinder can 'tilt' downwards, a range of 0 to ~90 degrees (°) and is always a positive value. Tilt, (ϕ), can be calculated from the following relation [28]:

$$\cos \phi = \boldsymbol{k} \cdot \boldsymbol{k}' \tag{C.1}$$

Where $\boldsymbol{k}$ and $\boldsymbol{k}'$ are the initial and final orientations of the z-axis aligned with the center top cylinder surface. Because of this alignment we can reduce the relation to:

$$\cos \phi = \boldsymbol{k}'_{\mathrm{y}} \tag{C.2}$$

The tilt can also be obtained using the projection of the z'-axis on the x-y plane, requiring the use of the *atan2* computer function to accommodate sign variations. This form is useful for comparison with the tilt azimuth angle computation as seen below.

$$\phi = atan2(\boldsymbol{k}'_y \sin\theta + \boldsymbol{k}'_x \cos\theta, \boldsymbol{k}'_z) \tag{C.3}$$

The bending direction of the tilt is determined by the tilt azimuth angle, θ. The azimuth angle is measured with respect to the positive y-axis (left), with a counterclockwise (left turn) positive range to 180 degrees and a negative clockwise (right turn) range to -180 degrees. Since we have aligned **i**, **j** and **k** with the coordinate axis our tilt azimuth formula is:

$$\tan\theta = \frac{\boldsymbol{k}'_y}{\boldsymbol{k}'_x} \tag{C.4}$$

To account for the range of negative values possible in evaluation, the computer function *atan2* is used:

$$\theta = atan2(\boldsymbol{k}'_y, \boldsymbol{k}'_x) \tag{C.5}$$

Once values have been obtained for the tilt and tilt azimuth angles we can express them in terms of the clinically meaningful parameters flexion/extension and lateral bending. The flexion/extension angle, F, can be written as:

$$F = \phi\cos\theta \tag{C.6}$$

where flexion is positive and extension is negative and lateral bending angle , L, can be written as:

$$L = \phi \sin\theta \tag{C.7}$$

where right lateral bending is positive. Both F and L are zero when there is no tilt as the projection vector $\boldsymbol{k}'_{x\text{-}y}$ is undefined, therefore tilt azimuth can arbitrarily be set to zero when this condition is encountered.

C.2 Twist

The twist angle (τ) combined with the tilt and tilt azimuth angle provide a complete description of the angular motion of the joint. The twist angle, $\boldsymbol{\tau}$, represents the rotation (yaw) about the z-axis of the cylinder from its initial position. Bending or tilt of the upper portion of the cylinder with respect to the bottom portion changes the normal vector on the plane between the two overlapping cylinders. This normal vector, $\boldsymbol{k}_{1/2}$, is directed at one-half the upper cylinder's tilt angle and has a tilt azimuth equal to the upper cylinder's, and can be expressed as [28]:

$$\boldsymbol{k}_{1/2} = \begin{matrix} \sin\frac{\phi}{2}\sin\theta \\ \cos\frac{\phi}{2} \\ \sin\frac{\phi}{2}\cos\theta \end{matrix} \tag{C.8}$$

Arbitrarily positioned hatch marks on the upper and lower cylinder surfaces indicate the alignment between cylinders. Twist motion of the upper cylinder will result in a new hatch projection whose angle with the reference hatch mark (no twist) is the twist angle τ. A mathematical description of the twist angle can be determined by assigning a zero degree hatch mark $\boldsymbol{h}_0$ at the intersection of the cylinder and the *x-z* plane, which represents the medial or midsagittal plane:

$$\boldsymbol{h}_o = j \times k_{1/2} \tag{C.9}$$

As rotation occurs the orientation of the hatch mark changes and can be calculated from the new orientation of the cylinder axes:

$$\boldsymbol{h'} = j' \times k_{1/2} \tag{C.10}$$

The projection of $\boldsymbol{h}$' onto the lower surface of the bottom cylinder is designated $\boldsymbol{h}'_{\mathrm{p}}$. With no twist $\boldsymbol{h}'_{\mathrm{p}}$ is coincident with $\boldsymbol{i}$. With twist the separation between $\boldsymbol{h}'_{\mathrm{p}}$ and $\boldsymbol{i}$ is the twist angle $\boldsymbol{\tau}$, expressed mathematically as:

$$\tan\tau = \left(\frac{h'_{p,y}}{h'_{p,x}}\right) = \left(\frac{h'_{y}}{h'_{x}}\right) \tag{C.11}$$

This can be solved [28] to give:

$$\tau = a\tan 2\left(i'_Z \sin\theta - j'_Z \cos\theta, i'_Z \cos\theta + j'_Z \sin\theta\right) \tag{C.12}$$

The range of twist is -180 to 180 degrees, with positive values in the counterclockwise direction from the midsagittal line (x-axis) and negative values clockwise. As the tilt angle approaches 90 degrees the location of the hatch mark degenerates and small variations in tilt produce large variations in twist [28]. This angle is difficult to reach for most joints, though caution must be exercised when using the cylinder technique to generalize several joints, as in our application.

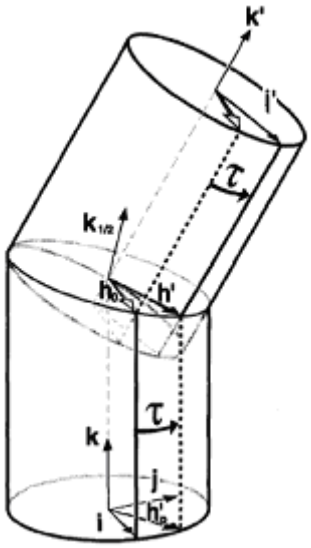

Figure C.3 Visualization of twist angle.

Appendix D: Task 1 Results for Spinal Motion Analysis Using Tilt/Twist Method

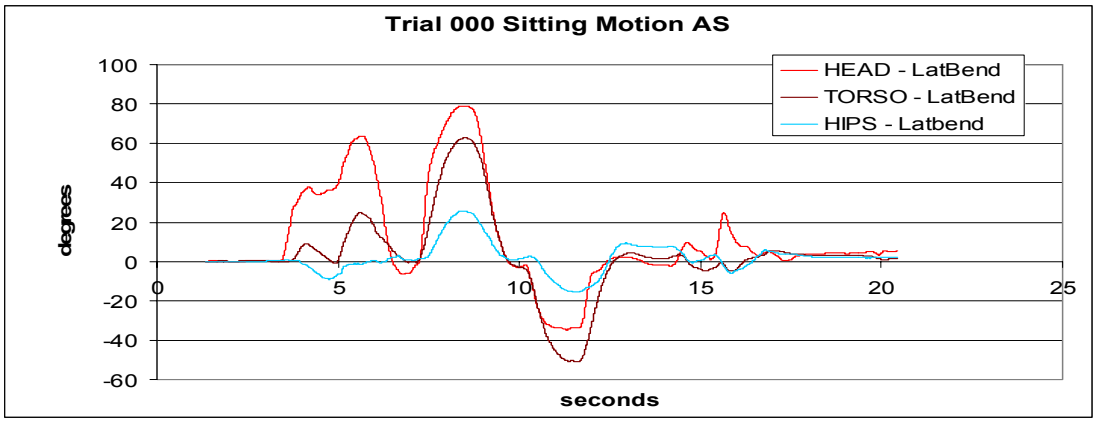
Trial 000 Sitting Motion AS
HEAD - LatBend
TORSO - LatBend
HIPS - Latbend
degrees
seconds
100
80
60
40
20
0
-20
-40
-60
0
5
10
15
20
25

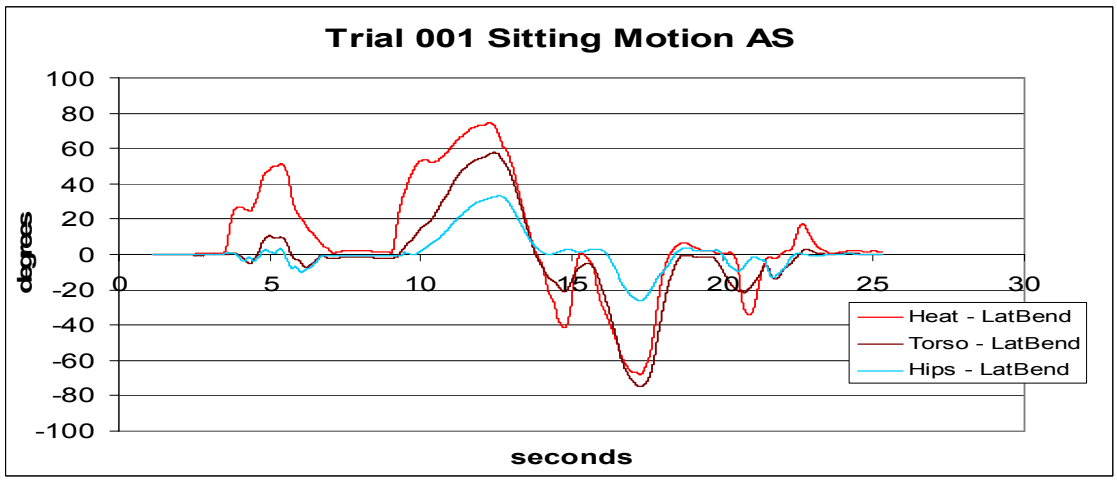
Trial 001 Sitting Motion AS
Heat - LatBend
Torso - LatBend
Hips - LatBend
degrees
seconds
100
80
60
40
20
0
-20
-40
-60
-80
-100
0
5
10
15
20
25
30

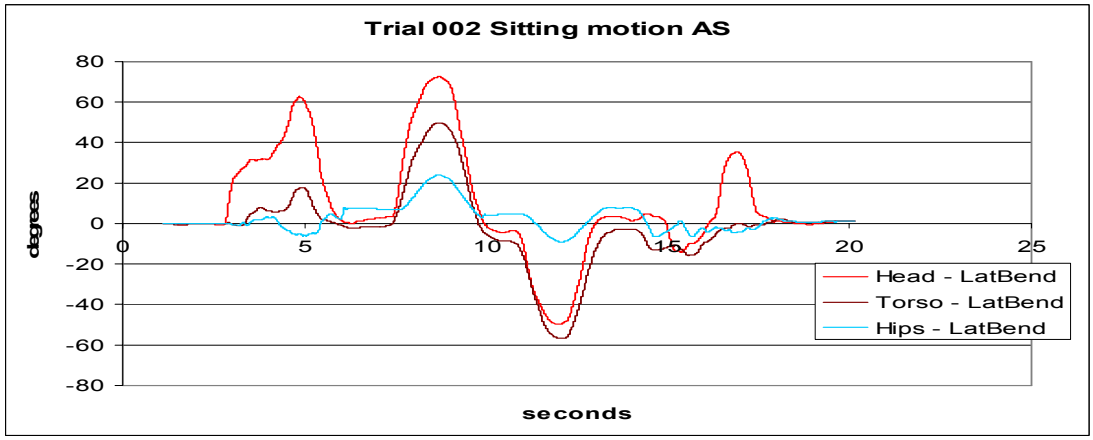
Trial 002 Sitting motion AS
Head - LatBend
Torso - LatBend
Hips - LatBend
degrees
seconds
80
60
40
20
0
-20
-40
-60
-80
0
5
10
15
20
25

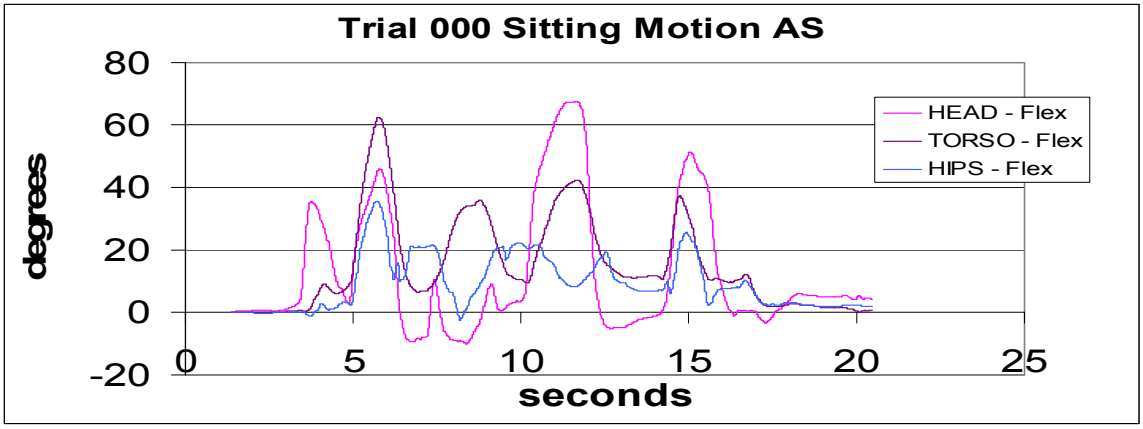
Trial 000 Sitting Motion AS
80
60
40
20
0
-20
degrees
0
5
10
15
20
25
seconds
HEAD - Flex
TORSO - Flex
HIPS - Flex

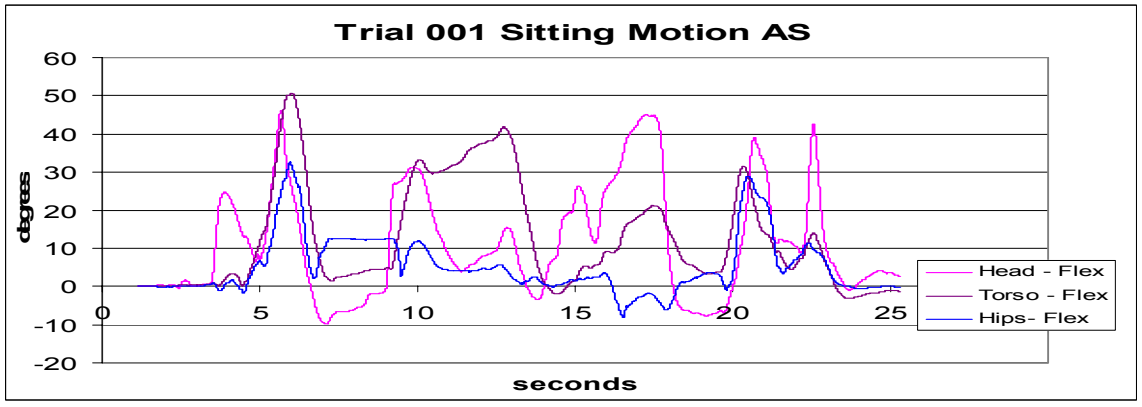
Trial 001 Sitting Motion AS
60
50
40
30
20
10
0
-10
-20
degrees
0
5
10
15
20
25
seconds
Head - Flex
Torso - Flex
Hips- Flex

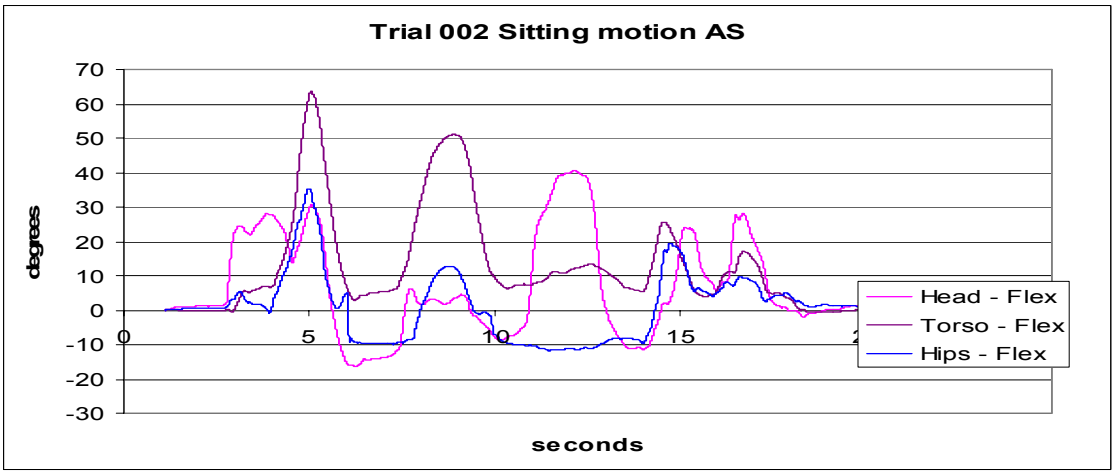
Trial 002 Sitting motion AS
70
60
50
40
30
20
10
0
-10
-20
-30
degrees
0
5
10
15
seconds
Head - Flex
Torso - Flex
Hips - Flex

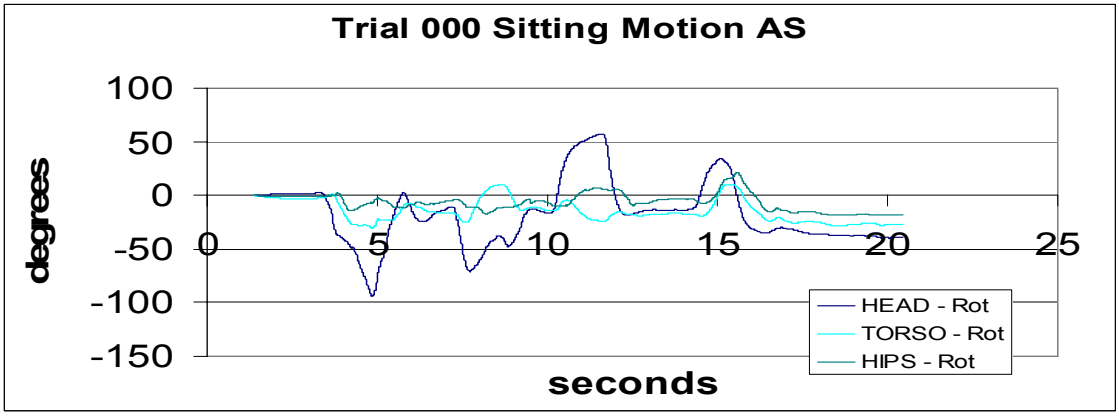
Trial 000 Sitting Motion AS
100
50
0
-50
-100
-150
degrees
0
5
10
15
20
25
seconds
HEAD - Rot
TORSO - Rot
HIPS - Rot

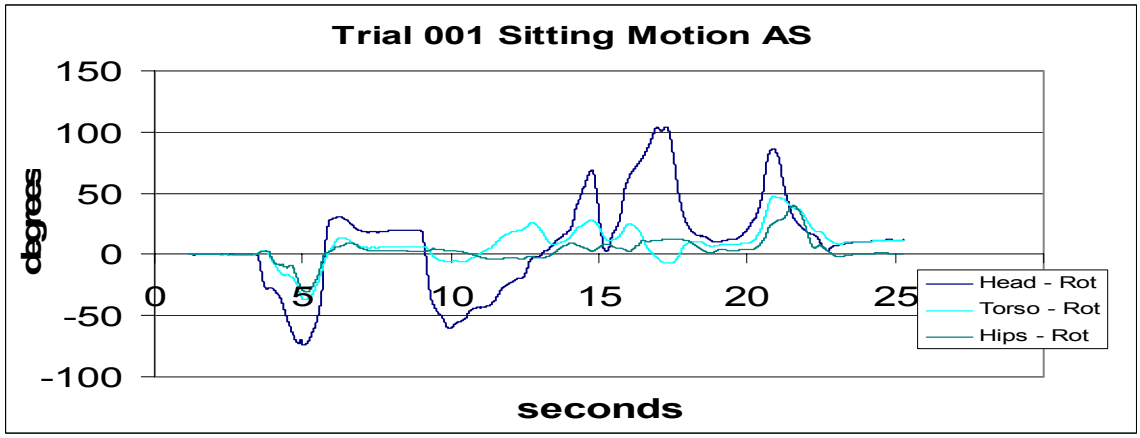
Trial 001 Sitting Motion AS
150
100
50
0
-50
-100
degrees
0
5
10
15
20
25
seconds
Head - Rot
Torso - Rot
Hips - Rot

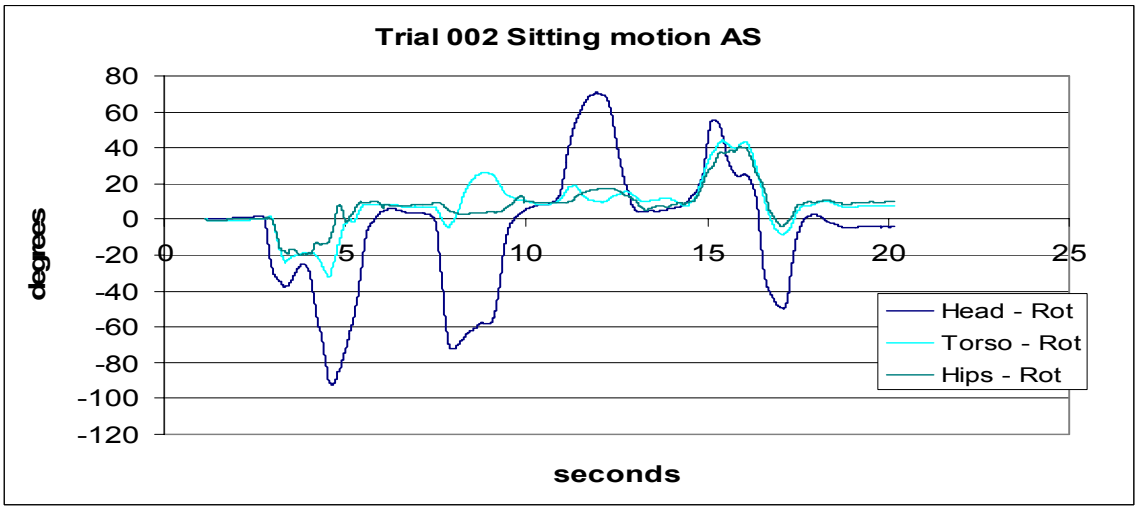
Trial 002 Sitting motion AS
80
60
40
20
0
-20
-40
-60
-80
-100
-120
degrees
0
5
10
15
20
25
seconds
Head - Rot
Torso - Rot
Hips - Rot

Appendix E: Task 2 Results for Spinal Motion Analysis Using Tilt/Twist Method

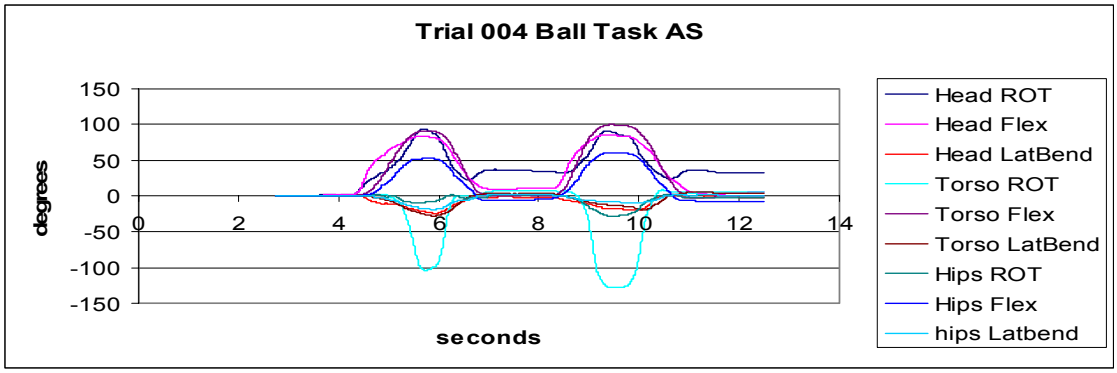
Trial 004 Ball Task AS
150
100
50
0
-50
-100
-150
degrees
0
2
4
6
8
10
12
14
seconds
Head ROT
Head Flex
Head LatBend
Torso ROT
Torso Flex
Torso LatBend
Hips ROT
Hips Flex
hips Latbend

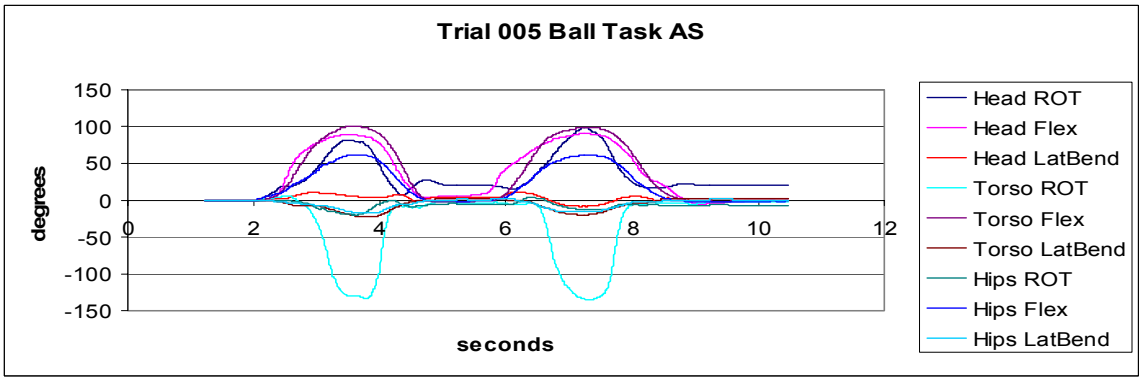
Trial 005 Ball Task AS
150
100
50
0
-50
-100
-150
degrees
0
2
4
6
8
10
12
seconds
Head ROT
Head Flex
Head LatBend
Torso ROT
Torso Flex
Torso LatBend
Hips ROT
Hips Flex
Hips LatBend

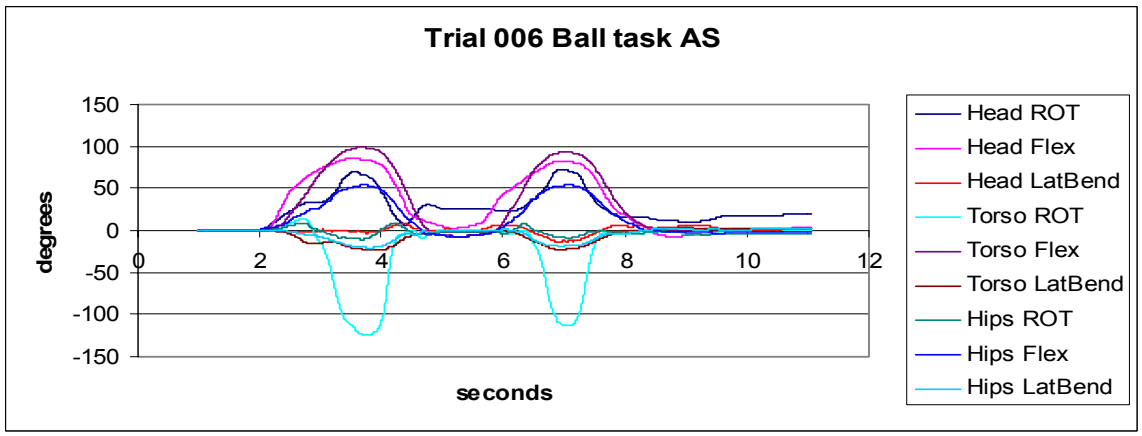
Trial 006 Ball task AS
150
100
50
0
-50
-100
-150
degrees
0
2
4
6
8
10
12
seconds
Head ROT
Head Flex
Head LatBend
Torso ROT
Torso Flex
Torso LatBend
Hips ROT
Hips Flex
Hips LatBend

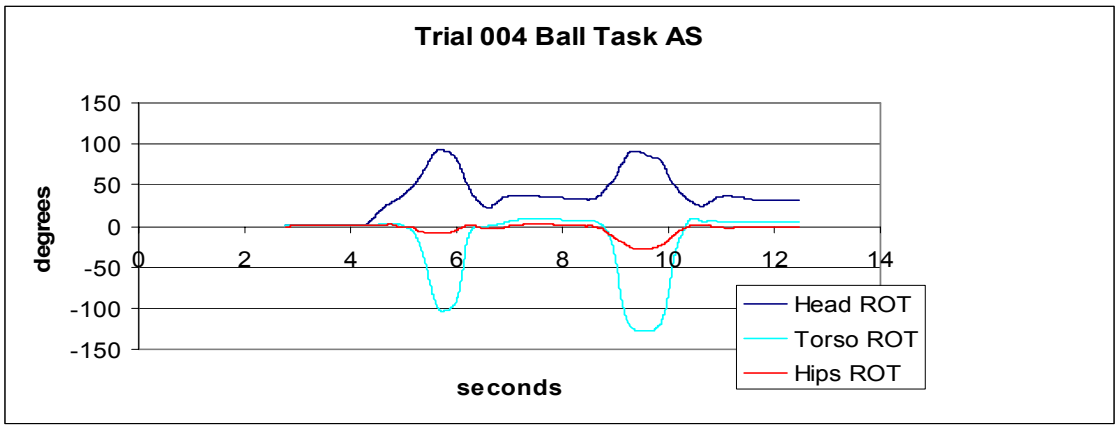
Trial 004 Ball Task AS
150
100
50
0
-50
-100
-150
degrees
0
2
4
6
8
10
12
14
seconds
Head ROT
Torso ROT
Hips ROT

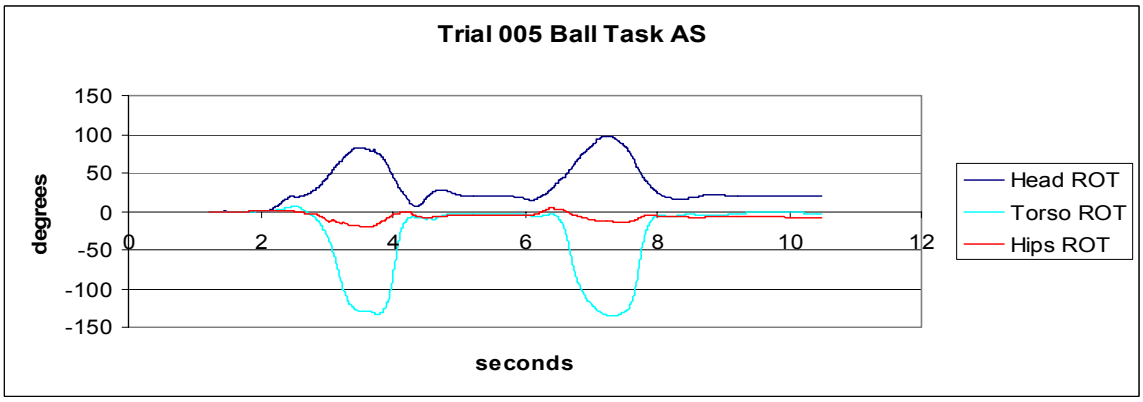
Trial 005 Ball Task AS
150
100
50
0
-50
-100
-150
degrees
0
2
4
6
8
10
12
seconds
Head ROT
Torso ROT
Hips ROT

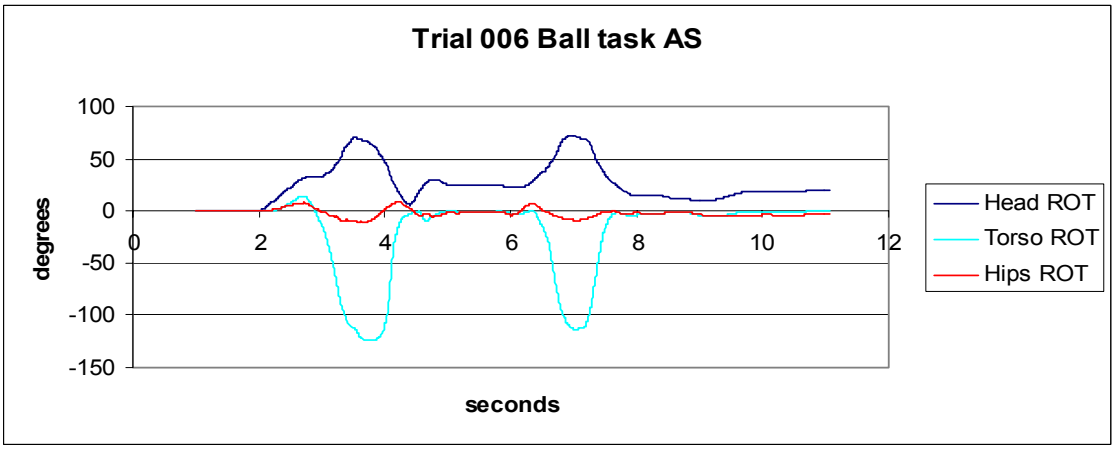
Trial 006 Ball task AS
100
50
0
-50
-100
-150
degrees
0
2
4
6
8
10
12
seconds
Head ROT
Torso ROT
Hips ROT

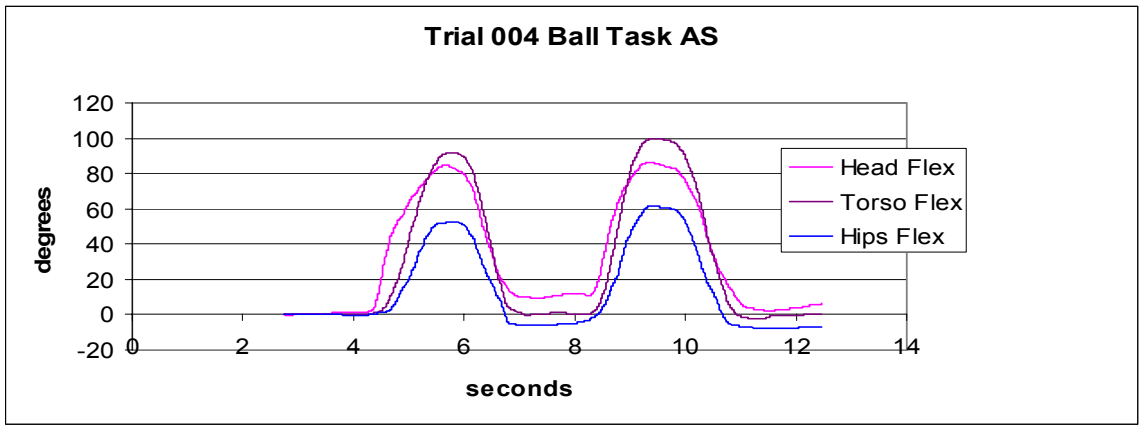
Trial 004 Ball Task AS
degrees
120
100
80
60
40
20
0
-20
0
2
4
6
8
10
12
14
seconds
Head Flex
Torso Flex
Hips Flex

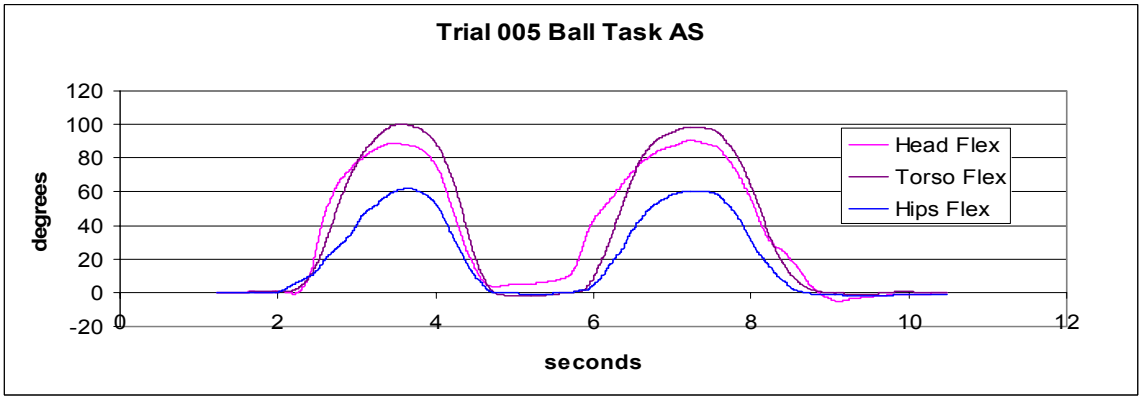
Trial 005 Ball Task AS
degrees
120
100
80
60
40
20
0
-20
0
2
4
6
8
10
12
seconds
Head Flex
Torso Flex
Hips Flex

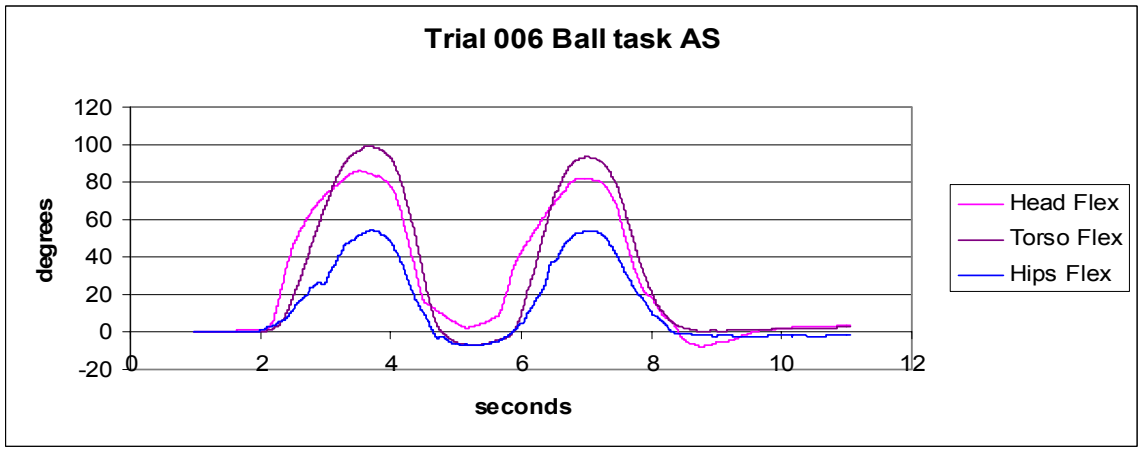
Trial 006 Ball task AS
degrees
120
100
80
60
40
20
0
-20
0
2
4
6
8
10
12
seconds
Head Flex
Torso Flex
Hips Flex

Appendix F: Task 3 Results for Spinal Motion Analysis Using Tilt/Twist Method

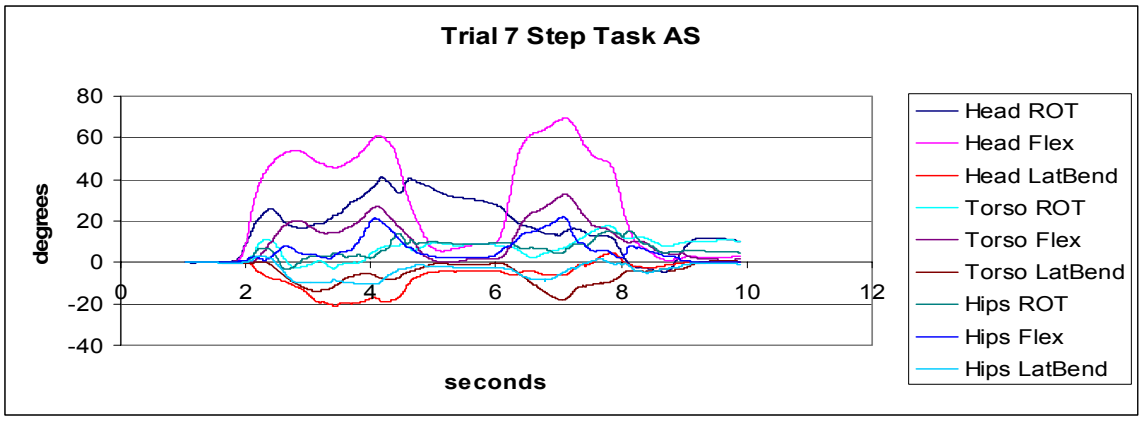
Trial 7 Step Task AS
degrees
seconds
Head ROT
Head Flex
Head LatBend
Torso ROT
Torso Flex
Torso LatBend
Hips ROT
Hips Flex
Hips LatBend

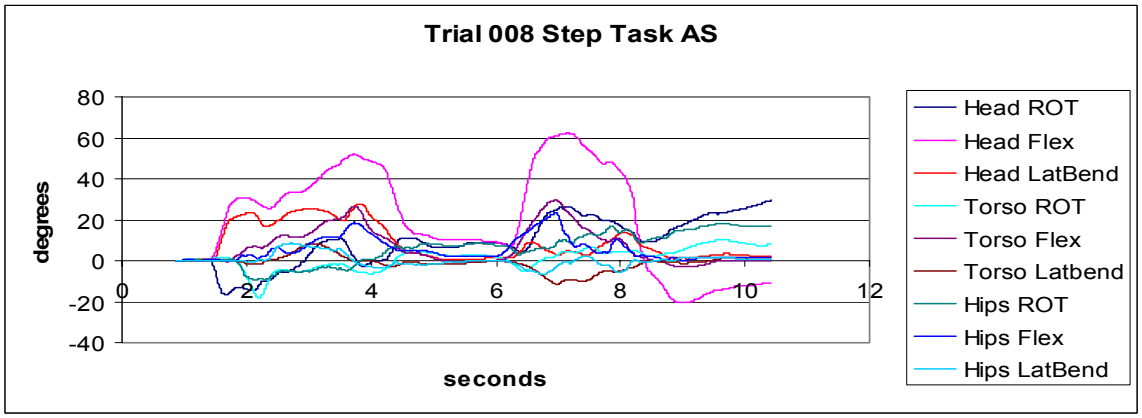
Trial 008 Step Task AS
degrees
seconds
Head ROT
Head Flex
Head LatBend
Torso ROT
Torso Flex
Torso Latbend
Hips ROT
Hips Flex
Hips LatBend

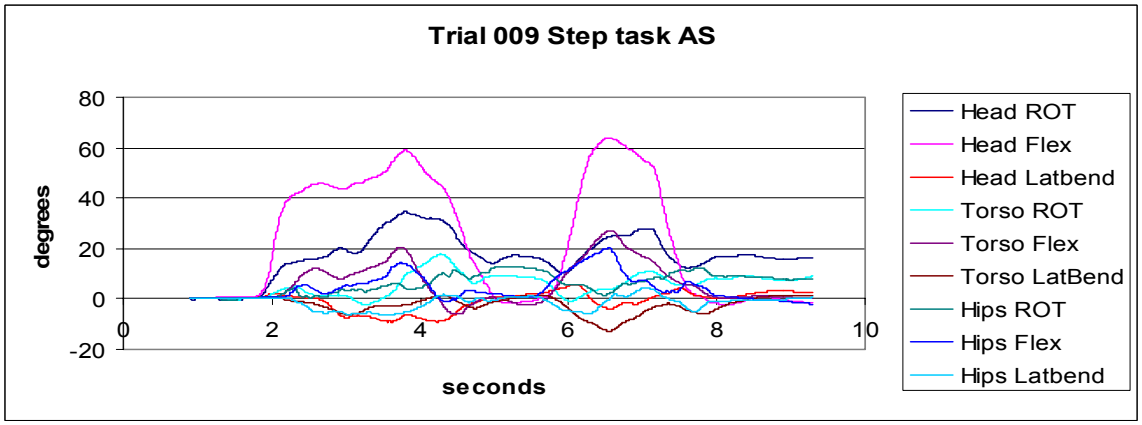
Trial 009 Step task AS
degrees
seconds
Head ROT
Head Flex
Head Latbend
Torso ROT
Torso Flex
Torso LatBend
Hips ROT
Hips Flex
Hips Latbend

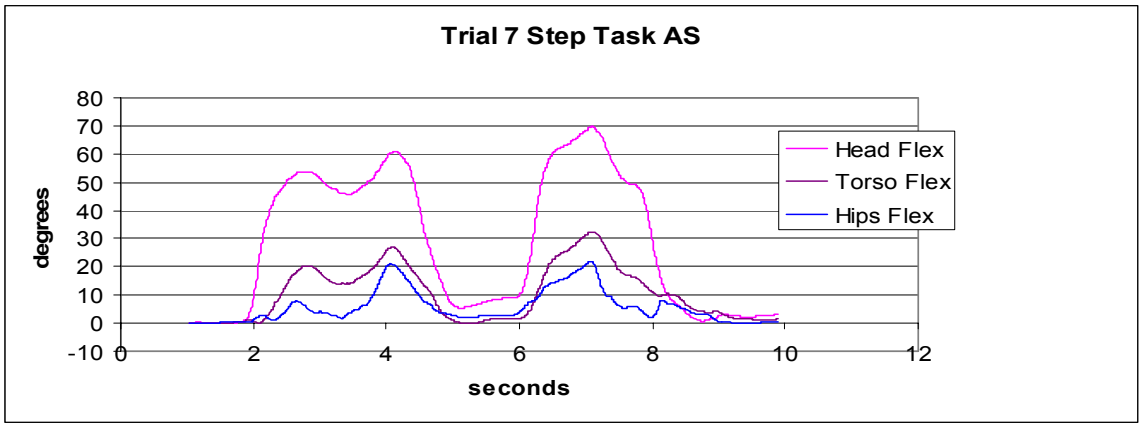
Trial 7 Step Task AS
degrees
80
70
60
50
40
30
20
10
0
-10
0
2
4
6
8
10
12
seconds
Head Flex
Torso Flex
Hips Flex

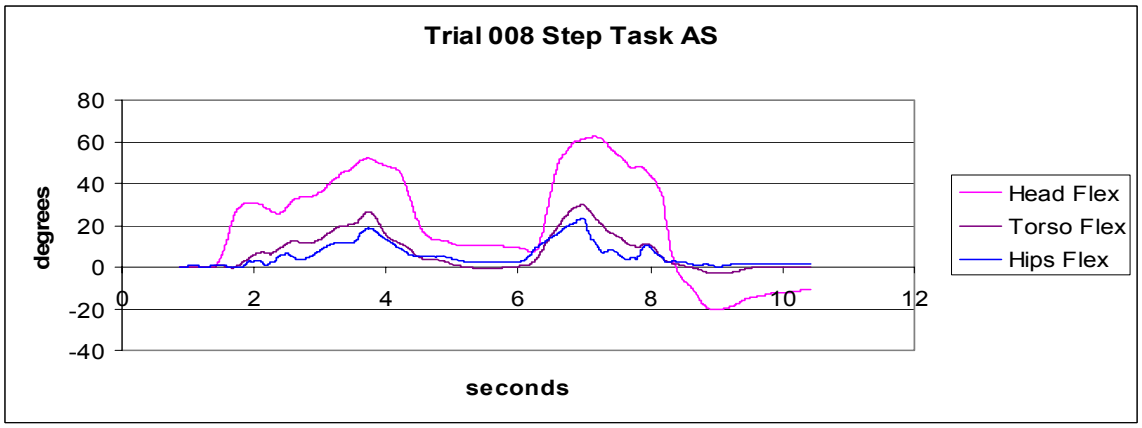
Trial 008 Step Task AS
degrees
80
60
40
20
0
-20
-40
0
2
4
6
8
10
12
seconds
Head Flex
Torso Flex
Hips Flex

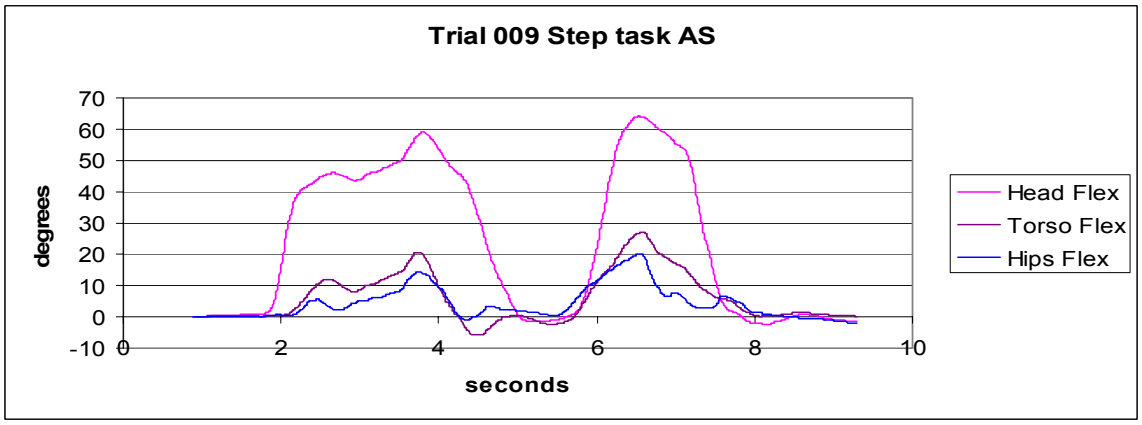
Trial 009 Step task AS
degrees
70
60
50
40
30
20
10
0
-10
0
2
4
6
8
10
seconds
Head Flex
Torso Flex
Hips Flex

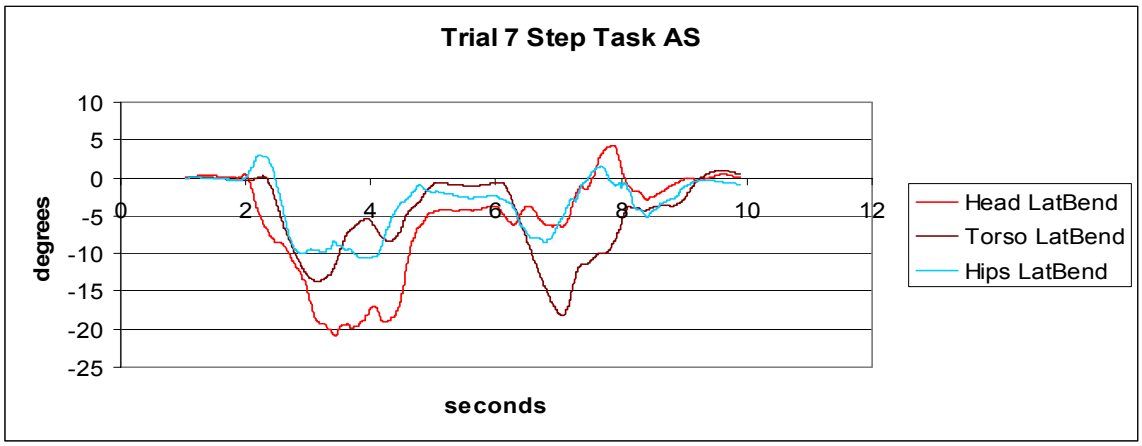
Trial 7 Step Task AS
10
5
0
-5
-10
-15
-20
-25
degrees
0
2
4
6
8
10
12
seconds
Head LatBend
Torso LatBend
Hips LatBend

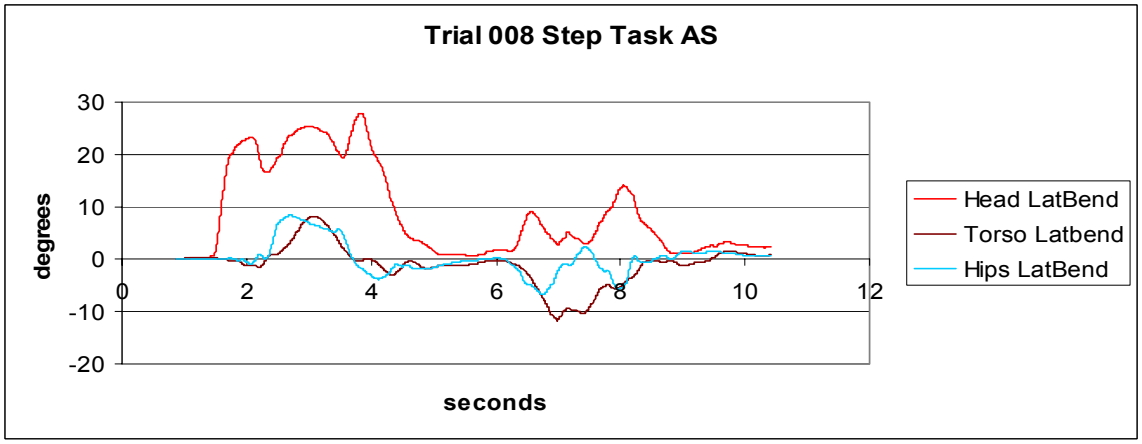
Trial 008 Step Task AS
30
20
10
0
-10
-20
degrees
0
2
4
6
8
10
12
seconds
Head LatBend
Torso Latbend
Hips LatBend

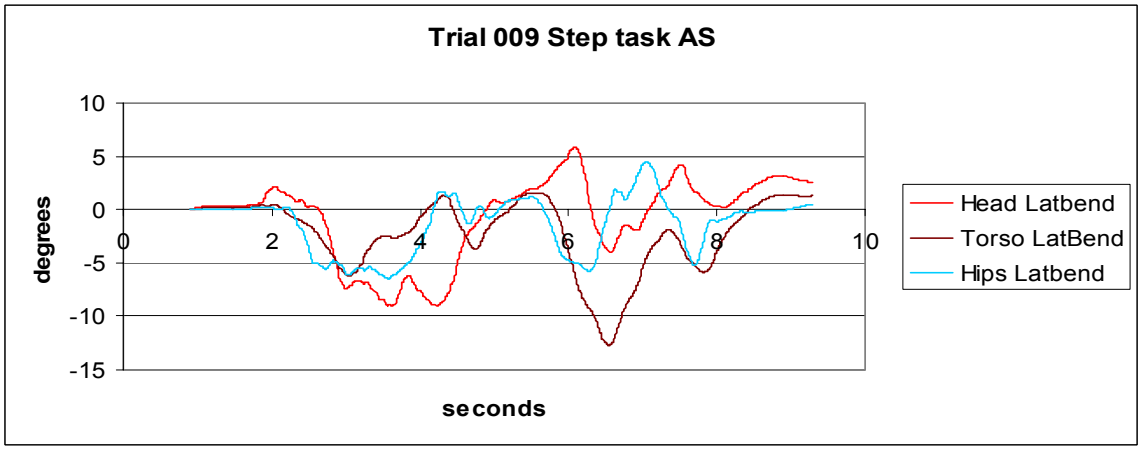
Trial 009 Step task AS
10
5
0
-5
-10
-15
degrees
0
2
4
6
8
10
seconds
Head Latbend
Torso LatBend
Hips Latbend

Appendix G: Rotation Matrix Singularity Zones Resulting from Use of Tilt/Twist Method

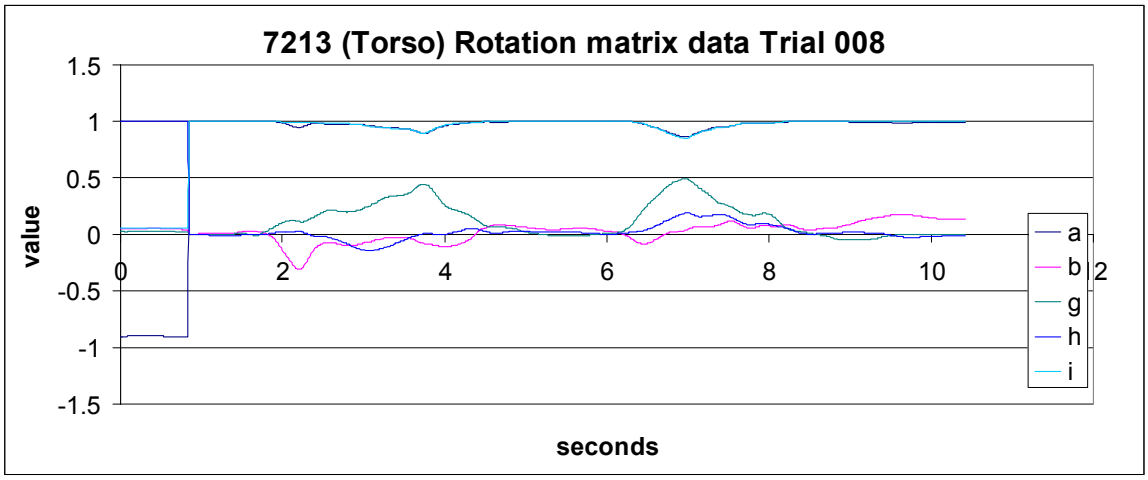
7213 (Torso) Rotation matrix data Trial 008
1.5
1
0.5
0
-0.5
-1
-1.5
value
0
2
4
6
8
10
12
a
b
g
h
i
seconds

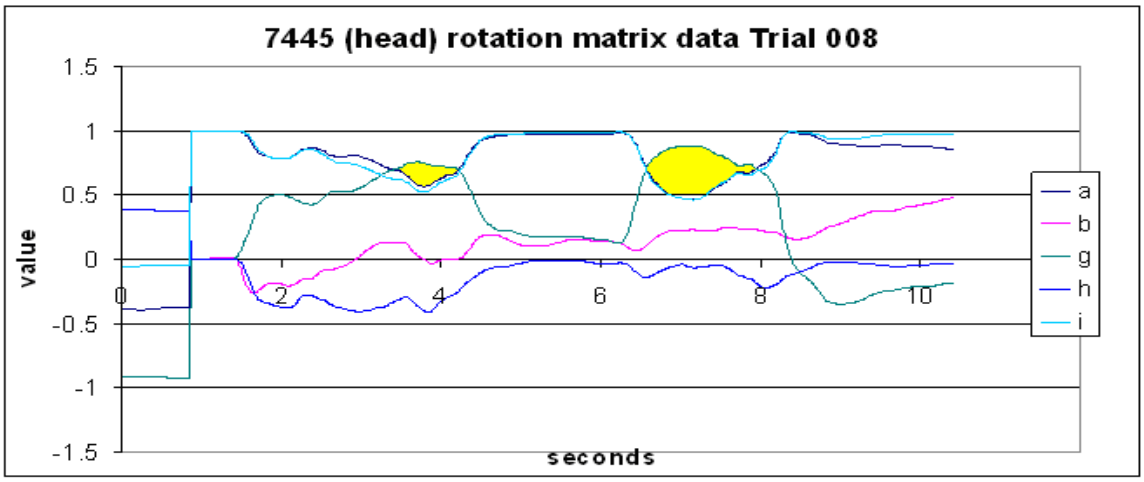
7445 (head) rotation matrix data Trial 008
1.5
1
0.5
0
-0.5
-1
-1.5
value
0
2
4
6
8
10
a
b
g
h
i
seconds

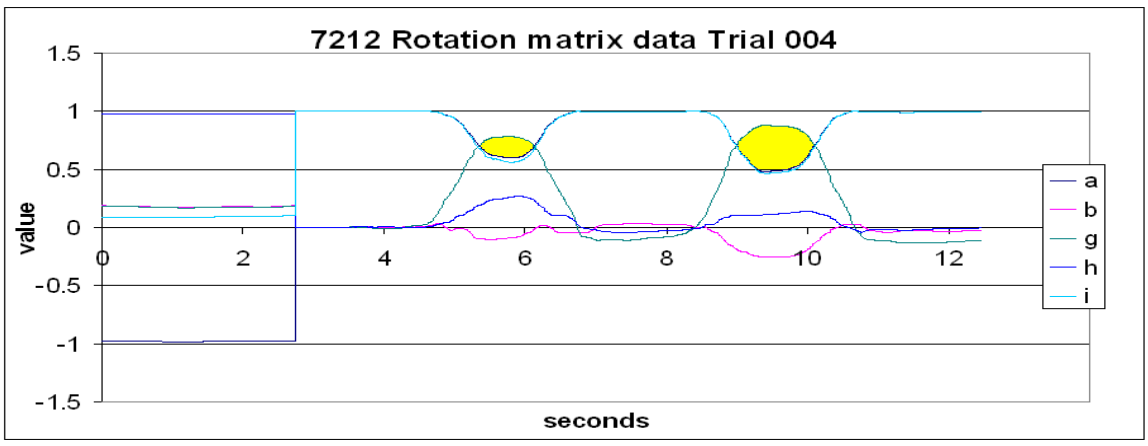
7212 Rotation matrix data Trial 004
1.5
1
0.5
0
-0.5
-1
-1.5
value
0
2
4
6
8
10
12
a
b
g
h
i
seconds

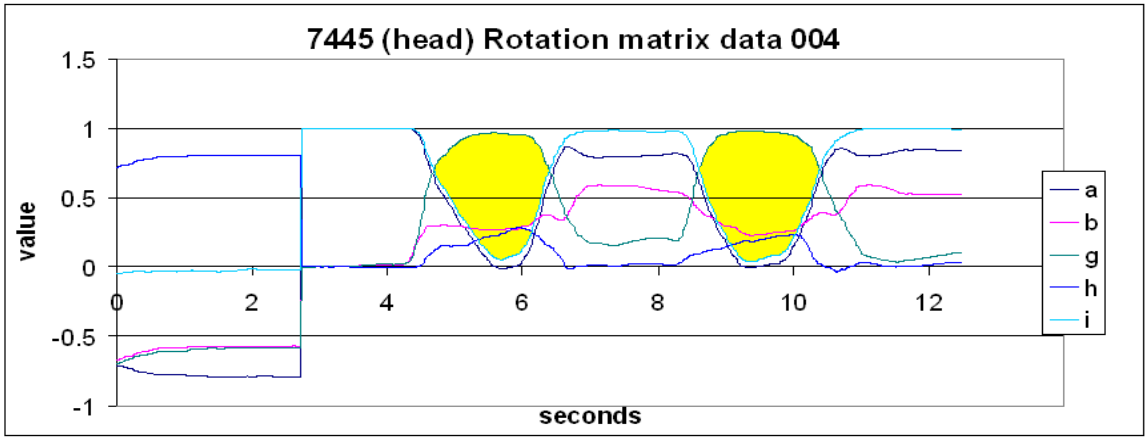
7445 (head) Rotation matrix data 004
1.5
1
0.5
0
-0.5
-1
value
0
2
4
6
8
10
12
seconds
a
b
g
h
i

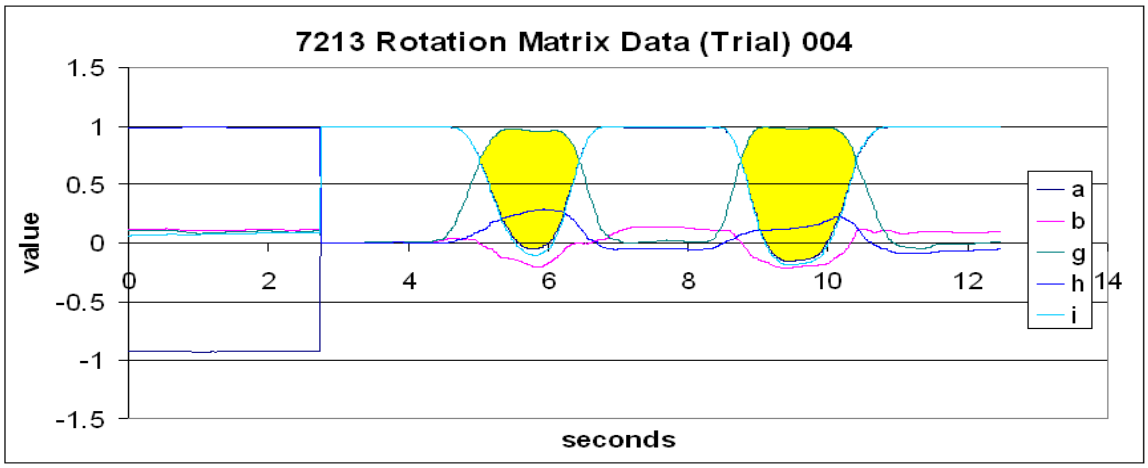
7213 Rotation Matrix Data (Trial) 004
1.5
1
0.5
0
-0.5
-1
-1.5
value
0
2
4
6
8
10
12
14
seconds
a
b
g
h
i

Appendix H: Ethics Approval Certificates for Subject Testing

University of Victoria

UVic/VIHA Joint Research Ethics Sub-Committee
Human Research Ethics, University of Victoria
PO Box 1700, Stn CSC, Victoria BC, V8W 2Y2
Tel (250) 472-4545 Fax (250) 721-7836 Web www.research.uvic.ca

VANCOUVER ISLAND health authority

Vancouver Island Health Authority, Memorial Pavilion, Kenning Wing
1952 Bay Street, Victoria BC, V8R 1J8
Tel (250) 370-8261 Fax (250) 370-8106 Web www.viha.ca

UVic/VIHA Joint Research Ethics Sub-Committee
Certificate of Approval

Principal Investigator	Department/School	Supervisor
Christina Goodvin **Master's Student**	**MENG**	**Dr. Edward Park**
Co-Investigator(s): **Jungkeun Lee** **Kevin Huang**		

Project Title: **The development of a three dimensional spinal motion measurement system for clinical practice**

Protocol No.	Approval Date	Start Date	End Date
06-2006-36b	**27-Oct-06**	**10-May-06**	**09-May-07**

Certification

This certifies that the UVic/VIHA Joint Research Ethics Sub-Committee has examined this research protocol and concludes that, in all respects, the proposed research meets appropriate standards of ethics as outlined by the University of Victoria Research Regulations Involving Human Subjects and the Vancouver Island Health Authority Research and Evaluation administration.

Dr. Richard Keeler
Associate Vice-President, Research, UVic

Dr. Peter Kirk
Director, Research and Academic Dev't, VIHA

This Certificate of Approval is valid for the above term provided there is no change in the procedures. Extensions or minor amendments may be granted upon receipt of "Request for Continuing Review or Amendment of an Approved Project" form.

06-2006-36b Goodvin, Christina

University of Victoria

UVic/VIHA Joint Research Ethics Sub-Committee
Office of Research Services, University of Victoria
PO Box 3025, Stn CSC, Victoria BC, V8W 2Y2
Tel (250) 472-4545 Fax (250) 721-8960 Web www.research.uvic.ca

VANCOUVER ISLAND health authority

Vancouver Island Health Authority, Memorial Pavilion, Kenning Wing
1952 Bay Street, Victoria BC, V8R 1J8
Tel (250) 370-8261 Fax (250) 370-8106 Web www.viha.ca

UVic/VIHA Joint Research Ethics Sub-Committee
Certificate of Approval

Principal Investigator	Department/School	Supervisor
Christina Goodvin **Graduate Student**	**MENG**	**Dr. Edward Park**

Co-Investigator(s):

Kel Sakaki, Software Programmer, MENG, UVic
Edmund Haslam, Electronic Technician, MENG, UVic
Kevin Huang, Software Programmer, MENG, UVic
Dr. Edward Park, Co-Principal Investigator, MENG, UVic
Dr. Naznin Virji-Babul, Collaborator, QACCH

Project Title: **The development of a three dimensional spinal motion measurement system for clinical practice**

Protocol No.	Approval Date	Start Date	End Date
2006-36	**10-May-06**	**10-May-06**	**09-May-07**

Certification

This certifies that the UVic/VIHA Joint Research Ethics Sub-Committee has examined this research protocol and concludes that, in all respects, the proposed research meets appropriate standards of ethics as outlined by the University of Victoria Research Regulations Involving Human Subjects and the Vancouver Island Health Authority Research and Evaluation administration.

Dr. Richard Keeler
Associate Vice-President, Research, UVic

Dr. Peter Kirk
Director, Research and Academic Dev't, VIHA

This Certificate of Approval is valid for the above term provided there is no change in the procedures. Extensions or minor amendments may be granted upon receipt of "Request for Continuing Review or Amendment of an Approved Project" form.

2006-36 Goodvin, Christina

Appendix I: Corrected Task 1 Results for Spinal Motion Analysis

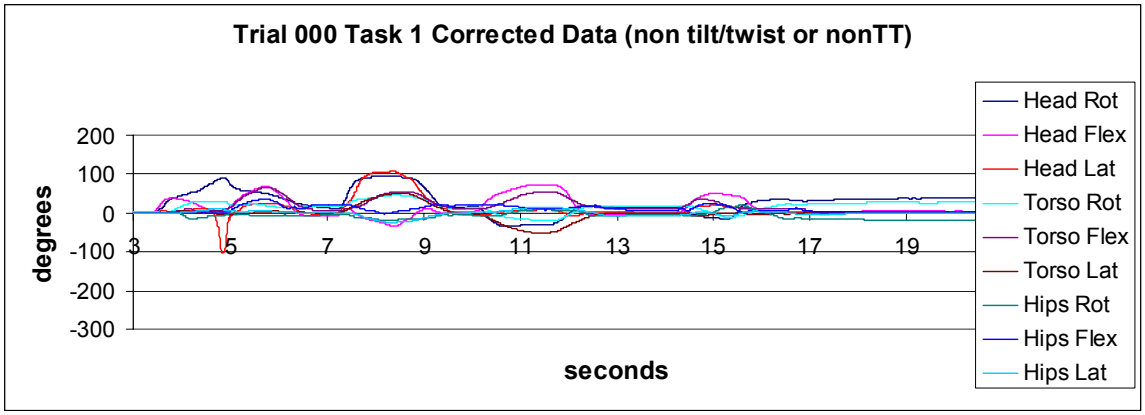
Trial 000 Task 1 Corrected Data (non tilt/twist or nonTT)
degrees
200
100
0
-100
-200
-300
3
5
7
9
11
13
15
17
19
seconds
Head Rot
Head Flex
Head Lat
Torso Rot
Torso Flex
Torso Lat
Hips Rot
Hips Flex
Hips Lat

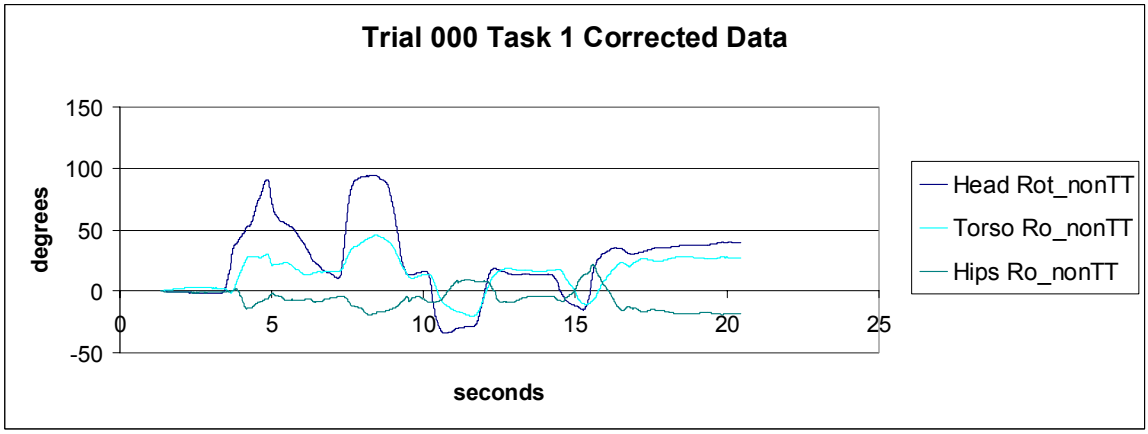
Trial 000 Task 1 Corrected Data
degrees
150
100
50
0
-50
0
5
10
15
20
25
seconds
Head Rot_nonTT
Torso Ro_nonTT
Hips Ro_nonTT

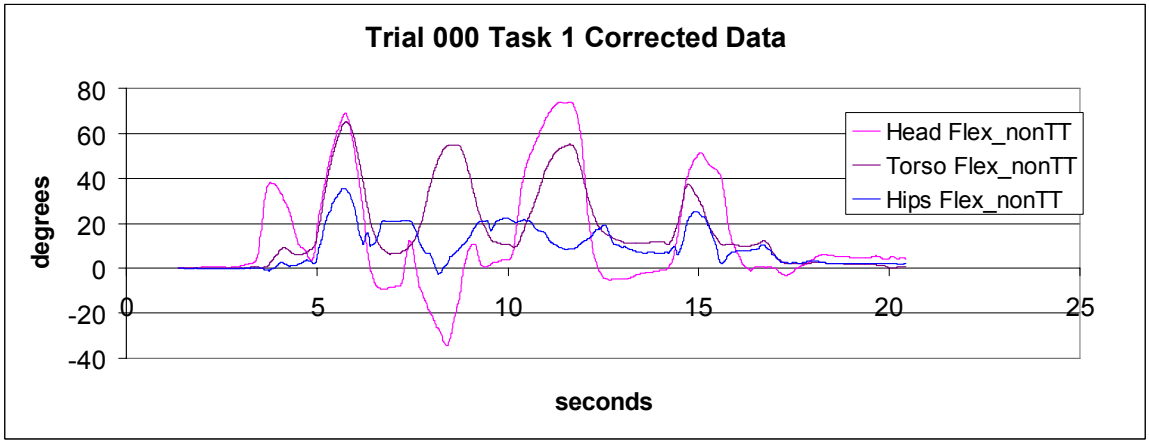
Trial 000 Task 1 Corrected Data
degrees
80
60
40
20
0
-20
-40
0
5
10
15
20
25
seconds
Head Flex_nonTT
Torso Flex_nonTT
Hips Flex_nonTT

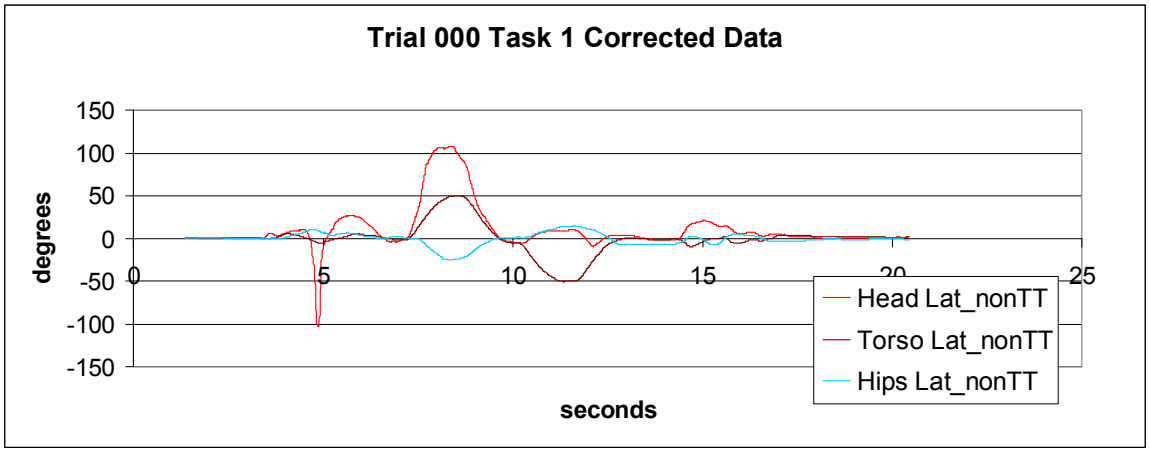
Trial 000 Task 1 Corrected Data
150
100
50
0
-50
-100
-150
degrees
0
5
10
15
20
25
seconds
Head Lat_nonTT
Torso Lat_nonTT
Hips Lat_nonTT

Appendix J: Corrected Task 2 Results for Spinal Motion Analysis

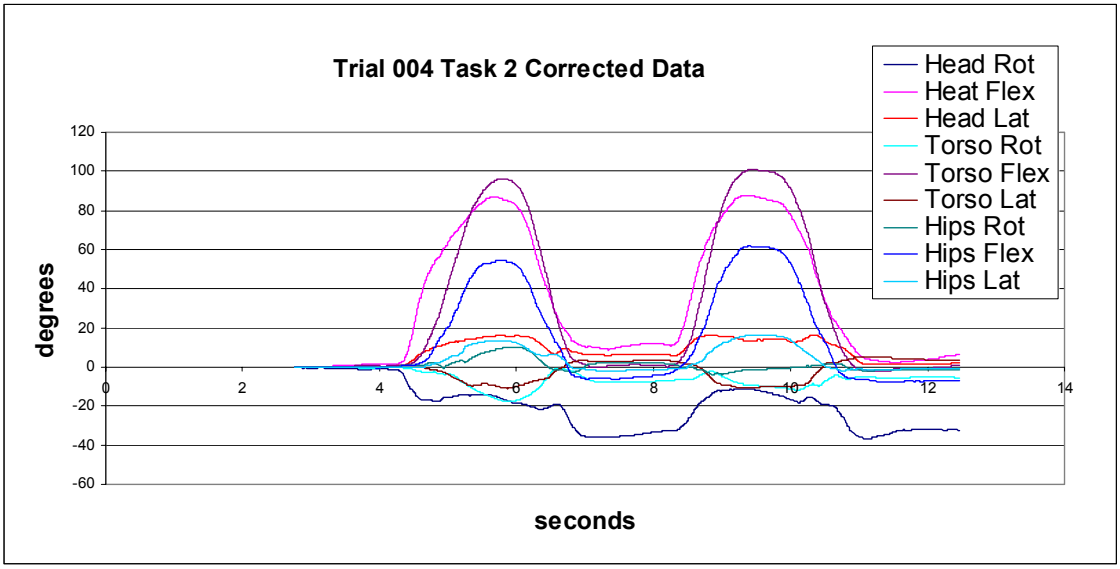
Trial 004 Task 2 Corrected Data
Head Rot
Heat Flex
Head Lat
Torso Rot
Torso Flex
Torso Lat
Hips Rot
Hips Flex
Hips Lat
120
100
80
60
40
20
0
-20
-40
-60
degrees
0
2
4
6
8
10
12
14
seconds

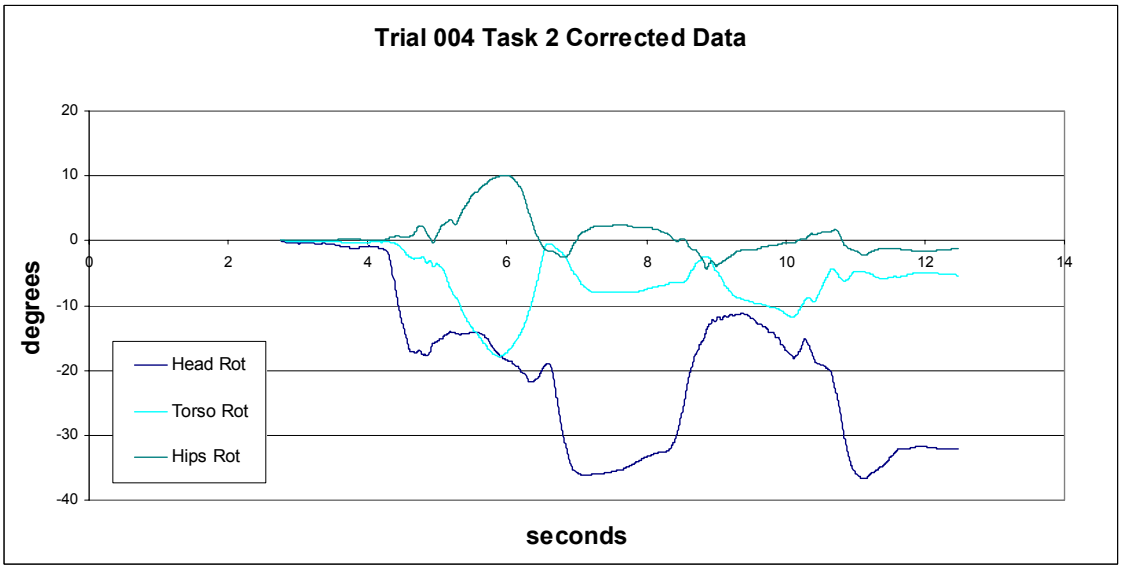
Trial 004 Task 2 Corrected Data
20
10
0
-10
-20
-30
-40
degrees
0
2
4
6
8
10
12
14
Head Rot
Torso Rot
Hips Rot
seconds

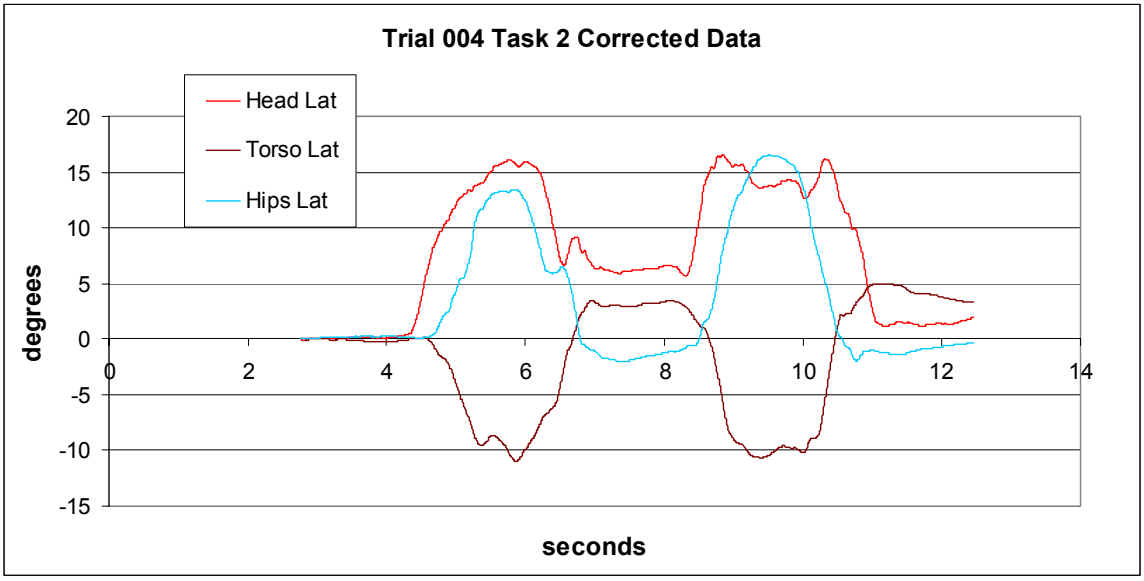
Trial 004 Task 2 Corrected Data
Head Lat
Torso Lat
Hips Lat
degrees
seconds
20
15
10
5
0
-5
-10
-15
0
2
4
6
8
10
12
14

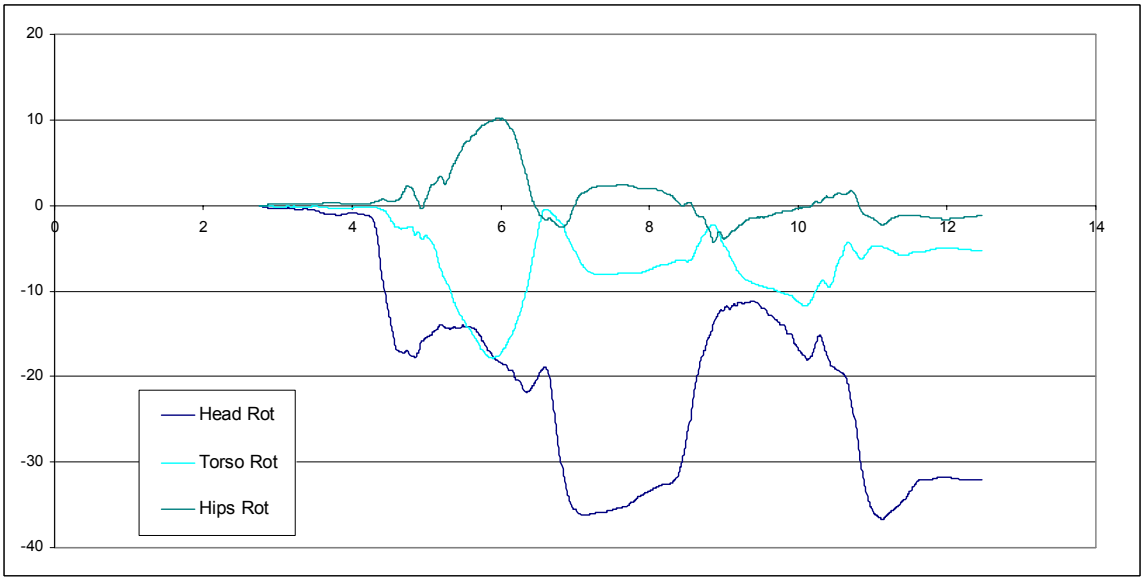
20
10
0
-10
-20
-30
-40
0
2
4
6
8
10
12
14
Head Rot
Torso Rot
Hips Rot

Appendix K: GVS Results

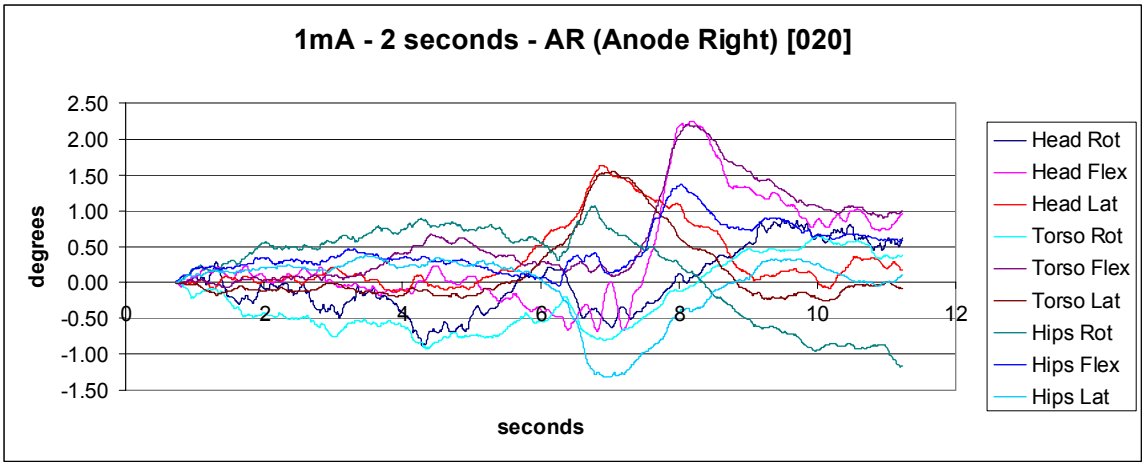
1mA - 2 seconds - AR (Anode Right) [020]
degrees
seconds
Head Rot
Head Flex
Head Lat
Torso Rot
Torso Flex
Torso Lat
Hips Rot
Hips Flex
Hips Lat

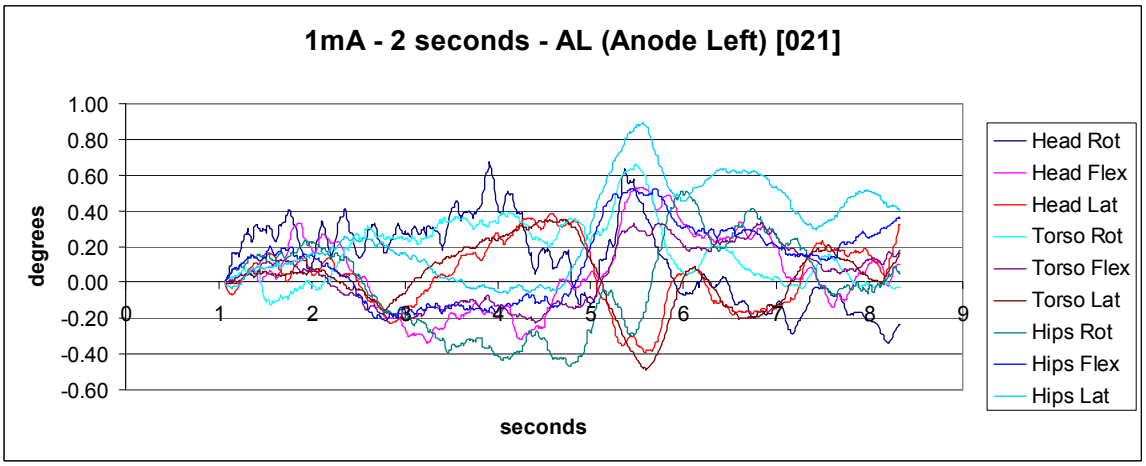
1mA - 2 seconds - AL (Anode Left) [021]
degrees
seconds
Head Rot
Head Flex
Head Lat
Torso Rot
Torso Flex
Torso Lat
Hips Rot
Hips Flex
Hips Lat

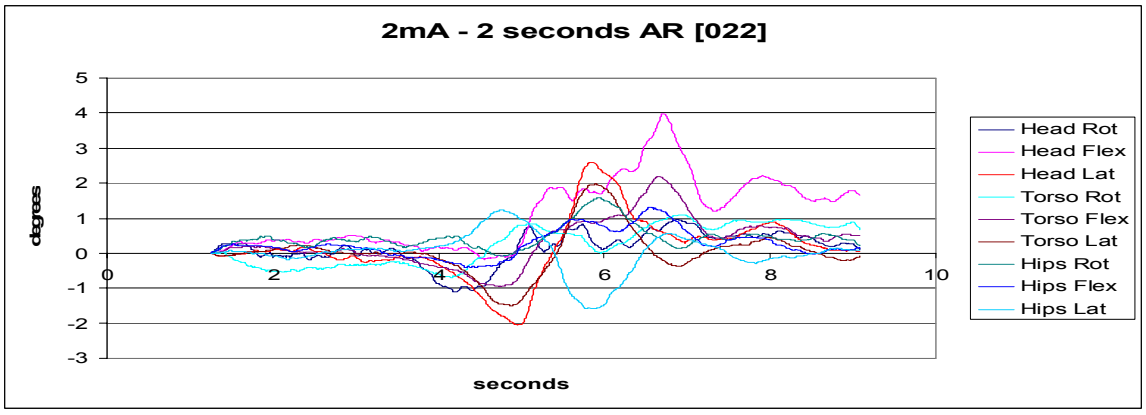
2mA - 2 seconds AR [022]
degrees
seconds
Head Rot
Head Flex
Head Lat
Torso Rot
Torso Flex
Torso Lat
Hips Rot
Hips Flex
Hips Lat

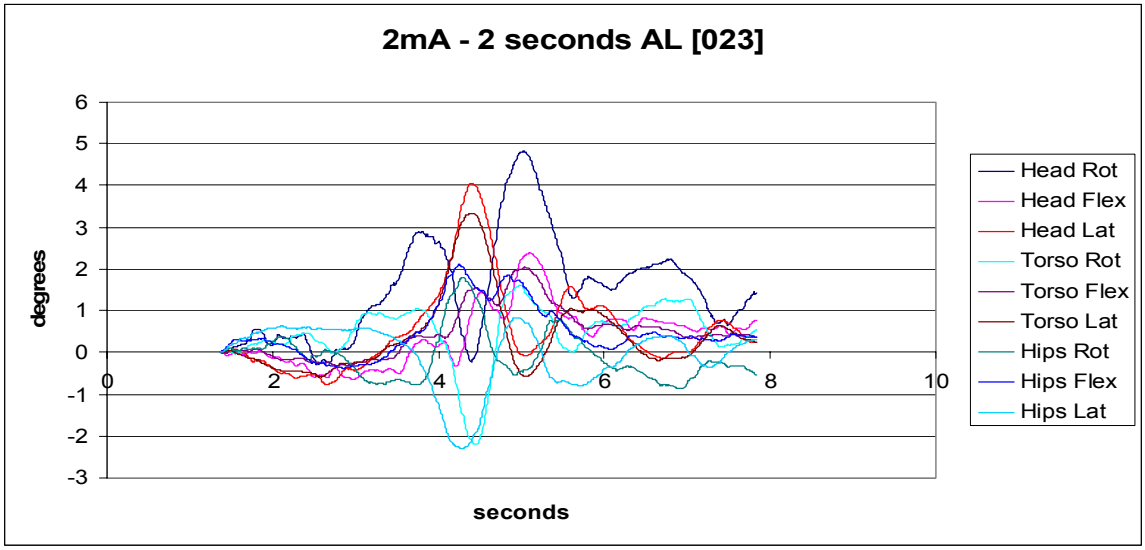
2mA - 2 seconds AL [023]
degrees
seconds
Head Rot
Head Flex
Head Lat
Torso Rot
Torso Flex
Torso Lat
Hips Rot
Hips Flex
Hips Lat

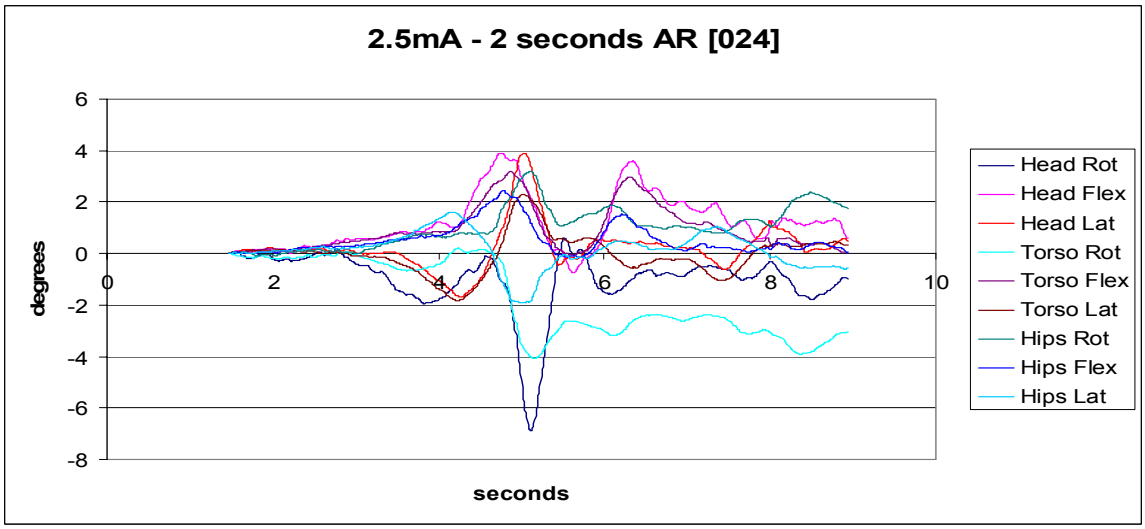
2.5mA - 2 seconds AR [024]
degrees
seconds
Head Rot
Head Flex
Head Lat
Torso Rot
Torso Flex
Torso Lat
Hips Rot
Hips Flex
Hips Lat

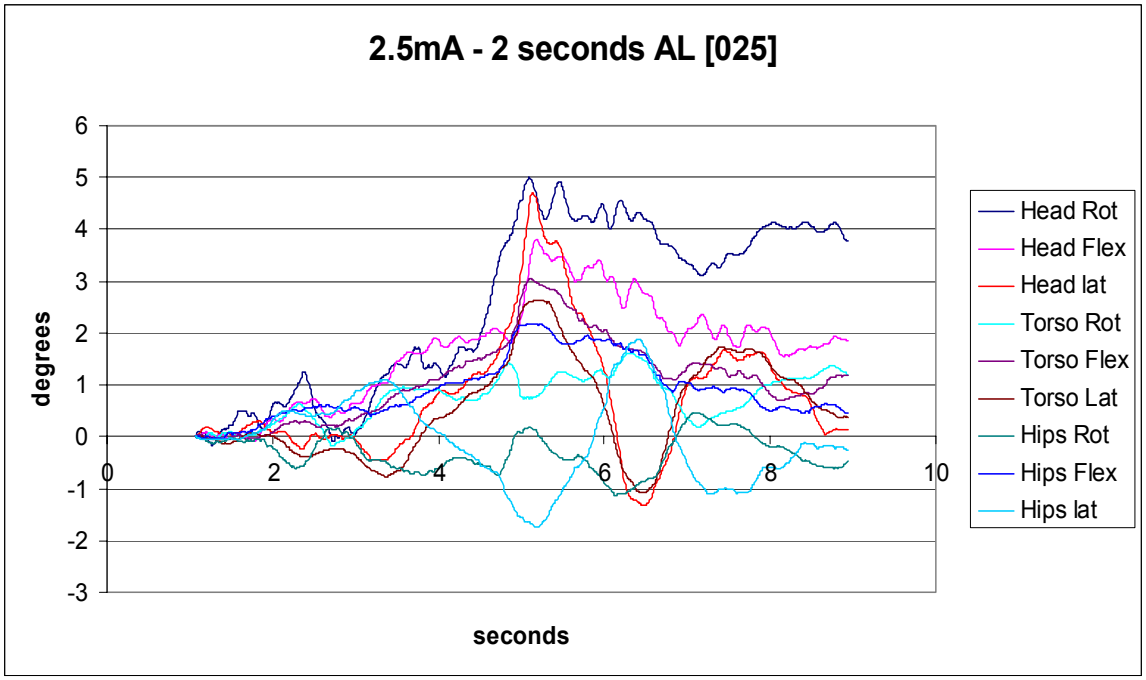
2.5mA - 2 seconds AL [025]
degrees
seconds
Head Rot
Head Flex
Head lat
Torso Rot
Torso Flex
Torso Lat
Hips Rot
Hips Flex
Hips lat

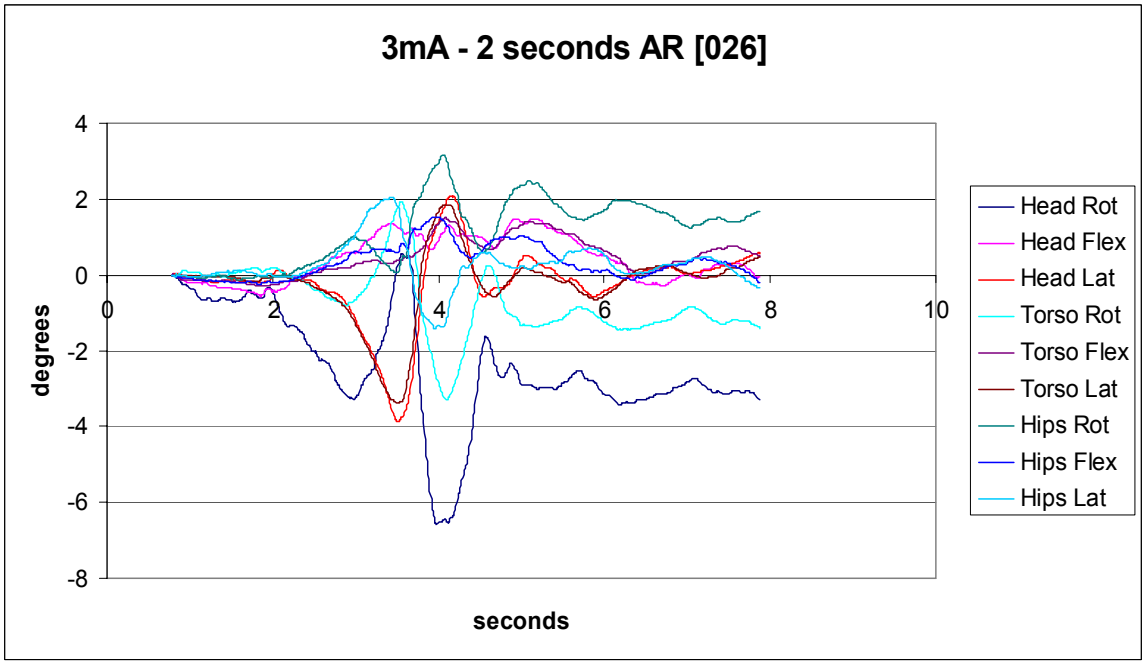
3mA - 2 seconds AR [026]
degrees
seconds
Head Rot
Head Flex
Head Lat
Torso Rot
Torso Flex
Torso Lat
Hips Rot
Hips Flex
Hips Lat

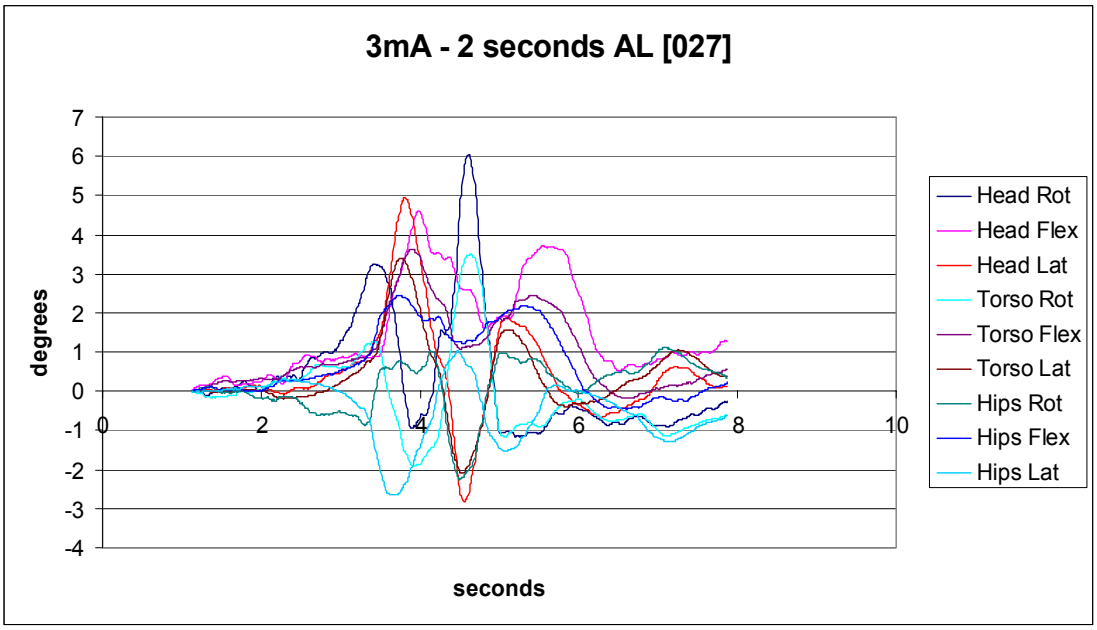
3mA - 2 seconds AL [027]
degrees
seconds
Head Rot
Head Flex
Head Lat
Torso Rot
Torso Flex
Torso Lat
Hips Rot
Hips Flex
Hips Lat

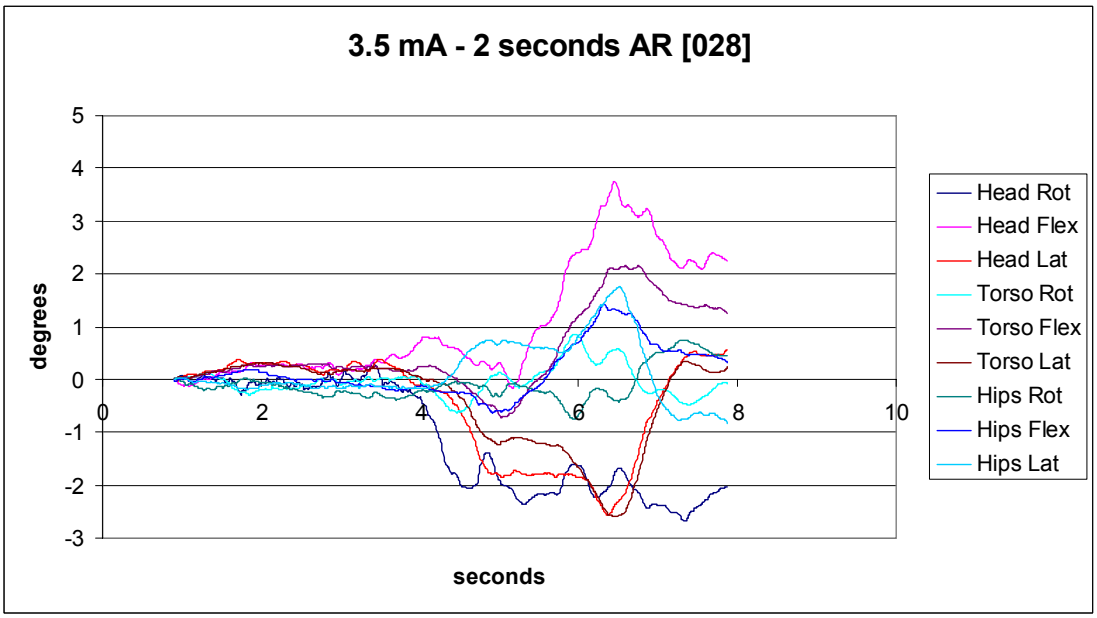
3.5 mA - 2 seconds AR [028]
degrees
seconds
Head Rot
Head Flex
Head Lat
Torso Rot
Torso Flex
Torso Lat
Hips Rot
Hips Flex
Hips Lat

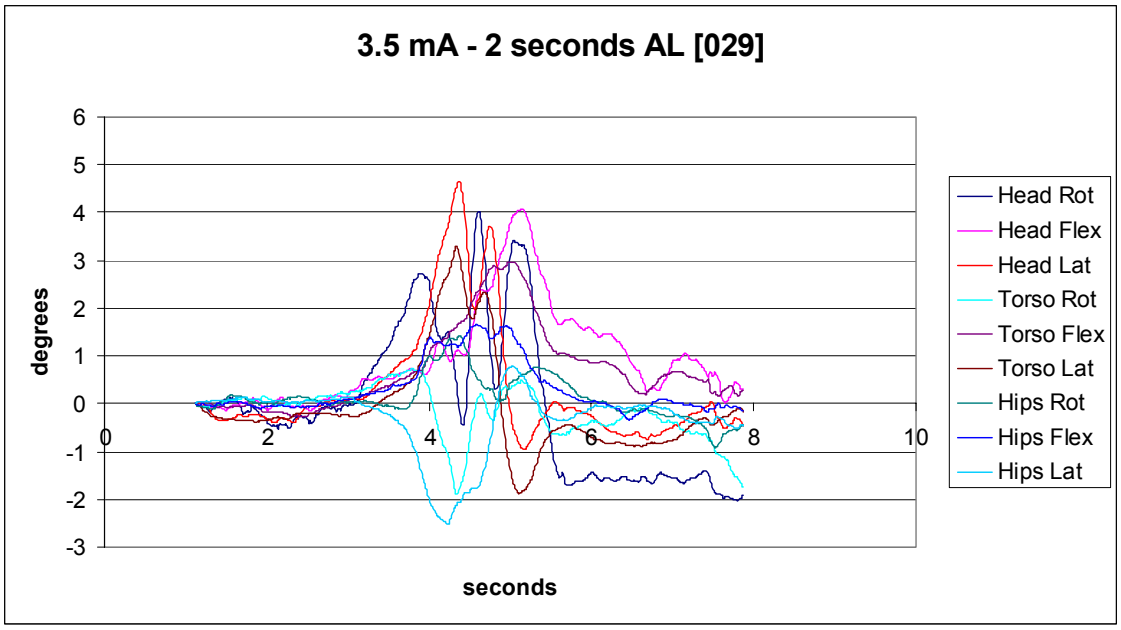
3.5 mA - 2 seconds AL [029]
degrees
seconds
Head Rot
Head Flex
Head Lat
Torso Rot
Torso Flex
Torso Lat
Hips Rot
Hips Flex
Hips Lat

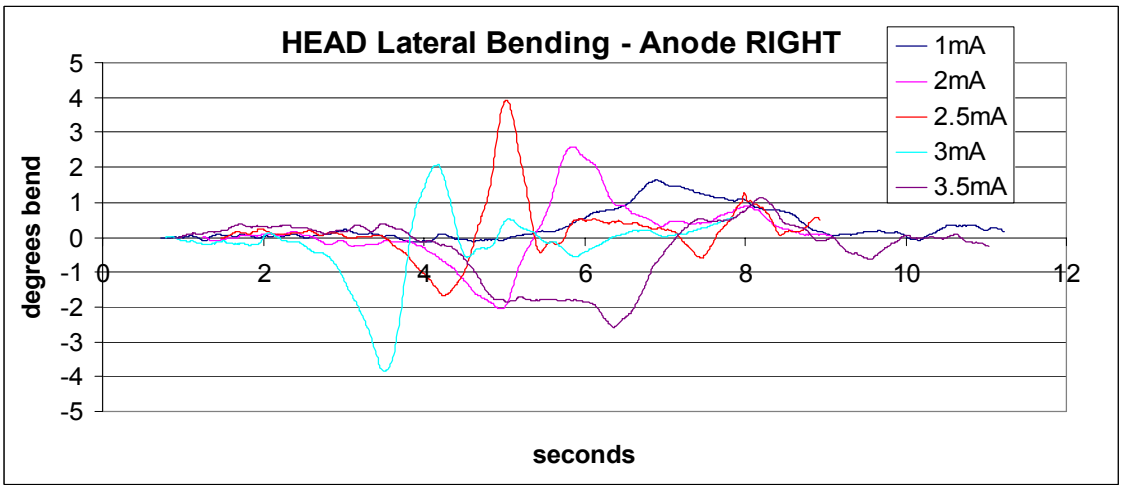
HEAD Lateral Bending - Anode RIGHT
degrees bend
seconds
1mA
2mA
2.5mA
3mA
3.5mA

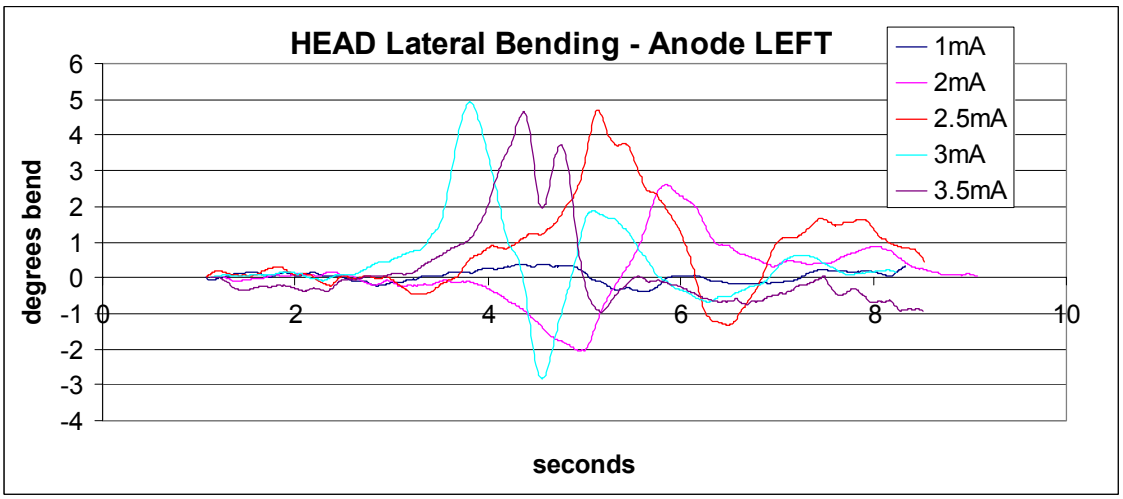
HEAD Lateral Bending - Anode LEFT
degrees bend
seconds
1mA
2mA
2.5mA
3mA
3.5mA

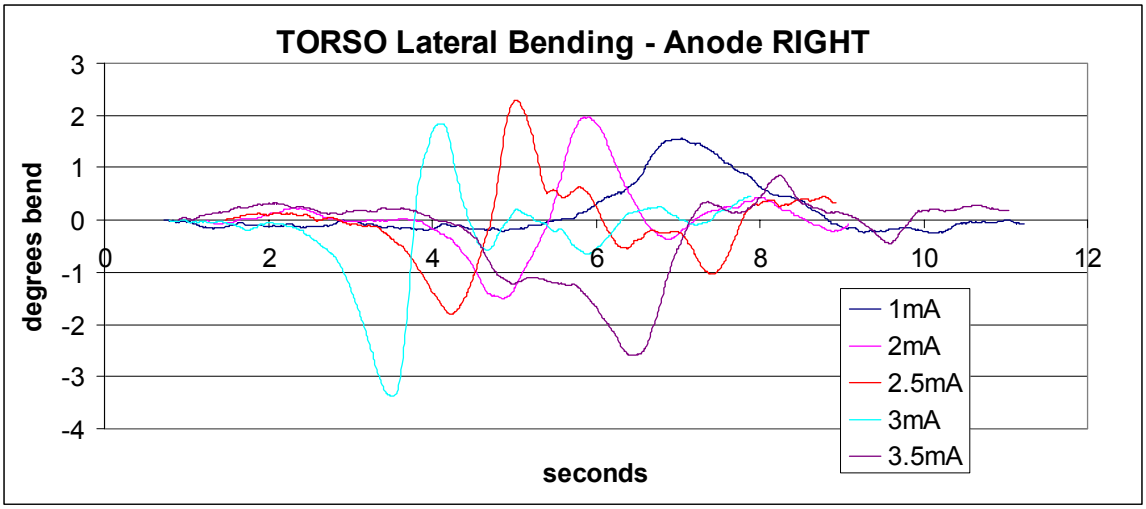
TORSO Lateral Bending - Anode RIGHT
degrees bend
seconds
1mA
2mA
2.5mA
3mA
3.5mA

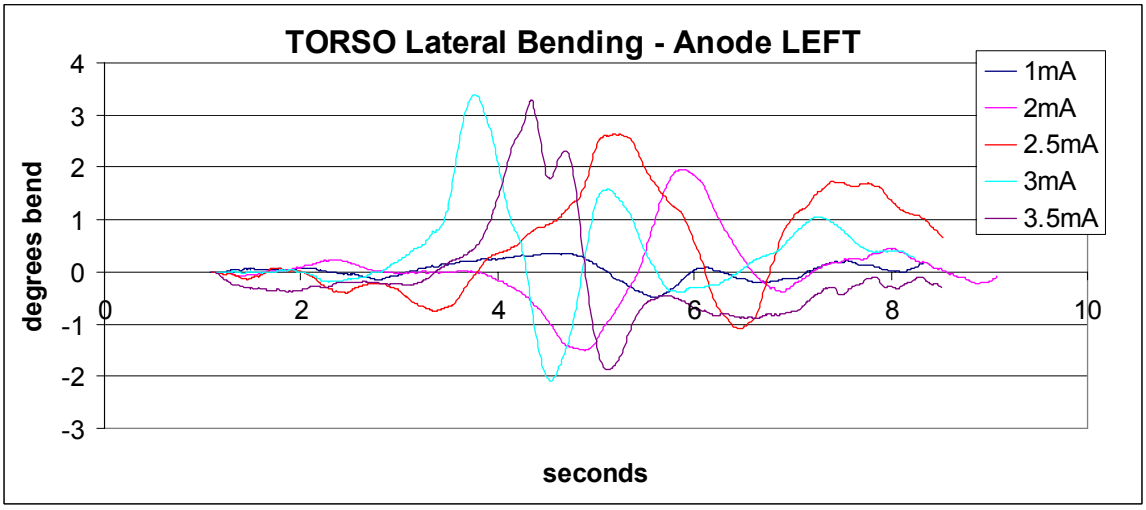
TORSO Lateral Bending - Anode LEFT
degrees bend
seconds
1mA
2mA
2.5mA
3mA
3.5mA

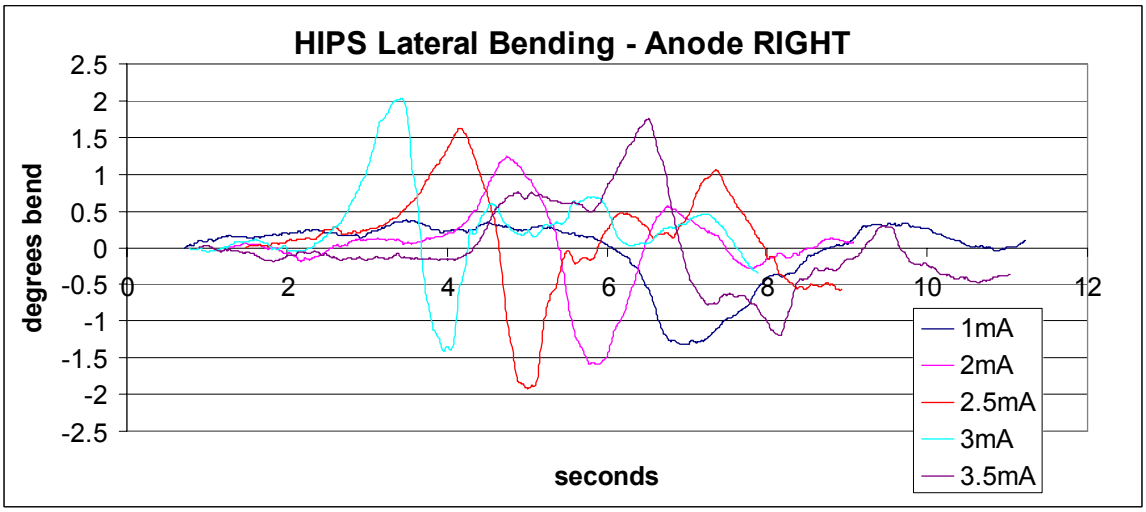
HIPS Lateral Bending - Anode RIGHT
degrees bend
seconds
1mA
2mA
2.5mA
3mA
3.5mA

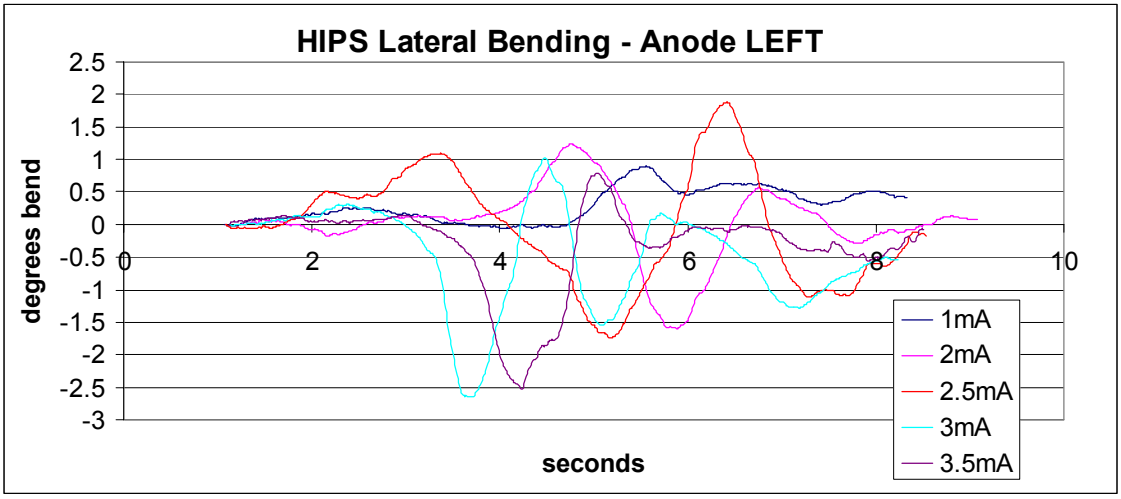
HIPS Lateral Bending - Anode LEFT
degrees bend
seconds
1mA
2mA
2.5mA
3mA
3.5mA

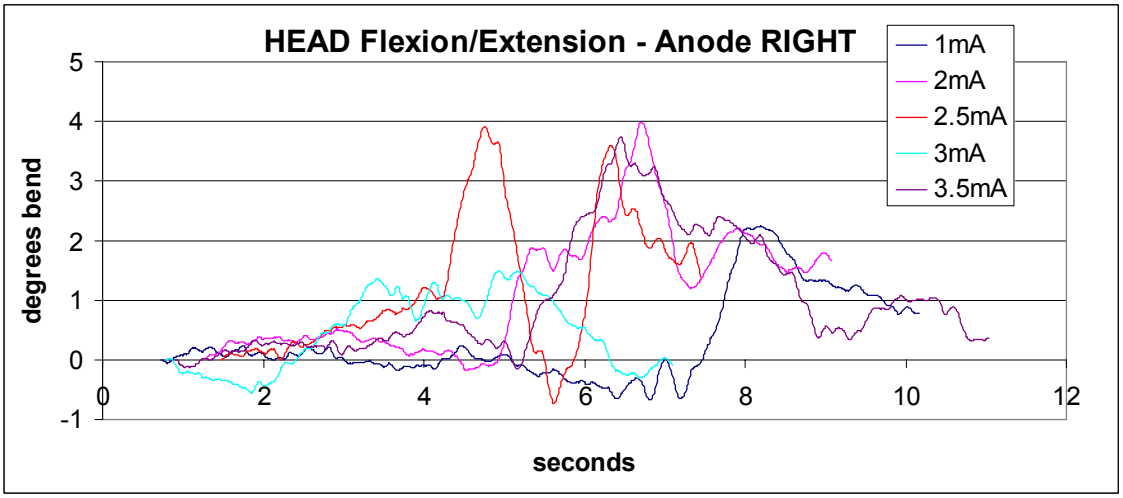
HEAD Flexion/Extension - Anode RIGHT
degrees bend
seconds
1mA
2mA
2.5mA
3mA
3.5mA

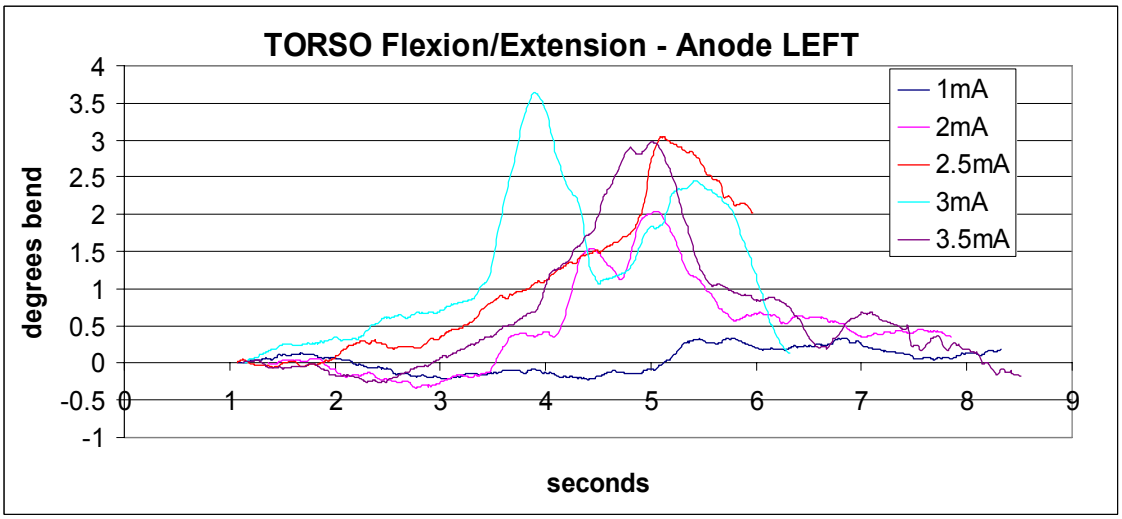
TORSO Flexion/Extension - Anode LEFT
degrees bend
seconds
1mA
2mA
2.5mA
3mA
3.5mA

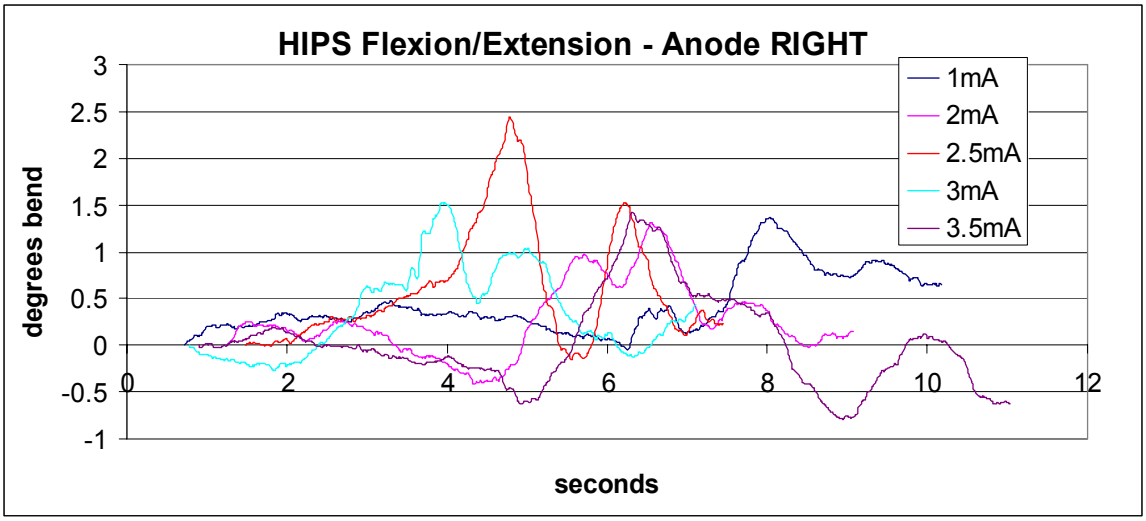
HIPS Flexion/Extension - Anode RIGHT
degrees bend
seconds
1mA
2mA
2.5mA
3mA
3.5mA
3
2.5
2
1.5
1
0.5
0
-0.5
-1
0
2
4
6
8
10
12

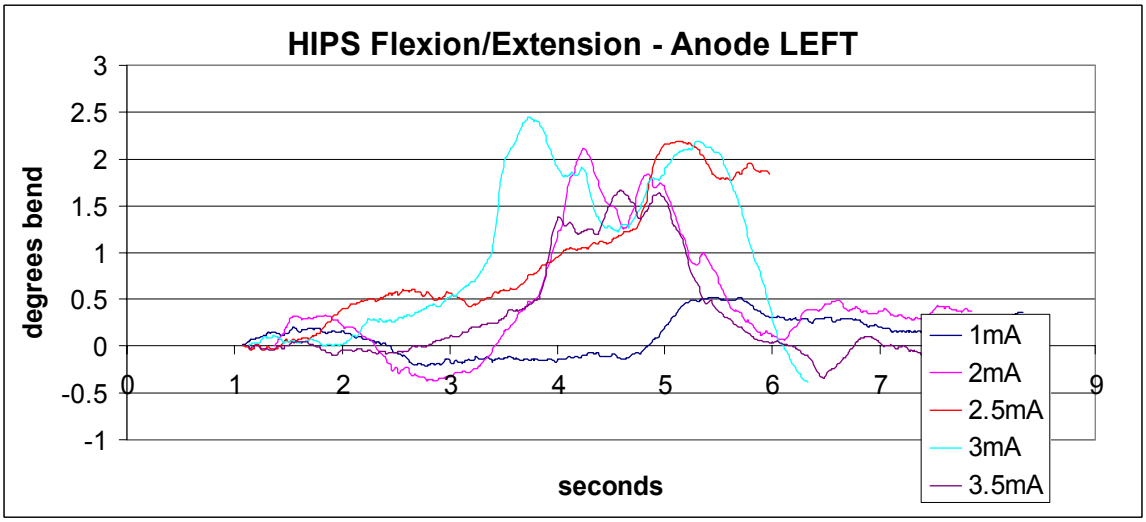
HIPS Flexion/Extension - Anode LEFT
degrees bend
seconds
1mA
2mA
2.5mA
3mA
3.5mA
3
2.5
2
1.5
1
0.5
0
-0.5
-1
0
1
2
3
4
5
6
7
9